NATIONAL ADVISORY COMMITTEE FOR AERONAUTICS

TECHNICAL NOTE 4110

MECHANICAL PROPERTIES OF PNEUMATIC TIRES WITH SPECIAL REFERENCE TO MODERN AIRCRAFT TIRES

By Robert F. Smiley and Walter B. Horne

Langley Aeronautical Laboratory
Langley Field, Va.

Washington
January 1958

D

TABLE OF CONTENTS

NATIONAL ADVISORY COMMITTEE FOR AERONAUTICS

TECHNICAL NOTE 4110

MECHANICAL PROPERTIES OF PNEUMATIC TIRES WITH SPECIAL REFERENCE TO MODERN AIRCRAFT TIRES

By Robert F. Smiley and Walter B. Horne

SUMMARY

A study is presented of most of the properties of pneumatic tires which are of interest to aircraft designers. The principal topics discussed are tire vertical-force-deflection characteristics; lateral, fore-and-aft, and torsional spring constants; footprint-area properties; relaxation lengths; rolling radius; cornering force, cornering power, self-alining torque, and pneumatic caster for yawed rolling conditions; effects of wheel tilt; and tire radial growth under the influence of centrifugal forces.

For each tire property considered, semiempirical equations are set up which take into account the major factors pertinent to the property. Wherever possible each equation is compared with the available experimental data to establish its degree of reliability.

A small amount of previously unpublished experimental data is included, mostly on the subjects of tire tilt, fore-and-aft stiffness, and centrifugal growth.

INTRODUCTION

In order to cope adequately with the landing and taxiing problems of present-day aircraft, those engaged in landing-gear design need information on a large number of pneumatic-tire properties. At present some information can be obtained from such sources as references 1 to 63 for a number of obsolete or foreign types of tires and for a few modern American tires. However, it is doubtful whether the landing-gear designer will find in the literature experimental data which are directly pertinent to the particular tire or tires in which he is interested. Moreover, the scale laws which tire properties obey have not been thoroughly investigated, and, for at least a few important tire properties, these scale laws are not at all obvious; in some cases, simple and accurate scale laws apparently cannot be established at all. Consequently, the aircraft designer cannot confidently scale the results of tire tests in order to apply them to tires in which he is interested.

Some useful studies have been made in regard to theoretical information on tire properties; most of these studies are contained or summarized in references 18 and 45. However, these theoretical studies, although enlightening in some respects, are usually based on oversimplified concepts and, almost inevitably, involve some empirical constants which have not yet been evaluated.

These observations indicate a need to assess the present state of the art for prediction of tire properties by a comprehensive study of the available theoretical and experimental information on tire properties. The present paper presents such a study which has as its primary aims the determination of the most important variables which influence the various tire properties and the establishment of some simple quantitative equations for most of these properties.

Since it is improbable that many readers of this paper will be interested in all the properties discussed herein, each tire property is considered in a separate section with as little cross-correlation between sections as appears necessary.

For each tire property considered some equation is obtained, either from a previous paper, by a crude theoretical derivation, or by purely empirical means. (For example, see appendix A.) Values calculated by these equations are then compared with the available experimental data, which are used to establish any empirical constants needed in the equations. It should be emphasized that the theoretical derivations that are presented are intended largely to give some idea of the basic phenomena, to demonstrate the major variables involved, and to suggest some promising form for empirical equations. In general, the equations resulting from these derivations are far from rigorous; however, by judicious insertion of empirical constants into these equations, it is believed that most of them can give at least a fair correspondence to reality.

Although almost all the discussion in this paper deals with previously published experimental data, a small amount of new data is presented principally on the subjects of tire tilt, braking, and centrifugal-growth effects.

SYMBOLS

a	ratio of net footprint area to gross footprint area, A_n/A_g
a_λ	vertical sinking of tire per unit lateral distortion
A_g	gross footprint area
A_n	net footprint area
b	width of tire-ground contact area (footprint)
c_x	change in fore-and-aft position of center of pressure of vertical force per unit of fore-and-aft deflection
c_γ	change in lateral position of center of pressure of vertical force per radian of wheel tilt
c_λ	change in lateral position of center of pressure of vertical force per unit of lateral distortion
C_b	braking-force coefficient
C_c	cornering-power coefficient
C_z	vertical-force coefficient (see eq. (24))
d	outside diameter of free tire
$D_t(\ )$	differential operator with respect to time, $\frac{d(\ )}{dt}$
e	base of natural logarithms

$$f_1(\ ) = \begin{cases} 0.96(\ ) + 0.216(\ )^2/C_z & \left((\ ) \leqq \frac{10}{3} C_z\right) \\ 2.4\left[(\ ) - C_z\right] & \left((\ ) \geqq \frac{10}{3} C_z\right) \end{cases}$$

F	force
F_1,F_2	drag forces for two narrow coupled wheels

F_x	instantaneous drag or fore-and-aft force (ground force parallel to direction of motion)
F_y	lateral or cornering force (perpendicular to direction of motion)
$F_{y,\gamma}$	lateral force resulting from wheel tilt for standing tire
$F_{y,\gamma,r}$	lateral force resulting from wheel tilt for rolling tire
$F_{y,h}$	lateral hysteresis force
$F_{y,s}$	lateral spring force
$F_{y,\lambda}$	lateral force resulting from elastic and hysteresis effects
F_z	vertical force acting on tire from ground
$F_{z,o}$	average or reference vertical force
F_ψ	normal force (ground force perpendicular to wheel plane)
$F_{\psi,r}$	instantaneous normal force
$F_{\psi,r,e}$	steady-state normal force
h	half-length of tire-ground contact area (footprint)
H	tire radius minus rim radius
$I_{x,w}$	polar moment of inertia of wheel and tire about axis perpendicular to the wheel axle
$I_{y,t}$	polar moment of inertia of tire and tube about wheel axle (excluding solid wheel parts)
$I_{y,w}$	polar moment of inertia of tire, tube, and wheel about wheel axle
J	circumferential decay length
k_t	radius of gyration of tire and tube about the wheel axle, $\sqrt{I_{y,t}/m_t}$
k_w	radius of gyration of wheel and tire about the wheel axle, $\sqrt{I_{y,w}/m_w}$

k_x	radius of gyration of wheel and tire about an axis perpendicular to the wheel axle, $\sqrt{I_{x,w}/m_w}$
K_x	fore-and-aft spring constant
K_α	torsional spring constant
K_γ	lateral force per radian tilt angle for standing tire with $\lambda_o = 0$
$K_{\gamma,r}$	lateral force per radian tilt angle for rolling tire
K_λ	lateral spring constant
L	relaxation length
L_f	unyawed-rolling-force relaxation length
L_s	static relaxation length
L_y	yawed-rolling-relaxation length
L_λ	unyawed-rolling-deflection relaxation length
m_w	mass of tire, tube, and wheel
m_t	mass of tire and tube
M_z	turning or twisting moment about a vertical axis through the wheel center
$M_{z,R}$	turning moment resulting from path curvature
$M_{z,\gamma}$	turning moment resulting from wheel tilt
n	polytropic exponent
N	cornering power, $\left(\frac{dF_{\psi,r,e}}{d\psi}\right)_{\psi\to 0}$
p	tire inflation pressure
Δp	pressure rise, $p - p_c$
p_o	tire inflation pressure at zero vertical load (gage)

$p_{o,a}$	tire inflation pressure at zero vertical load (absolute)
p_b	tire bursting pressure
p_g	average gross footprint pressure, F_z/A_g
p_i	additional pressure resulting from centrifugal forces
p_n	average tire-ground bearing pressure, F_z/A_n
p_r	tire rated inflation pressure
P	tire parameter defined by equation (96) or (97)
q	pneumatic caster, $M_{z,r}/F_{\psi,r}$ or $M_{z,r,e}/F_{\psi,r,e}$
r	outside free radius of tire
r_o	initial tire radius
Δr	increase in tire radius resulting from centrifugal-force effects
r_e	rolling radius
$r_{e,o}$	rolling radius for unyawed and unbraked rolling
$r_{e,1}, r_{e,2}$	rolling radii for two narrow coupled wheels
R	radius of curvature of tire rolling path
s	peripheral distance around tire
s_1	slip ratio
t	time
u	peripheral displacement
v_o	vertical velocity at ground contact
v_H	horizontal rolling velocity
V	inside volume of tire
V_o	initial volume of tire

w	maximum width of undeflected tire
x	displacement in fore-and-aft direction or in direction of motion
y	displacement perpendicular to direction of motion
α	tire twist angle
γ	tilt of wheel plane, radians
δ	vertical tire deflection
δ_o	vertical tire deflection for pure vertical loading conditions $\left(F_x = F_y = 0\right)$
δ_1,δ_2	vertical tire deflection for two narrow coupled tires
δ_b	vertical deflection at tire bottoming
δ_e	effective vertical tire deflection
δ_r	rated vertical tire deflection
δ_x	vertical sinking of tire resulting from application of fore-and-aft ground force
δ_λ	vertical sinking of tire resulting from application of lateral ground force
ϵ_x	elongation strain produced by drag force
ϵ_z	elongation strain produced by vertical force (always negative)
η_x	fore-and-aft hysteresis parameter
η_z	vertical hysteresis parameter
η_α	torsional hysteresis parameter
η_λ	lateral hysteresis parameter
θ	wheel rotation, radians
θ_1	peripheral angle, deg

κ	pressure-rise parameter
λ	lateral distortion of tire equator
λ_o	lateral distortion of tire equator at center of tire-ground contact area
λ_x	fore-and-aft distortion of tire-ground contact area
μ_x	drag coefficient of friction
$\mu_{x,m}$	maximum drag coefficient of friction for locked-wheel tests
$\mu_{x,s}$	sliding-drag coefficient of friction for locked-wheel tests
μ_ψ	yawed rolling coefficient of friction
ξ	tilt parameter (see ref. 52)
τ_λ	lateral-spring-constant coefficient
ϕ	yaw-angle parameter, $\frac{N}{\mu_\psi F_z}\psi$
ψ	yaw angle
ω	wheel angular velocity, radians/sec
ω_o	wheel angular velocity for unbraked rolling, radians/sec

Subscripts:

max	maximum value
st	static

DEFINITIONS

The following terms are defined for use in many parts of this paper. Other terms which are used only locally in the text are defined at the appropriate places.

RATED PRESSURE

Inasmuch as the tire carcass stiffness is a factor of some importance in understanding the behavior of pneumatic tires, some numerical index of this carcass stiffness which could be used readily in establishing empirical equations for tire properties appears desirable. Somewhat arbitrarily, this paper adopts the quantity "rated pressure" as this standard. The term "rated pressure" (denoted by the symbol p_r) is defined as one-quarter of the bursting pressure p_b of the tire. (The minimum bursting pressure for current tires can be found in refs. 62 and 63.) The rated pressure p_r thus defined is, for current American tires, almost always exactly equal to the inflation pressure listed in tire specifications (refs. 61 to 63); however, the operating inflation pressure of tires may be considerably different from the specified or rated pressure. For example, some tires are operated at pressures less than one-half the rated pressure, and others may be operated at pressures in excess of the rated pressure.

For calculations in this paper which required numerical values of the rated pressure, the following procedure was followed: For recent American tires the rated pressure was calculated from the minimum bursting pressures given in references 62 and 63. For some German tires (for which little bursting-pressure data were available) the rated pressure was considered to be equal to the customary inflation pressure according to indirect evidence in German tire specifications (for example, fig. 23 of ref. 50). For a few tires, for which no better estimate could be made, the rated pressure was considered to be equal to the tire inflation pressure.

RATED AND BOTTOMING DEFLECTIONS

The term "rated deflection" (denoted by the symbol δ_r) is used to refer to the customary operating vertical deflection of a tire as specified by references 61 to 63. "Bottoming deflection" (denoted by the symbol δ_b) refers to the maximum vertical deflection which a tire can sustain before the rim begins to cut into the tire carcass. Both rated and bottoming deflections are indicated in most figures in the present paper in order to give some idea of the practical vertical-deflection range for the data in these figures.

SLIP RATIO

The "slip ratio" (denoted by the symbol s_1) of a rolling unyawed partially braked wheel may be defined as follows:

$$s_1 = \frac{\omega_o - \omega}{\omega_o} = \frac{(v_H/\omega) - (v_H/\omega_o)}{v_H/\omega} \qquad (1)$$

where v_H is the rolling velocity, ω_o is the angular velocity for unbraked rolling, and ω is the angular velocity for braked rolling. Also, since the ratio v_H/ω is defined as the tire rolling radius r_e and the ratio v_H/ω_o is defined as the unbraked rolling radius $r_{e,o}$, equation (1) may also be written in the forms

$$s_1 = \frac{r_e - r_{e,o}}{r_e} \qquad (2)$$

$$r_e = \frac{r_{e,o}}{1 - s_1} \qquad (3)$$

TIRE CONSTRUCTION AND NOMENCLATURE

The following miscellaneous information regarding conventional tire construction and nomenclature should be helpful as background information for many parts of the discussion of this paper.

GENERAL DISCUSSION

The types of tires in current use on most American airplanes may be briefly described as follows: (See also refs. 61 to 63.) These tires are classified according to a standard type number from I to VII, and each of these types may be further subdivided into groups according to the use of the tire, the two primary subdivisions being the collective class of nose- and main-wheel tires and the class of tail-wheel tires. At present, although most of these tire types are still in use on a few isolated airplanes, the majority of current airplanes use only types I, III, and VII tires, and even the type I tires are becoming obsolete.

The general appearance and cross-sectional shapes of the three major types of tires (types I, III, and VII) are indicated in figure 1 in accordance with information from reference 21 for several nose- and main-wheel tires of conventional tread (that is, not channel tread). Tail-wheel tires of these same types may be somewhat different in construction. Figure 1 shows that the type I tires are considerably different in appearance from the types III and VII tires, the type I tires having a much smoother profile and having their sections of maximum internal width much closer to the wheel rim. The difference between the types III and VII tires is less clear cut; apparently, the main difference is that the type III tires are somewhat fatter (that is, have a larger width-diameter ratio) than the corresponding type VII tires.

In the body of this paper the experimental data discussed for types I, III, and VII tires refer almost exclusively to nose- and main-wheel tires of conventional tread unless it is specifically stated otherwise. Practically no information is available for tail-wheel or other types of tires.

SPECIFIC NOMENCLATURE

An abbreviated notation has been adopted in this paper to designate specific tires. This notation is illustrated for a type III nose- and main-wheel tire as follows:

```
45×15-14PR-III-c(15.50-20)R17-C
|    |     |  |    |       |  |
|    |     |  |    |       |  └Code letter for specific tires
|    |     |  |    |       |
|    |     |  |    |       └Reference number
|    |     |  |    |
|    |     |  |    └Standard tire designation
|    |     |  |
|    |     |  └Manufacturer
|    |     |
|    |     └Tire type number
|    |
|    └Ply rating
|
└Tire size (diameter × width)
```

The first set of numbers (45×15) represents the nominal diameter and width of the tire, always in inches, usually to the nearest inch. (For the modern tires discussed in this paper the values of diameter and width were obtained either by direct measurement or from refs. 61 to 63.) The third number (14PR) represents the tire ply rating. The fourth number (III) represents the tire standard type number. The fifth quantity (c) is a code to designate the tire manufacturer. The next set of numbers (15.50-20) designates the standard designation for the particular tire according to references 61 to 63. This designation differs in form for different types of tires and for different uses (nose or tail wheel). The next number (R17) represents the number of the reference in which the corresponding experimental data are to be found; for unpublished data the designation RU is used. The last letter (C) represents the code letter used in the corresponding reference to designate that particular tire.

This detailed designation is needed in only a few places in this paper. In most other cases, parts of the designation are either of little importance to the associated discussion, are unknown, or are not pertinent (for example, type numbers cannot be applied to foreign-type tires); consequently, they are omitted from the tire designation for such cases.

PROPERTIES OF A STANDING OR NONROTATING TIRE

This section considers the properties of a standing or nonrotating tire subjected to the following types of loading conditions: pure vertical loading, combined vertical and lateral loading, combined vertical loading and twisting moment, combined vertical and fore-and-aft (drag) loading, and combined vertical loading and tilt.

PURE VERTICAL LOADING

In this section the following properties of a tire subjected to pure vertical loading are discussed: geometric properties of the ground-contact or footprint area, pressure rise due to vertical deflection, vertical force-deflection relationships, and gross and net or average bearing pressure between tire and ground.

Geometric Properties of Footprint Area

Footprint length.- The footprint length $2h$ of a pneumatic tire under pure vertical loading has been found by Rotta (ref. 44 or 45) to be largely a function of tire diameter d and vertical deflection δ. If the tire were not distorted by the vertical force, this length would be equal to the length of the geometric chord formed by the intersection of a circle having a diameter equal to the diameter of the tire with the ground plane or

$$2h = 2d\sqrt{(\delta/d) - (\delta/d)^2} \tag{4}$$

(See dashed line in fig. 2.) However, because of the effect of vertical load, the actual tire circumference is distorted from a circular shape (see solid line in fig. 2), and the footprint length becomes less than the length of the geometric chord given by equation (4).

Data showing the experimental variation of footprint length with vertical deflection for pure vertical loading are presented in figure 3 for several type VII tires and one type I tire and in figure 4 for several German aircraft tires. As can be seen from these figures, the experimental footprint length is approximately 85 percent of the geometric-chord length for the types I and VII tires, or

$$h/d = 0.85\sqrt{(\delta/d) - (\delta/d)^2} \tag{5}$$

For some of the German tires the footprint length is smaller.

Near rated tire deflection the footprint length is seen to be approximately

$$2h = 0.44d \tag{6}$$

Footprint width.- Experimental data showing the variation of footprint width b with tire vertical deflection δ, for pure vertical loading, are presented in figure 5 for several type VII tires and one type I tire. As can be seen from the figure, all these data can be fairly accurately represented by the empirical equation

$$b/w = 1.7\sqrt{(\delta/w) - 2.5(\delta/w)^4 + 1.5(\delta/w)^6} \tag{7}$$

or, more approximately, by the simpler equation

$$b/w = 2\sqrt{(\delta/w) - (\delta/w)^2} \tag{8}$$

Near rated deflection the data indicate that

$$b \approx 0.84w \tag{9}$$

or, for these tires, in terms of tire diameter,

$$b \approx 0.25d \tag{10}$$

Gross footprint area.- The gross footprint area A_g of a tire is defined as the area of contact between tire and ground, including the spaces between the tire treads. According to Hadekel's analysis of the experimental data of Michael (see refs. 18 and 38, respectively), this area varies approximately linearly with vertical deflection and can be approximately represented by the empirical equation

$$A_g = 2.25(\delta - 0.03w)\sqrt{wd} \tag{11}$$

Michael's data and equation (11) are shown together in figure 6 to illustrate the degree of reliability of equation (11). This figure indicates that equation (11) gives reasonable predictions of the gross footprint area for the obsolete tires tested by Michael. However, figure 7 indicates that equation (11) does not give as good predictions for modern types I and VII tires. These modern tires can be better represented by the slightly simpler empirical equation

$$A_g = 2.3\delta\sqrt{wd} \tag{12}$$

Net or bearing footprint area.- The net or bearing footprint area A_n of a tire is defined as the actual area of contact between tire and ground exclusive of the spaces between the tire treads. This net area can be expressed in terms of the gross footprint area by the relation

$$A_n = aA_g \tag{13}$$

where the factor a, in general, depends largely on the tread pattern and, for the modern tires investigated in references 22 to 24 and 53, appears to depend only slightly on the tire vertical deflection. (See table I.)

Pressure Rise

When an inflated pneumatic tire is subjected to a vertical deflection or force, the resulting air compression causes a rise in the inflation pressure. This pressure rise may be calculated approximately from the following considerations:

First, consider the gas law for a polytropic process in the form

$$\left(p_{o,a} + \Delta p\right)\left(V_o + \Delta V\right)^n = p_{o,a}V_o$$

or

$$\left(1 + \frac{\Delta p}{p_{o,a}}\right)\left(1 + \frac{\Delta V}{V_o}\right)^n = 1 \tag{14}$$

where $p_{o,a}$ is the initial absolute inflation pressure (for zero tire deflection), Δp is the pressure rise, V_o is the initial air volume, ΔV is the change in volume, and n is the polytropic exponent. For small pressure and volume changes, equation (14) can, by means of a binomial-series expansion of the factor $\left(1 + \frac{\Delta V}{V_o}\right)^n$ and neglect of small higher order terms, be put in the simpler form

$$1 = \left(1 + \frac{\Delta p}{p_{o,a}}\right)\left(1 + n\frac{\Delta V}{V_o} + \text{Small higher order terms}\right)$$

$$= 1 + \frac{\Delta p}{p_{o,a}} + n\frac{\Delta V}{V_o} + \text{Small higher order terms}$$

or, approximately,

$$\Delta p = -np_{o,a}\frac{\Delta V}{V_o} \tag{15}$$

According to the experimental static tests of Michael (see ref. 38) the pressure rise, and, hence, the volume change, is proportional to the square of the vertical tire deflection δ so that equation (15) can be expressed in the form

$$\Delta p = n\kappa p_{o,a}(\delta/w)^2 \tag{16}$$

where κ is a constant depending on the tire shape.

For the usual static tire tests, the air-compression process is probably essentially isothermal ($n = 1$) so that equation (16) becomes

$$\Delta p_{st} = \kappa p_{o,a}(\delta/w)^2 \tag{17}$$

Some typical static-test data illustrating the degree of validity of equation (17) are shown in figure 8 for a 27-inch-diameter type I tire. In this figure the theoretical variation of Δp (with $\kappa = 0.66$) is well confirmed by the experimental data for essentially the entire possible range of tire deflection and for as large a range of tire inflation pressures as is usually likely to be encountered in practice (from $p_o \approx 0.3p_r$ to $p_o \approx 1.1p_r$).

According to experiment and to some approximate theoretical considerations (see ref. 18) the tire-shape constant κ depends on the tire fatness ratio or width-diameter ratio. The experimental variation of the shape constant with fatness ratio, as obtained from static-test data, is shown in figure 9 for several types I, III, and VII tires and for a number of obsolete types of tires. These data indicate that the general trend of the shape-constant variation with fatness ratio appears to follow the equation

$$\kappa = 1.5w/d \tag{18}$$

An additional variation of tire-shape constant is seen with tire type. Mean values of κ, estimated from the data in figure 9, are probably sufficiently accurate for practical calculations of pressure rise. These values are 0.66, 0.62, and 0.35 for types I, III, and VII tires, respectively.

Vertical-Force-Deflection Variations

In this section the nature of the variation of vertical ground force F_z with vertical tire deflection δ for a nonrotating tire is discussed. (The variation for a rotating tire is treated in a subsequent section.) As is fairly well known, this variation depends to some extent on the rate of vertical loading. For example, figure 10 indicates that the force for a given deflection is appreciably greater for a drop test than for a static test. In order to evaluate these variations quantitatively, the following procedure is used: First, an analysis is made of the tire static-force-deflection variation for the increasing force condition. Second, an attempt is made to explain the differences between the static and dynamic (drop-test) curves.

Static-force-deflection variation.- As a first step for evaluating the static relation between vertical ground force and vertical tire deflection, it is recognized that the ground force must be equal to the product of the footprint area A_g and the footprint pressure p_g, or

$$F_z = p_g A_g \tag{19}$$

or, after the assumption is made that A_g obeys a relationship like that given by equation (11) or (12),

$$F_z = p_g w \sqrt{wd}\, f(\delta/w) \tag{20}$$

As a first approximation, the footprint pressure could be assumed to be equal to the inflation pressure, and equation (20) would take the form

$$\frac{F_z}{pw\sqrt{wd}} = f(\delta/w) \tag{21}$$

If equation (21) were realistic, then plots of the parameter $\frac{F_z}{pw\sqrt{wd}}$ against δ/w would yield a single curve regardless of inflation pressure. However, this is not the case, as is indicated, for example, by the data in figure 11(a). The reason for the failure of equation (21) is that it does not take into account the fact that the finite tire carcass stiffness gives a finite tire stiffness for zero inflation pressure. It was found, however, that this tire-carcass effect could be taken into account with good accuracy for almost all modern tires by the following empirical modification of equation (21):

$$\frac{F_z}{\left(p + 0.08p_r\right) w \sqrt{wd}} = f(\delta/w) \tag{22}$$

where the quantity $0.08p_r$ can be considered to be an effective carcass pressure. (The symbol p_r is the rated pressure.) Some experimental data illustrating the adequacy of equation (22) are shown in figures 11(b) and 12 for some relatively extreme changes in inflation pressure.

Empirical evaluation of the function $f(\delta/w)$ for equation (22) from the available experimental data led to the following alternate final forms of this equation:

$$\left.\begin{aligned} \frac{F_z}{\left(p + 0.08p_r\right)w\sqrt{wd}} &= 0.96(\delta/w) + \frac{0.216(\delta/w)^2}{C_z} & \left(\delta/w \leqq \frac{10}{3} C_z\right) \\ \frac{F_z}{\left(p + 0.08p_r\right)w\sqrt{wd}} &= 2.4\left[(\delta/w) - C_z\right] & \left(\delta/w \geqq \frac{10}{3} C_z\right) \end{aligned}\right\} \tag{23}$$

$$\frac{F_z}{\left(p + 0.08p_r\right)w\sqrt{wd}} = 2.4\left[(\delta/w) - C_z\left(1 - e^{\frac{-0.6\delta/w}{C_z}}\right)\right] \tag{24}$$

where $C_z = 0.02$ for type I tires and $C_z = 0.03$ for types III and VII tires. Two forms of the function $f(\delta/w)$ were obtained, one chosen for ease of calculation (eq. (23)) and the other to obtain a single continuous equation form (eq. (24)). It might also be noted that Hadekel (ref. 18) found that the vertical-deflection characteristics of a number of obsolete types of tires could be fitted with fair accuracy by the equation

$$\frac{F_z}{\left(p + p_1\right)w\sqrt{wd}} = 2.25(\delta/w) - 0.03 \tag{25}$$

where the quantity p_1 in equation (25) is a constant corresponding to the quantity $0.08p_r$ in equation (23).

Experimental data demonstrating the degree of reliability of equations (23) and (24) are shown in figure 13 for a large number of types I, III, and VII tires. Almost all the tire data shown are in reasonable agreement with the predictions of equations (23) and (24), regardless of tire size and manufacturer.

Rated conditions: At rated conditions of pressure and deflection, equation (23) reduces approximately to the following forms

$$F_z \approx 0.52pw\sqrt{wd} \approx 0.11pd^2 \qquad \text{(Type I)} \tag{26}$$

$$F_z \approx 0.57pw\sqrt{wd} \approx 0.12pd^2 \qquad \text{(Type III)} \tag{27}$$

$$F_z \approx 0.57pw\sqrt{wd} \approx 0.08pd^2 \qquad \text{(Type VII)} \tag{28}$$

or to a cruder approximation for any of these types,

$$F_z \approx 0.10pd^2 \tag{29}$$

Dynamic-force-deflection variation.- This section describes the most conspicuous features of the vertical-force-deflection characteristics of tires for the special case of dynamic vertical drop tests of nonrotating tires and briefly discusses the relationships between these dynamic characteristics and the corresponding static characteristics.

Some typical dynamic vertical-force-deflection curves obtained from drop tests with a pair of 56-inch-diameter type I tires are shown in figure 14 for a range of initial vertical velocities (at ground contact) from about 0 to 12 feet per second. This figure shows that, for the increasing-force branch (upper branch) of these curves, the shapes of the curves appear to be essentially independent of the vertical velocity. This conclusion is also supported by the experimental data of reference 39 for a 27-inch-diameter type I tire.

As was noted previously, the vertical force for a given vertical deflection is noticeably larger for dynamic drop-test conditions than for static conditions. (See fig. 10.) Part of the reason for this difference may be due to the difference in the air-compression process for the two cases (probably essentially isothermal for static tests and polytropic for dynamic drop tests) as was previously discussed in the section entitled "Pressure Rise." However, the calculations of reference 53 indicate that this effect cannot entirely explain the difference between static and dynamic characteristics. Other possible reasons for the differences may result from differences in the tire-carcass effects and the hysteresis behavior for each condition. In regard to the hysteresis behavior, it may be seen from figure 10 (see also refs. 38 and 53) that the hysteresis loop for the drop-test case is somewhat larger than for the static case but is not extremely so.

These tire characteristics for vertical drop tests (without wheel rotation) are of limited significance from a practical standpoint since they are not, in many respects, representative of realistic landing conditions in which the wheels are almost always rotating. (See, for example, ref. 53 and also subsequent parts of this paper.) For this reason, no attempt is made herein to obtain analytical equations for the tire vertical-force-deflection characteristics for the drop-test case without wheel rotation. However, the observation that the vertical-force-deflection variation is largely independent of vertical velocity is probably of general significance and applicable to realistic wheel-rotating landing conditions.

Gross Footprint Pressure

The gross footprint or ground pressure p_g (ratio of vertical force to gross footprint area) for a tire under pure vertical loading can be obtained in first approximation by dividing equation (23) by equation (12), which gives the equations

$$\left.\begin{aligned} \frac{p_g}{p + 0.08p_r} &= \frac{1}{2.3}\left[0.96 + \frac{0.216(\delta/w)}{C_z}\right] && \left(\delta/w \leqq \frac{10}{3} C_z\right) \\ \frac{p_g}{p + 0.08p_r} &= \frac{24}{23}\left[1 - C_z(\delta/w)^{-1}\right] && \left(\delta/w \geqq \frac{10}{3} C_z\right) \end{aligned}\right\} \quad (30)$$

where $C_z = 0.02$ for type I tires and $C_z = 0.03$ for types III and VII tires. The predictions of equations (30) are compared with experimental data in figure 15 for types I and VII tires from references 22 to 24 and 53. Fair agreement is seen to exist except at small vertical deflections. The following empirical equations, which are minor modifications of equations (30), are seen to fit the data better in this low deflection range:

$$\left.\begin{aligned} \frac{p_g}{p + 0.08p_r} &= 0.6 + \frac{81}{1600C_z}(\delta/w) && \left(\delta/w \leqq \frac{40}{9} C_z\right) \\ \frac{p_g}{p + 0.08p_r} &= 1.05 - C_z(\delta/w)^{-1} && \left(\delta/w \geqq \frac{40}{9} C_z\right) \end{aligned}\right\} \quad (31)$$

Average Bearing Pressure

The average bearing or contact pressure p_n between tire and ground is equal to the gross footprint pressure p_g divided by the ratio a of gross footprint area to net (bearing) footprint area, or

$$p_n = \frac{p_g}{a} \quad (32)$$

where p_g is given by equations (31) or figure 15, and a depends, in general, on the tire tread pattern but usually appears to range between 0.60 and 0.76. (See table I.)

A sample plot of the variation with vertical deflection of the ratio of bearing pressure to inflation pressure is shown in figure 16 for rated pressure conditions, according to equations (31) and (32), with a taken as 0.7 and C_z as 0.03. For these conditions the bearing pressure varies from about 86 percent of the inflation pressure for zero deflection to about 143 percent for large deflections.

COMBINED VERTICAL AND LATERAL LOADING

When a stationary vertically loaded tire at a vertical load F_z, an inflation pressure p, and an initial vertical deflection δ_o is subjected to a lateral force perpendicular to the wheel plane $F_{y,\lambda}$, the tire experiences a corresponding lateral deformation λ_o at the ground, a vertical sinking δ_λ, and a lateral shifting of the vertical-force center-of-pressure location $c_\lambda \lambda_o$. (See fig. 17.) The available experimental data pertinent to these quantities, to the corresponding lateral spring constant K_λ, and to the corresponding lateral distortion of the tire equator are summarized and analyzed in this section.

Lateral Spring Constant

Before the available experimental data for the lateral spring constant are discussed, some mention should be made of the manner in which this spring constant is determined. Usually the force-deflection curves from which these spring constants are determined look somewhat like the slightly idealized curve shown in the following sketch:

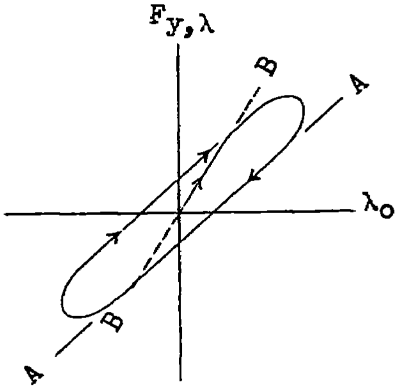

This sketch shows that the slope of the solid straight line AA represents the spring constant. The initial slope of this curve (slope of line BB) is seen to be dependent to some extent on the starting position of the force-deflection curve inside the hysteresis loop and is therefore not necessarily equal to the spring constant. Since some of the available tire force-deflection curves consist only of the initial quarter-cycles of hysteresis loops, the values of spring constants determined from such quarter-cycles depend to some extent on the judgment of the observer. This same type of difficulty due to hysteresis effects was also experienced for almost all the tire properties discussed subsequently (for example, for torsional and fore-and-aft spring constants).

Sample experimental lateral-spring-constant data are shown in figure 18 for a type I tire. Most data for this parameter indicate that the lateral spring constant decreases with increasing vertical deflection and increases approximately linearly with increasing inflation pressure. These two variables (vertical deflection and inflation pressure) appear to be the primary variables influencing the variation of lateral spring constant for any one tire. However, this spring constant is also influenced slightly by the amplitude of the corresponding force-deflection hysteresis loop, as is indicated in figure 19, which presents lateral-spring-constant data obtained from static tests (ref. 24) and dynamic vibration tests (ref. 25). These data indicate that the spring constant decreases with increasing amplitude. However, this variation does not appear to be much over 10 percent, at least for the data shown, and is disregarded in the subsequent analysis.

Dimensional considerations and observation of plots like those of figure 18 indicate that for most tires the lateral stiffness can be predicted by an empirical equation of the type

$$K_\lambda = \tau_\lambda w\left(p + 0.24p_r\right)\left[1 - \left(0.7\delta_o/w\right)\right] \qquad (33)$$

(A detailed discussion of the procedure used to derive eq. (33) is given in appendix A.) The quantity $0.24p_r$ in equation (33) (where p_r is the rated pressure) takes into account the fact that, because of tire carcass stiffness, the lateral stiffness is finite for zero inflation pressure. This quantity may be regarded as an effective lateral carcass pressure similar to the corresponding quantity used in the previous analysis of tire vertical-force-deflection characteristics. (For example, see eq. (22).) However, it should be noted that the influence of the carcass is three times as important for the lateral stiffness (where effective carcass pressure is equal to $0.24p_r$), as it was for the vertical stiffness (where effective carcass pressure is equal to $0.08p_r$).

From the experimental lateral-stiffness static-test data shown in figure 20, the approximate numerical values of the coefficient τ_λ for types I, III, and VII tires are seen to be

$$\tau_\lambda = 3 \qquad \text{(Type I tires)} \qquad (34)$$

$$\tau_\lambda = 2 \qquad \text{(Types III and VII tires)} \qquad (35)$$

Additional information on the parameter τ_λ is provided by figure 21, which presents values of τ_λ estimated from the available lateral-stiffness data for a large number of tires (including the tires of fig. 20). These values of τ_λ are plotted against the tire shape or fatness ratio w/d. Consider first the German tires which are designated by circle symbols. The available information on these tires indicates that they physically resemble types III and VII tires more than type I tires and, as would be expected from the preceding discussion of figure 20 (see also eqs. (34) and (35)), they tend to give values of τ_λ which are, on the average, roughly equal to 2. The one German tire which definitely resembles a type I tire is seen to give a larger value of τ_λ than the other German tires, as would also be expected from the previous discussion.

The significance of the vibration-test data (from ref. 25) shown in figure 21 is not very clear. First, the lateral stiffnesses of these tires do not vary with inflation pressure according to the expression used in equation (33). Consequently, values of τ_λ determined from these data are not independent of pressure. The values of τ_λ shown in the figure for these tires apply only to the rated pressure condition; moreover, since three of these tires were not tested near rated pressure, the data had to be extrapolated. Finally, the only tire from the vibration tests which appears to be at all comparable to any of the static-test tires of figure 20 is the 24×7.7-10PR-VII tire, and this particular tire resembles physically a type I tire more than it does any of the type VII tires used for the static tests. In view of these observations, the general applicability of equations (33), (34), and (35) to realistic dynamic conditions is questionable. However, because of the limitations of the vibration data mentioned previously, it is believed that these equations furnish as good an estimate of tire lateral stiffness as can be made at present.

Vertical-Force Center of Pressure

Under the influence of a lateral force, the vertical-force center of pressure shifts a distance $c_\lambda \lambda_o$ in the direction of the applied force with respect to the wheel center plane, where λ_o represents the lateral deformation of the base of the tire and the coefficient c_λ represents the fraction of the distance λ_o through which the vertical-force center of pressure moves. (See fig. 17.) The available data on this subject, for types I, III, and VII tires, are presented in figure 22 and are summarized as follows:

$$c_\lambda = 0.85 \qquad \text{(Type I)} \tag{36}$$

$$c_\lambda = 0.80 \qquad \text{(Type III)} \tag{37}$$

$$c_\lambda = 0.70 \qquad \text{(Type VII)} \tag{38}$$

Vertical Sinking

Upon application of a lateral force, a tire at a given vertical force sinks vertically through the small distance δ_λ, which can be represented as a fraction a_λ of the corresponding lateral distortion λ_o, or

$$\delta_\lambda = a_\lambda |\lambda_o| \tag{39}$$

where $|\lambda_o|$ denotes the absolute value of the lateral distortion. The experimental data of reference 21, shown in figure 23, indicate the following values of a_λ for types I, III, and VII tires.

$$a_\lambda = 0.21 \qquad \text{(Type I)} \tag{40}$$

$$a_\lambda = 0.15 \qquad \text{(Types III and VII)} \tag{41}$$

Lateral Deformation (Static Relaxation Length)

Under the influence of a lateral force, the equator or peripheral center line of a tire is laterally distorted through the distance λ in the manner indicated in figure 17. It can be seen from the experimental data in this figure that (except in and near the edge of the ground-contact area) the variation of the lateral deformation λ with the tire peripheral angle θ_1 or peripheral distance s obeys an essentially exponential law; that is, the lateral deformation can be expressed by an equation of the form

$$\lambda = Ae^{-s/L_s} \tag{42}$$

where A is a constant and the exponential constant L_s is called the tire static relaxation length. The form of the variation of this static relaxation length with tire inflation pressure and vertical deflection is indicated in figure 24 for a 56×16-32PR-VII-R21A tire. The figure shows that this static relaxation length decreases with increasing inflation pressure and with increasing vertical deflection. The following type of empirical equation appears to cover this variation with fair accuracy for types VII and III tires, as can be seen from examination of figure 25:

$$\frac{L_s}{w} = \left(2.8 - 0.8p/p_r\right)\left(1.0 - 4.5\delta_o/d\right) \qquad (43)$$

where p is the inflation pressure and p_r is the rated pressure. The static relaxation lengths for some of the German aircraft tires in figure 25(b) appear to be somewhat larger.

COMBINED VERTICAL LOADING AND TWISTING MOMENT

When a stationary vertically loaded tire at a vertical load F_z, an inflation pressure p, and an initial vertical deflection δ_o is subjected to a twisting moment M_z, the tire experiences a corresponding angular deformation α. The available experimental data pertinent to this moment-angle variation and to the corresponding torsional spring constant K_α are summarized and analyzed in this section.

General Observations

Sample static-test data illustrating the variation of twisting moment with twist angle are shown in figure 26 for a 40×12-14PR-VII-R24-B tire at a fixed inflation pressure and vertical deflection and at several different amplitudes. These curves show that the torsional spring constant or slope of these curves decreases with increasing amplitude. The magnitude of this decrease can be seen more easily from figure 27, which presents the variation of torsional spring constant with amplitude for two 40×12-14PR-VII-R24 tires for several loading conditions. The magnitude of this amplitude effect appears to be appreciable and probably ought to be taken into account in future considerations of tire properties. However, since the available information on torsional stiffness is extremely limited and is based mostly on not extremely accurate estimates from quarter- or half-cycles of hysteresis loops, an analysis of the amplitude effect in this paper seemed premature. Consequently, this effect is neglected in the subsequent analysis.

Torsional Spring Constant

Sample experimental data illustrating the effects of vertical deflection and inflation pressure on the torsional stiffness are shown in figure 28 for a 28×9-10PR-I(27-inch)R21-E2 tire. These data indicate that the torsional stiffness increases approximately linearly with both increasing pressure and vertical deflection. These variations, for most tires, can be represented with fair accuracy by empirical equations of the form

$$\left.\begin{aligned}\frac{K_\alpha}{(p + 0.8p_r)w^3} &= 250\left(\delta_o/d\right)^2 &\qquad \left(\delta_o/d \leqq 0.03\right)\\[2ex] \frac{K_\alpha}{(p + 0.8p_r)w^3} &= 15\left[\left(\delta_o/d\right) - 0.015\right] &\qquad \left(\delta_o/d \geqq 0.03\right)\end{aligned}\right\}\qquad(44)$$

for types III and VII tires and by the similar equations

$$\left.\begin{aligned}\frac{K_\alpha}{(p + 0.8p_r)w^3} &= 475\left(\delta_o/d\right)^2 &\qquad \left(\delta_o/d \leqq 0.02\right)\\[2ex] \frac{K_\alpha}{(p + 0.8p_r)w^3} &= 19\left[\left(\delta_o/d\right) - 0.01\right] &\qquad \left(\delta_o/d \geqq 0.02\right)\end{aligned}\right\}\qquad(45)$$

for type I tires. Experimental static-test data illustrating the degree of reliability of these equations are shown in figure 29(a) to 29(c). These data indicate that the agreement between the data and calculations is far from excellent; however, in view of the fact that the literature appears to contain no simple equations at all for the torsional spring constant, these equations should at least be useful as a first approximation. The wide variation of the data from the calculation is due in part to the neglect of the apparently important amplitude effect mentioned previously.

Some additional static-test data on torsional stiffness are shown in figure 29(d) for several German tires. It is noted that the spring-constant data for most of these tires appear to be in rough agreement with the empirical predictions for the types I, III, and VII tires.

COMBINED VERTICAL AND FORE-AND-AFT LOADING

When a stationary vertically loaded tire at a vertical load F_z and an initial vertical tire deflection δ_o is subjected to a fore-and-aft or drag force F_x, the tire experiences a corresponding drag deformation at the ground λ_x, a vertical sinking δ_x, and a shift of the vertical-force center of pressure $c_x\lambda_x$. (See fig. 30.) The available experimental data pertinent to these quantities, to the corresponding fore-and-aft spring constant K_x, and to the corresponding distortion of the tire equator are summarized and analyzed in this section.

Fore-and-Aft Spring Constant

Before the available experimental fore-and-aft spring-constant data are discussed, it should be noted that the available fore-and-aft force-deflection data from which such spring constants can be determined consist almost entirely of the first quarter-cycles of force-deflection hysteresis loops, and, as was mentioned previously in the discussion of the lateral spring constant, because of hysteresis effects, such spring constants are sometimes of questionable accuracy.

Sample experimental fore-and-aft spring-constant data from the investigation of reference 21 are shown in figure 31 for a 56×16-32PR-VII tire. These data show that the fore-and-aft spring constant tends to increase with increasing tire vertical deflection and to increase only slightly (or not at all) with increasing inflation pressure.

In view of the preceding analysis of lateral and torsional stiffness, it appeared reasonable to expect that the fore-and-aft stiffness could be described by a similar equation of the type

$$K_x = k_1 d\left(p + k_2 p_r\right) f\left(\delta_o/d\right) \tag{46}$$

where k_1 and k_2 are numerical constants. However, since the fore-and-aft stiffness does not depend strongly on the inflation pressure (see fig. 31), it would be expected that $k_2 \gg 1$; thus, to a first approximation, $p \ll k_2 p_r$, and equation (46) almost reduces to the form $K_x = k_1 k_2 p_r f\left(\delta_o/d\right)$, from which relation it is evident that an independent evaluation of the two constants k_1 and k_2 is difficult. Consequently, the value $k_2 = 4$ was almost arbitrarily selected and the available data were analyzed on this basis.

It appears from the static-test experimental data of references 21 to 24 for several type VII tires that $k_1 = 0.6$ and $f(\delta_o/d) = \sqrt[3]{\delta_o/d}$; therefore, the fore-and-aft stiffness can be expressed by the equation

$$K_x = 0.6d(p + 4p_r)\sqrt[3]{\delta_o/d} \qquad \text{(Type VII)} \qquad (47)$$

(See fig. 32(a).) According to some data obtained by the General Aerodynamics Branch of the Langley Laboratory for two type III tires (see fig. 32(b)), the fore-and-aft stiffness of tires of this type is almost the same as for the type VII tires and can be described by the equation

$$K_x = 0.53d(p + 4p_r)\sqrt[3]{\delta_o/d} \qquad \text{(Type III)} \qquad (48)$$

However, according to the static data of references 3 and 48 for several German aircraft tires, the constant k_1 appears to be almost twice as large $(k_1 \approx 1.1)$ as for the types VII and III tires; therefore, these tires roughly obey the equation

$$K_x = 1.1d(p + 4p_r)\sqrt[3]{\delta_o/d} \qquad \text{(German)} \qquad (49)$$

(see fig. 32(c)). Finally, according to some dynamic free-vibration-test data from reference 25 (see fig. 32(d)) for a pair of 26×8 tires at frequencies near 4 cycles per second and an amplitude of $\lambda_x \approx 0.1$ inch,

$$K_x \approx 1.5d(p + 4p_r)\sqrt[3]{\delta_o/d} \qquad (50)$$

(Eq. (50) is unfortunately not very reliable since the value of p_r used in conjunction with these data was not known and had to be assumed.)

In order to explain the large difference (over 2 to 1) between the equations for the different tire types, it should be recognized that, since the effect of inflation pressure on the stiffness is small, the tire stiffness is controlled largely by the tire-carcass properties. Moreover, tire-carcass construction might vary appreciably for different types of tires. Consequently, it seems too much to hope to obtain a simple accurate equation for fore-and-aft stiffness of all tires without going into the tire construction in great detail.

The preceding observations suggest tentatively that the fore-and-aft spring constant for types VII and III tires can be computed by equations (47) and (48) and for other types of tires by the equation

$$K_x = 0.8d\left(p + 4p_r\right)\sqrt[3]{\delta_o/d} \qquad (51)$$

Equation (51) is approximately the average of equations (47) to (49).

At rated tire deflection and rated inflation pressure, equations (47) and (48) both reduce approximately to the same relation:

$$K_x = 1.2pd \quad \text{(Types III and VII)} \qquad (52)$$

Vertical-Force Center of Pressure

Under the influence of a fore-and-aft or drag force the vertical-force center of pressure shifts a distance $c_x\lambda_x$ in the direction of the applied force, where λ_x represents the fore-and-aft deflection of the base of the tire and the parameter c_x represents the fraction of the distance λ_x through which the vertical-force center of pressure moves. (See fig. 30.) The only available data on this subject are shown in figure 33. These data, for a 56×16-32PR-VII tire, indicate that approximately

$$c_x = 0.25 \qquad (53)$$

Vertical Sinking

Upon application of a fore-and-aft force, a standing tire sinks vertically through the small distance δ_x, which, according to the experimental evidence of reference 21 for a 56×16-32PR-VII tire, is approximately equal to 10 percent of the fore-and-aft deflection or

$$\delta_x = 0.1\left|\lambda_x\right| \qquad (54)$$

where $\left|\lambda_x\right|$ denotes the absolute value of the fore-and-aft deflection.

Circumferential Distortion

Under the influence of a fore-and-aft force, according to the experimental data of reference 3, the following state of deformation exists on a standing tire (see fig. 30): As the base of the tire is deflected a distance λ_x by the fore-and-aft load, the major part of the tire equator (except near the ground) rotates about the wheel center through a small displacement u roughly equal to about 20 percent of the base deflection λ_x. Some sample data from reference 3 illustrating this effect are shown in figure 30.

Near the ground, according to reference 48, the circumferential displacement u is apparently close to an exponential function of the peripheral distance from the ground s or

$$u = \lambda_x e^{-s/J}$$

and the corresponding elongation strain ϵ_x for the right-hand side of the tire in figure 30 is then

$$\epsilon_x = -\frac{du}{ds} = \frac{\lambda_x}{J} e^{-s/J} \tag{55}$$

where J is a tire constant which is analogous to the static relaxation length for lateral deformation and which is called the circumferential decay length. This constant J, according to experimental data from reference 48 for only one test condition, is approximately equal to one-half the tire radius or

$$J = 0.5r \tag{56}$$

The only other available data for a standing tire which are pertinent to this subject are the experimental data from the tests of reference 3 for several German aircraft tires. (For example, see fig. 30.) The tire circumferential distortion data from these tests were taken for too few circumferential positions (see fig. 30) to provide reliable determinations of the circumferential decay length; and whereas these data indicate that the decay length predicted by equation (56) is of the correct order of magnitude, they are inadequate to insure the reliability of the equation.

Some further discussion of the circumferential decay length for the case of a rolling tire is given in a subsequent section of this paper. (See section entitled "Braking Force for Small Slip Ratios.")

COMBINED VERTICAL LOADING AND TILT

Lateral Force

If a standing tire at a vertical load F_z is laterally tilted without lateral deformation of the tire equator in contact with the ground $\left(\lambda_o = 0\right)$, there arises a corresponding lateral ground force $F_{y,\gamma}$ which, for small tilt angles, is directly proportional to the tilt angle γ (see fig. 34), the constant of proportionality being designated as $-K_\gamma$ where γ is taken in radians:

$$F_{y,\gamma} = -K_\gamma \gamma \tag{57}$$

According to some experimental data obtained in static-tilt tests for a 45×15-14PR-III(15.50-20) tire at approximately rated conditions (see fig. 35), the relation between K_γ and F_z is approximately

$$K_\gamma = 0.57F_z \tag{58}$$

The major reasons for the existence of this tilt force have been discussed by Rotta. (See ref. 44 or 45.) Rotta has also made some theoretical calculations of this tilt force, which are reproduced in figure 36 together with the experimental data. (The quantity H in the parameter H/w for this figure is defined as tire radius minus rim radius.) These theoretical curves give some indications of the effects of vertical deflection and of the parameter H/w on the tilt force; and although they do not appear to be in good agreement with the limited experimental data, they should at least be useful as a standard for extrapolating the experimental data.

Vertical-Force Center of Pressure

The vertical-force center of pressure of a standing tilted tire is laterally displaced from the intersection of the wheel center plane and the ground plane by an amount $c_\gamma \gamma$ where c_γ is the lateral shift per radian of tilt. (See fig. 34(a).) For a rigid toroidal tire of circular cross section, this shift parameter c_γ would be equal to

$$c_\gamma = 0.5w \tag{59}$$

(See fig. 34(b).) The only available experimental data pertinent to this subject are shown in figure 37. These data were obtained from the previously mentioned static-tilt tests of a 45×15-14PR-III(15.50-20) tire at approximately rated conditions. The data are seen to indicate that the actual value of c_γ, at least for these conditions, is approximately equal to the value given by equation (59), or more accurately by the equation

$$c_\gamma = 0.48w \tag{60}$$

PROPERTIES OF A ROLLING OR ROTATING TIRE

This section of this paper considers the following properties of a rolling or rotating tire: rolling relaxation lengths, rolling radius, yawed-rolling characteristics, braking force for small slip ratios, turning moment for curvilinear rolling, tilted-rolling characteristics, and vertical-force-deflection characteristics.

ROLLING RELAXATION LENGTHS

In this section the tire property of relaxation length as applied to several cases of rolling motion is defined and discussed. A previous section discussed the corresponding quantity for a standing tire.

Unyawed-Rolling Relaxation Length

The original definition of tire relaxation length was given as follows by Temple in reference 55: Consider the situation wherein the base or ground-contact area of an unyawed tire is laterally deflected relative to the wheel and the wheel is then rolled straight ahead in its initial plane. After the tire has rolled forward a distance equal to the footprint length, according to the experiments of Kantrowitz (ref. 30) and others, the lateral deflection of the center of the ground-contact area λ_o dies out exponentially with the distance x rolled. The distance that the tire must roll forward in order for the lateral deformation to drop to a fraction $1/e$ of its initial value has been defined as the relaxation length of the tire. In other words, the variation of lateral deformation λ_o with distance x rolled is governed by an equation of the type

$$\lambda_o = A_1 e^{-x/L_\lambda} \tag{61}$$

where A_1 is a constant depending on the initial lateral deformation and L_λ is the relaxation length. In order to distinguish this particular type of relaxation length from the others discussed in this paper, it is henceforth called the unyawed-rolling-deflection relaxation length.

Another way to define an unyawed-rolling relaxation length is to consider the decay of the tire lateral force F_y with distance x rolled for the rolling conditions previously described. Since lateral force is roughly proportional to lateral deformation, equation (61) also indicates that the lateral force would decrease exponentially with distance rolled according to a relation of the form

$$F_y = A_2 e^{-x/L_f}$$

where A_2 is a constant depending on the initial lateral force and L_f is a constant which is called the unyawed-rolling-force relaxation length and which should be essentially the same as L_λ.

The available experimental measurements of these two unyawed-rolling relaxation lengths are shown in figure 38 in the form of a relaxation-length parameter similar to the one obtained from the previous analysis of the static relaxation length (fig. 25). Also shown in figure 38 is the empirical equation

$$L_f = L_\lambda = \left(2.8 - 0.8p/p_r\right)\left(1.0 - 4.5\delta_o/d\right)w \qquad (62)$$

which was previously obtained for the static relaxation length L_s. (See eq. (43) and fig. 25.) The two types of unyawed-rolling relaxation length in figure 38 are seen to be similar to each other and are about the same as or slightly smaller than the corresponding static relaxation lengths which are represented by the empirical equation.

Yawed-Rolling Relaxation Length

Another definition of rolling relaxation length may be obtained by consideration of the experiment in which a wheel is set up at an angle of yaw and is then rolled straight ahead at this constant angle. If no appreciable skidding occurs, then, according to theory (ref. 48) and to experiments (for example, refs. 22 to 24), the tire builds up a lateral force which exponentially approaches an end-point condition for steady yawed rolling; that is, the lateral force $F_{y,r}$ builds up with distance x rolled according to a relation of the form

$$F_{y,r} = F_{y,r,e} - A_3 e^{-x/L_y} \tag{63}$$

where $F_{y,r,e}$ is the steady-state force, A_3 is a constant which depends on the initial tire distortion, and L_y is called the yawed-rolling relaxation length.

The available experimental yawed-rolling relaxation-length data are shown in figure 39 in the form of the relaxation-length parameter suggested by the previous analysis of the static relaxation length. Also shown is a solid line which represents the static-test data (see eq. (43)) and a dashed line which represents the equations

$$\left.\begin{aligned}
\frac{L_y}{2.8 - (0.8p/p_r)} &= 11\delta_o/d && (\delta_o/d \leqq 0.053) \\
\frac{L_y}{2.8 - (0.8p/p_r)} &= (64\delta_o/d) - 500(\delta_o/d)^2 - 1.4045 && (0.053 \leqq \delta_o/d \leqq 0.068) \\
\frac{L_y}{2.8 - (0.8p/p_r)} &= 0.9075 - (4\delta_o/d) && (0.068 \leqq \delta_o/d)
\end{aligned}\right\} \tag{64}$$

which are empirical equations fitted to the yawed-rolling data. For large vertical deflections the yawed-rolling and static relaxation lengths appear to be similar, the yawed-rolling relaxation length being usually somewhat smaller. However, for small vertical deflections there is a definite difference between the two; the yawed-rolling relaxation length appears to increase with increasing deflection whereas the static relaxation length (see solid line of fig. 39 or experimental data in fig. 25) decreases with increasing vertical deflection. The reasons for this difference are not known.

ROLLING RADIUS

The rolling radius of a tire r_e is a tire parameter which is used to correlate the angular and horizontal displacements and velocities of a rolling wheel. It is defined (this definition differs slightly from the definition of refs. 22 and 23) as the ratio of the horizontal displacement of the wheel axle dx to the angular displacement of the wheel dθ, or as

$$r_e = \frac{dx}{d\theta} \equiv \frac{v_H}{\omega} \tag{65}$$

where $v_H\left(= \frac{dx}{dt}\right)$ is the horizontal velocity of the wheel axle and $\omega\left(= \frac{d\theta}{dt}\right)$ is the angular velocity of the wheel. (It is, of course, not equal to either the free or the deflected geometric radius of the tire.) This rolling radius is a variable quantity which is influenced primarily by the tire vertical deflection δ_o, the tire drag force F_x, and the tire yaw angle ψ. The symbol $r_{e,o}$ is used to represent the rolling radius for the special case of unyawed and unbraked rolling.

Effect of Vertical Deflection

The effect of vertical deflection on the rolling radius of a tire has been calculated by Whitbread on the basis of some simplified assumptions regarding the tire distortion in the ground-contact region. (See ref. 18.) He arrived at the final approximate equation

$$r_{e,o} = r - \frac{1}{3}\delta_o \tag{66}$$

Whitbread also conducted some experiments with two 6.8-inch-diameter and 10-inch-diameter aircraft tires which roughly confirmed this equation. (See ref. 18.)

Additional data which, in general, support this equation are shown in figure 40 for a number of type VII aircraft tires ranging from 26 to 56 inches in diameter for inflation pressures close to the rated pressure.

Equation (66) does not take into account the effect of tire inflation pressure on the rolling radius. Such an effect does exist, and its order of magnitude is indicated in figure 41 for a pair of 56×16-24PR-VII-R22 tires. However, this figure shows that, for a change of 4 to 1 in inflation pressure, the change in rolling radius is only about ±1 percent from the mean value for the range of the experimental data shown.

Effect of Braking

If a braking force F_x is applied to a rolling tire, its rolling radius r_e will increase. This increase may be explained by the following discussion.

Consider the behavior of a small incremental segment of the tire equator as the tire rolls ahead. When this segment is far from the ground-contact area, it has some undistorted length ds_o shown in the following sketch:

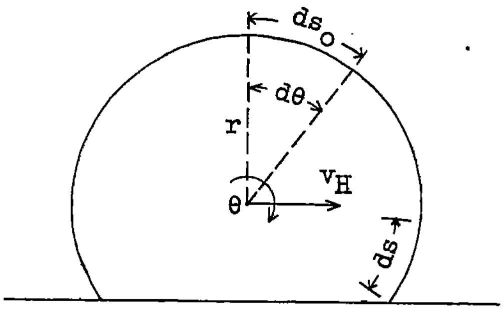

However, as the tire rolls ahead and this segment is just about to enter the ground-contact region, its length has changed to a new value ds as a consequence of the strains produced by the vertical and drag forces acting on the tire in the ground-contact region, or, in other words

$$ds = ds_o\left(1 + \epsilon_z + \epsilon_x\right) \tag{67}$$

where ϵ_z is the elongation strain produced by the vertical force (always negative) and ϵ_x is the elongation strain produced by the drag force.

According to the experimental evidence of references 32 and 51, for small braking forces the tire equator does not skid with respect to the ground in most of the forward or leading half of the ground-contact area. This result implies that as the tire rolls ahead a distance dx an equal length of strained tire equator ds is laid down on the ground; that is,

$$ds = dx \tag{68}$$

The corresponding incremental rotation $d\theta$ of the solid wheel parts in radians is equal to the ratio of the undistorted length of the equator segment laid down on the ground to the tire free radius r or

$$d\theta = \frac{ds_o}{r} \tag{69}$$

as illustrated in the preceding sketch.

The rolling radius of the braked tire, which is defined by equation (65) as $r_e = \frac{dx}{d\theta}$, can now be obtained by combination of equations (67), (68), and (69) as

$$r_e = \frac{dx}{d\theta} = r + r\epsilon_z + r\epsilon_x \tag{70}$$

The expression $r + r\epsilon_z$ in equation (70) represents the rolling radius for unbraked rolling $r_{e,o}$, which has been evaluated in the preceding section (see eq. (66)). Hence, equation (70) can be restated in the form

$$r_e = r_{e,o} + r\epsilon_x \tag{71}$$

where $r_{e,o}$ is given by equation (66). The quantity ϵ_x, which represents the strain due to drag at the leading edge of the ground-contact area, can be obtained from equation (55) (by setting $s = 0$) as

$$\epsilon_x = \frac{\lambda_x}{J} \tag{72}$$

Thus, equation (71) can be rewritten in the form

$$r_e = r_{e,o} + \frac{r}{J}\lambda_x \tag{73}$$

or, since $F_x = K_x\lambda_x$ (where K_x is the fore-and-aft spring constant),

$$r_e = r_{e,o} + \frac{rF_x}{JK_x} \tag{74}$$

Equation (74) is converted to another form in a subsequent section of this paper (see section entitled "Braking Force for Small Slip Ratios") and is therein compared with some limited experimental data for one 48×17-16PR-III(17.00-20)RU tire. From this limited comparison, the value of J appears to be approximately equal to r for braked rolling conditions; hence, equations (73) and (74) can be written in the form

$$r_e = r_{e,o} + \lambda_x \tag{75a}$$

$$r_e = r_{e,o} + \frac{F_x}{K_x} \tag{75b}$$

Finally, by inserting equation (66) into equations (75a) and (75b), the rolling radius for braked rolling can be expressed in terms of vertical deflection δ_o and drag force or fore-and-aft deflection as

$$r_e = r - \frac{1}{3}\delta_o + \frac{F_x}{K_x} \tag{76a}$$

or

$$r_e = r - \frac{1}{3}\delta_o + \lambda_x \tag{76b}$$

Effect of Yaw

In the presence of a finite yaw angle ψ the rolling radius r_e increases with increasing yaw angle. According to the experimental evidence of references 22 and 23, the product $r_e \cos \psi$ appears to be largely independent of yaw angle for any given initial vertical deflection (see, for example, fig. 42); that is,

$$r_e = \frac{r_{e,o}}{\cos \psi} \tag{77}$$

where $r_{e,o}$ is the rolling radius for zero yaw. By substituting equation (66) into equation (77), the rolling radius for yawed rolling can be expressed in terms of initial vertical deflection δ_o and yaw angle as

$$r_e = \frac{r - \frac{1}{3}\delta_o}{\cos \psi} \tag{78}$$

YAWED-ROLLING CHARACTERISTICS

General Observations

Consider the condition in which a wheel is yawed with respect to its direction of motion by an angle ψ and is then rolled straight ahead with this yaw angle held constant. The major quantities of interest for these rolling conditions are the cornering force $F_{y,r}$ (ground lateral force perpendicular to direction of motion), the normal force $F_{\psi,r}$ (ground lateral force perpendicular to wheel plane), the self-alining torque $M_{z,r}$ (ground moment about a vertical axis through the wheel center point), and the pneumatic caster or center-of-pressure distance of the normal force q $\left(q = M_{z,r}/F_{\psi,r}\right)$.

For a given condition of pressure and vertical deflection, as the wheel rolls forward the cornering force builds up with distance rolled in the manner illustrated in figure 43. The initial slopes of these force-distance curves are seen to increase roughly linearly with increasing yaw angle, as would be expected from the theory of reference 48.

Steady-State Conditions

After a steady-state yawed-rolling condition is reached, the steady-state normal force $F_{\psi,r,e}$, cornering force $F_{y,r,e}$, self-alining torque $M_{z,r,e}$, and pneumatic caster q, as functions of yaw angle, vary in the manner illustrated in figures 44 and 45. These quantities and the tire cornering power are discussed and analyzed separately in the following sections.

Normal force.- The normal force generally increases with increasing yaw angle, linearly for small yaw angles, and eventually tends asymptotically to a maximum value determined by the product of the coefficient of friction μ_ψ and the vertical load F_z (see, for example, fig. 44 or ref. 13, 18, 19, or 22). Most of the available data on this subject for modern tires are plotted in figure 46 in terms of the dimensionless ratios $\frac{F_{\psi,r,e}}{\mu_\psi F_z}$ and $\frac{N\psi}{\mu_\psi F_z}$, where N is the cornering power or initial slope of the curve of normal force plotted against yaw angle $\left(N = \left(\frac{dF_{\psi,r,e}}{d\psi}\right)_{\psi \to 0}\right)$.

It might be noted from figure 44(a) or figure 46, both of which are typical for vertical deflections up to and slightly over rated deflection, that the slope of the curve of normal force plotted against yaw angle always decreases with increasing yaw angle, whereas for very large vertical deflections (see fig. 44(b) or fig. 47) this curve appears to have a point of inflection.

For vertical deflections up to approximately rated deflection, the experimental variations can be predicted with fair accuracy by the empirical equations

$$\left.\begin{aligned} \frac{F_{\psi,r,e}}{\mu_\psi F_z} &= \phi - \frac{4}{27}\phi^3 \qquad (\phi \leqq 1.5) \\ \frac{F_{\psi,r,e}}{\mu_\psi F_z} &= 1 \qquad (\phi \geqq 1.5) \end{aligned}\right\} \tag{79}$$

where

$$\phi = \frac{N}{\mu_\psi F_z}\psi \tag{80}$$

(See figs. 46(a) to (46(c).) However, for larger vertical deflections, the variation appears to depend on the vertical deflection and, even for the same vertical deflection, appears to be different for different tires. (See fig. 47.)

Cornering force.- The cornering force $F_{y,r,e}$ (perpendicular to the direction of motion) is slightly smaller than the corresponding normal force $F_{\psi,r,e}$ (perpendicular to the wheel plane), as is indicated in figure 45. Apparently, the difference between these forces can usually be predicted with reasonable accuracy by the equation

$$F_{y,r,e} = F_{\psi,r,e} \cos \psi \tag{81}$$

as is also indicated in figure 45.

Cornering power.- The cornering power N of a tire is defined as the rate of change of cornering force $F_{y,r,e}$ with yaw angle ψ for $\psi \rightarrow 0$. Sample data illustrating the variation of cornering power with vertical deflection δ and inflation pressure p are shown in figure 48 for a pair of 56x16-24PR-VII-R22 tires. Data of this type indicate that cornering power increases with increasing vertical deflection for small vertical deflections up to a maximum value and then decreases. In addition, cornering power appears to increase approximately linearly with increasing inflation pressure.

Analysis of the available experimental data on cornering power for modern types I, III, and VII tires resulted in the following empirical equations for cornering power:

$$\left.\begin{aligned}\frac{N}{C_c\left(p + 0.44p_r\right)w^2} &= 1.2(\delta/d) - 8.8(\delta/d)^2 \qquad (\delta/d \leqq 0.0875)\\ \frac{N}{C_c\left(p + 0.44p_r\right)w^2} &= 0.0674 - 0.34(\delta/d) \qquad (\delta/d \geqq 0.0875)\end{aligned}\right\} \qquad (82)$$

where the cornering-power coefficient C_c is given by the following table:

Tire type	Value of C_c for -	
	N, force/radian	N, force/deg
I	63	1.1
III	69	1.2
VII	57	1.0

The available experimental data are compared with the predictions of equations (82) in figure 49 for a wide range of vertical deflections and inflation pressures. In figure 49(a) the empirical equation appears to give predictions which are accurate within about 20 percent for the type VII tires. Figure 49(b) indicates that the shape of the empirical curve (which was determined mostly from the data for the type VII tires) does not describe very well the shape of the experimental curves for types I and III tires. However, since the available data for types I and III tires are very limited, an attempt to establish different types of empirical equations for these tires did not seem to be justified.

Since equations (82) appear to be of limited accuracy, at least for types I and III tires, the cornering power might alternately be calculated from the theoretical equations

$$\left.\begin{aligned} N &= \left(L_y + h\right)K_\lambda \quad \text{per radian} \\ N &= \frac{\pi}{180}\left(L_y + h\right)K_\lambda \quad \text{per degree} \end{aligned}\right\} \qquad (83)$$

(see, for example, ref. 48 or 52) which express the cornering power as a function of lateral spring constant K_λ, half-length of footprint h, and relaxation length L_y. Some comparisons of experimental cornering-power data with values calculated from equations (83) are shown in table II. (Since all the parameters involved in the calculations were not measured under identical conditions of deflection and pressure, it was necessary to interpolate slightly the experimental data from the pertinent references; moreover, since K_λ depends slightly on the amplitude of lateral deformation (see fig. 19), it was sometimes necessary to use mean values of K_λ.)

Table II shows that the values of cornering power calculated from equations (83) are in fairly good agreement with the experimental values for vertical deflections up to somewhat above rated deflection $\left(\delta_r/d \approx 0.07\right)$, but the calculated values are appreciably higher for very large vertical deflections.

In regard to the effects of rolling velocity on cornering power, about the only available pertinent experimental data appear to be the data of reference 13 (for speeds up to 45 miles per hour), reference 27 (for speeds up to 56 miles per hour), reference 29 (for speeds up to 95 miles per hour, and reference 43 (for speeds up to 100 miles per hour). While some of these data indicate a slight decrease in cornering power with increasing speed, most data indicate no definite appreciable effects of speed even up to 100 miles per hour.

Self-alining torque.- Most available data for the variation of self-alining torque $M_{z,r,e}$ with yaw angle ψ for modern tires are presented in figure 50 in terms of the dimensionless ratios $\frac{M_{z,r,e}}{\mu_\psi F_z h}$ and $\frac{N}{\mu_\psi F_z}\psi$. This figure shows that most of these data can be approximately described by the empirical equations

$$\left.\begin{aligned}
\frac{M_{z,r,e}}{\mu_\psi F_z h} &= 0.8\phi && (\phi \leqq 0.1) \\
\frac{M_{z,r,e}}{\mu_\psi F_z h} &= \phi - \phi^2 - 0.01 && (0.1 \leqq \phi \leqq 0.55) \\
\frac{M_{z,r,e}}{\mu_\psi F_z h} &= 0.2925 - 0.1\phi && (\phi \geqq 0.55)
\end{aligned}\right\} \qquad (84)$$

where

$$\phi = \frac{N}{\mu_\psi F_z} \psi$$

The maximum self-alining torque, according to equations (84), is equal to

$$M_{z,r,e,max} = 0.24\mu_\psi h F_z \qquad (85)$$

Pneumatic caster.- Most of the available data for modern tires for the variation with yaw angle ψ of the pneumatic caster q are presented in figure 51 in terms of the dimensionless ratios $\frac{q}{h}$ and $\frac{N}{\mu_\psi F_z} \psi$. In this figure,

$$q = M_{z,r,e} \big/ F_{\psi,r,e} \qquad (86)$$

and h is the tire half-footprint length for zero yaw as estimated from static-test data. Also shown in this figure is the variation calculated from the following empirical equations which were obtained by combination of the corresponding force and moment equations (79) and (84) with the definition of pneumatic caster (eq. (86)).

$$\left.\begin{aligned}
\frac{q}{h} &= 0.8\bigg/\left(1 - \frac{4}{27}\phi^2\right) && (\phi \leqq 0.1) \\
\frac{q}{h} &= \left(\phi - \phi^2 - 0.01\right)\bigg/\left(\phi - \frac{4}{27}\phi^3\right) && (0.1 \leqq \phi \leqq 0.55) \\
\frac{q}{h} &= (0.2925 - 0.1\phi)\bigg/\left(\phi - \frac{4}{27}\phi^3\right) && (0.55 \leqq \phi \leqq 1.5) \\
\frac{q}{h} &= 0.2925 - 0.1\phi && (\phi \geqq 1.5)
\end{aligned}\right\} \qquad (87)$$

where

$$\phi = \frac{N}{\mu_\psi F_z}\psi$$

Fair agreement between calculation and experiment is seen to exist, the agreement being best for the 40×12 tires. However, since the agreement appears to be far from perfect, it should be noted that the accuracy of the experimental data shown is not extremely high and is particularly poor for the small yaw angles. Also, the data for the 40×12 tires, from a consideration of instrument accuracy and test procedure alone, should be much more reliable than the data for the 26×6.6 and 56×16 tires.

Coefficient of friction.- Since the dimensionless plots of experimental data on yawed-rolling characteristics shown in figures 46, 47, 50, and 51 involve the corresponding yawed-rolling coefficient of friction μ_ψ as a parameter, it appears pertinent to indicate herein something as to the size of this coefficient for these particular data and its variation for other test conditions. The data for yawed-rolling coefficient of friction corresponding to the experimental data in these four figures are plotted against bearing pressure p_n in figure 52. All these data were obtained on a dry reinforced-concrete taxi strip at rolling speeds of about 1 to 2 miles per hour. Also shown in figure 52 are some coefficients of friction obtained from locked-wheel sliding-drag tests of the same tires on the same taxi strip at speeds of about 10 inches per minute. The coefficients of friction from both sets of data indicate a decrease of coefficient of friction with increasing bearing pressure which can be approximately predicted by the empirical equation

$$\mu_\psi = \mu_{x,s} = 0.93 - 0.0011p_n \qquad (88)$$

where p_n is in pounds per square inch.

Equation (88) may furnish a reasonable first approximation for the coefficient of friction on dry concrete runways at very low taxi speeds, but does not, of course, take into account many other important factors such as temperature, skidding velocity, slip ratio, surface roughness, and surface wetness, which factors may considerably influence the coefficient of friction. While a discussion of these factors is beyond the scope of this paper, it might be noted that some pertinent information on them is contained in references 2, 13, 20, 31, 34, 40 to 42, and 46.

BRAKING FORCE FOR SMALL SLIP RATIOS

When a braking force is applied to a rolling tire, the relationship between the braking force F_x and the slip ratio s_1 (see section entitled "Definitions") is given by curves of the type shown in figure 53. For small slip ratios the braking force appears to increase linearly with increasing slip ratio. This linear variation may be approximately predicted by making use of the equation previously derived for the effect of braking force on the rolling radius r_e (eq. (74)) and the definition of slip ratio in terms of rolling radius (eq. (2)). These two equations provide the following relationship between braking force and slip ratio for small slip ratios:

$$F_x = JK_x \frac{r_e}{r} s_1$$

or since r_e is approximately equivalent to r,

$$F_x = JK_x s_1 \tag{89}$$

In order to use equation (89), the tire circumferential decay length J must be expressed in terms of the tire dimensions. According to some preliminary experimental braking data obtained by the General Aerodynamics Branch of the Langley Laboratory for a 48×17-16PR-III(17.00-20)RU tire (see fig. 54), it appears that approximately

$$J = r$$

so that equation (89) takes the form

$$F_x = rK_x s_1 \tag{90}$$

(Consideration of the available static-test data pertinent to the decay length J led to the equation $J = 0.5r$ (eq. (56)); however, since eq. (56) was based largely on a single test point and since the determination of this decay length from experimental data is usually a highly critical process, it would not be surprising if eq. (56) were considerably in error for the static decay length. Of course, the possibility also exists that the decay length is different for static and rolling conditions, as appears to be the case for the analogous static and rolling relaxation lengths.)

Equation (90) probably furnishes an approximate estimate of the relationship between braking force and slip ratio for small slip ratios. However, since data suitable for checking the validity of the equation are limited to a single aircraft tire (see fig. 54), it might be noted that Hadekel (ref. 18) has indicated that the available experimental data for small slip ratios for automobile and motorcycle tires (refs. 13 and 2, respectively) can be described by the empirical relation

$$F_x = 14F_z s_1 \tag{91}$$

within an error of about ±20 percent. Comparison of the prediction of this equation with the aircraft tire data shown in figure 54 indicates fair agreement but indicates that the prediction of the equation is somewhat high.

TURNING MOMENT FOR CURVILINEAR ROLLING

When an unyawed wheel rolls along a circular path (or any other curved path), it experiences an elastic ground moment $M_{z,R}$ which tends to turn the wheel out of the circle. (See following sketch.)

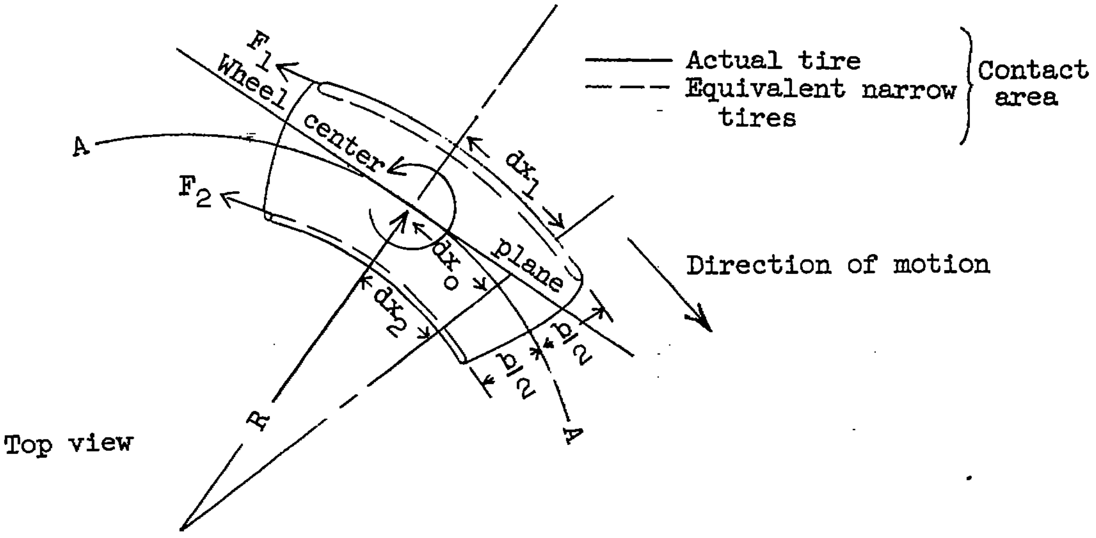

This turning moment arises as a consequence of tire circumferential stresses and has been partly explained by Von Schlippe and Dietrich (ref. 48) and by Fromm (ref. 16). A simplified qualitative version of their explanation follows.

As a first approximation, a tire having the finite footprint width b can be considered to behave in a manner which is qualitatively similar to the behavior of two very narrow tires mounted rigidly on the same axle at a distance b apart. Next, consider the motion of these two coupled equivalent tires as the overall wheel system moves along the circular path AA in the preceding sketch. As the overall wheel system moves forward a distance dx_o and rotates through an angle $d\theta$, the outboard tire moves a distance $dx_1 = dx_o\left[R + (b/2)\right]/R$ (where R is the radius of the path curvature) and the inboard tire moves a distance $dx_2 = dx_o\left[R - (b/2)\right]/R$. Since the angular displacement $d\theta$ is the same for both coupled tires, the corresponding rolling radii $\left(r_e = \frac{dx}{d\theta}\right)$ are

$$r_{e,o} = \frac{dx_o}{d\theta} \tag{92}$$

$$r_{e,1} = \frac{dx_o}{d\theta}\,\frac{R + (b/2)}{R} = r_{e,o}\left(1 + \frac{b}{2R}\right) \tag{93}$$

$$r_{e,2} = \frac{dx_o}{d\theta}\,\frac{R - (b/2)}{R} = r_{e,o}\left(1 - \frac{b}{2R}\right) \tag{94}$$

According to equation (75b), for small slip ratios (that is, for small differences between r_e and $r_{e,o}$), the drag force F_x acting on a rolling unyawed tire is approximately equal to

$$F_x = P\left(r_e - r_{e,o}\right) \tag{95}$$

where

$$P = K_x \tag{96}$$

Another not necessarily identical form for this parameter P can be obtained by using the approximate relationship $rK_x = 14F_z$, which is obtained from a comparison of equations (90) and (91)

$$P = 14F_z/r \tag{97}$$

If the corresponding drag forces for each of the two equivalent tires here are assumed to obey laws similar to equation (95), then, for the outboard tire in the sketch, the drag force F_1 is

$$F_1 = C_b P\left(r_{e,1} - r_{e,o}\right) = C_b P r_{e,o} \frac{b}{2R} \tag{98}$$

(see eqs. (93) and (95)), where C_b is a proportionality constant. Similarly, for the inboard tire,

$$F_2 = -C_b P r_{e,o} \frac{b}{2R} \tag{99}$$

The corresponding ground moment $M_{z,R}$ is then (see sketch)

$$M_{z,R} = F_1(b/2) - F_2(b/2) \tag{100}$$

or, after substitution of equations (98) and (99)

$$M_{z,R} = \frac{C_b P b^2 r_{e,o}}{2R} \tag{101}$$

In terms of path curvature $\left(\frac{d^2y}{dx^2} = \frac{1}{R} \text{ for large } R\right)$ and tire radius $\left(\text{with the assumption that } r_{e,o} \approx r\right)$:

$$M_{z,R} \approx \frac{1}{2} C_b r P b^2 \frac{d^2y}{dx^2} \tag{102}$$

Experimental data suitable for evaluating the constant C_b are available in reference 23 for one 26×6.6-12PR-VII tire for three curvature conditions (R = 4.71, 9.83, and 14.70 feet) and in reference 48 for a 10×3 tire for one curvature condition (R = 1 meter). Use of the experimental data of reference 23 to evaluate C_b in conjunction with equations (96) and (102) leads to the following equation for M_R

$$M_{z,R} = 0.034 r b^2 K_x \frac{d^2y}{dx^2} \tag{103}$$

corresponding to $C_b \approx 0.067$, and, in conjunction with equations (97) and (102), leads to the equation

$$M_{z,R} = 0.24F_z b^2 \frac{d^2y}{dx^2} \tag{104}$$

corresponding to $C_b \approx 0.034$. The corresponding constants for equations (103) and (104) as obtained by use of the experimental data of reference 48 are 0.012 and 0.17, respectively, as compared with 0.034 and 0.24 from reference 23. However, the latter set of numbers are probably more realistic, since the tire of reference 48 had an untypical diamond-shaped footprint pattern, whereas the tire of reference 23 had a more typical ellipse-shaped footprint. Consequently, it is suggested that either equation (103) or (104) be used for computing tire rolling moments due to path curvature.

This completes the discussion of the rolling moment in curvilinear rolling. However, for the sake of a later derivation on tilted rolling moments, it is convenient to express here the drag forces F_1 and F_2 on the two equivalent tires in terms of their respective rolling radii. The relation for F_1 is obtained by substituting the experimental value of C_b and the definition of P (eq. (96)) into equation (98) (see also eq. (56)). This substitution gives the equation

$$F_1 = 0.067K_x\left(r_{e,1} - r_{e,o}\right) \tag{105}$$

and similarly for F_2,

$$F_2 = 0.067K_x\left(r_{e,2} - r_{e,o}\right) \tag{106}$$

ROLLING CHARACTERISTICS OF A TILTED TIRE

During the straight-line steady-state rolling of an unyawed tilted tire, the tire experiences a lateral force (for example, see fig. 55(a)) and a turning moment. This force and moment are discussed in this section.

Lateral Force

The lateral force for unyawed tilted-rolling conditions probably results from two or more separate causes. The first and apparently primary cause for the side force, as was pointed out by Rotta (ref. 45), is the static lateral force due to tilt previously discussed (see eq. (57)). A second possible cause for side forces arises if the rolling motion of a tilted tire is of such a nature that it leads to lateral equator deformation λ_o and, consequently, to lateral force of an amount $K_\lambda \lambda_o$ (where K_λ is the lateral spring constant). According to the solution of equation (16) of reference 52, the lateral deformation λ_o for steady tilted rolling at a tilt angle γ (in radians) is equal to

$$\lambda_o = -\frac{\xi h L}{r}\gamma \tag{107}$$

where h is the footprint half-length, L is the appropriate type of relaxation length, and r is the tire free radius. The parameter ξ is a numerical constant associated with tilt and is discussed in detail in reference 52. Although the magnitude of ξ is unknown, the discussion and experimental evidence of reference 52 indicate that it is much smaller than unity. The direction of this lateral deformation is such that the ground-contact part of the tire tends to be deflected toward the center of the wheel axle as is indicated in the following rear-view sketch:

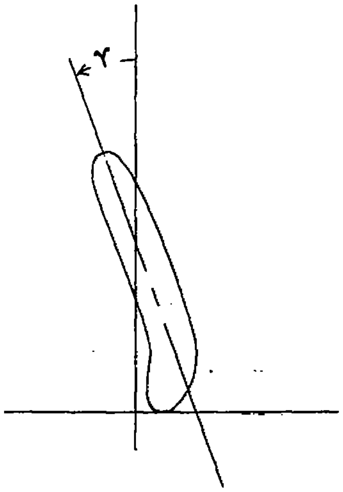

The lateral force corresponding to this deformation (eq. (107)) is

$$F_{y,\lambda} = K_\lambda \lambda_o = -\frac{\xi hLK_\lambda}{r}\gamma \tag{108}$$

(It should be noted here that eq. (16) of ref. 52, on which eq. (107) is based, was derived upon considerations of a finite ground-contact area. Arguments which do not take this finite area into account, such as those of ref. 18, tend to lead to a greatly exaggerated view of the tire lateral deformation and of the corresponding lateral force.)

The total lateral force due to tilt $F_{y,\gamma,r}$ for a steadily rolling tire is given by the sum of equations (57) and (108) as

$$F_{y,\gamma,r} = -\left(K_\gamma + \frac{\xi hLK_\lambda}{r}\right)\gamma \tag{109}$$

where γ is in radians or,

$$F_{y,\gamma,r} = -K_{\gamma,r}\gamma \tag{110}$$

where

$$K_{\gamma,r} = K_\gamma + \frac{\xi hLK_\lambda}{r} \tag{111}$$

The only available experimental data pertinent to the lateral forces on rolling tilted aircraft tires are given in reference 35 and are reproduced in figure 55. From these data it appears that, to a rough approximation,

$$K_{\gamma,r} = F_z \tag{112}$$

where F_z is the vertical ground force. The experimental data of reference 5 for automobile tires are also in rough agreement with equation (112).

Turning Moment

During the tilted rolling of an unyawed tire, a turning moment $M_{z,\gamma}$ acts on the tire from the ground in the direction indicated in the top view of figure 56. Although the magnitude and importance of this moment have not yet been extensively investigated, a partial qualitative explanation of its origin has been given by Chudakov in reference 6. The following discussion of this moment is an extension of Chudakov's discussion and is very similar to the previous discussion concerning the rolling moment for curvilinear rolling.

As a first approximation, a tire of finite width behaves in a manner which is qualitatively similar to the behavior of two very narrow tires mounted rigidly on the same axle at a distance b (footprint width) apart. For the case of tilted rolling, these two equivalent tires have the individual vertical deflections δ_1 and δ_2 (see fig. 56), where

$$\delta_1 = \delta_o - \frac{b}{2}\gamma \tag{113}$$

$$\delta_2 = \delta_o + \frac{b}{2}\gamma \tag{114}$$

in which δ_o is the average or overall vertical deflection, δ_1 is the deflection of the left-hand equivalent tire in figure 56(b), δ_2 is the deflection for the right-hand tire, and γ is the tilt angle.

Consider now the rolling radii for the equivalent tire with the vertical deflection δ_1. If this tire were rolling freely, its rolling radius $r_{e,o,1}$ would be equal to $r - \frac{1}{3}\delta_1$ (see eq. (66)), or by application of equation (113),

$$r_{e,o,1} = r - \frac{1}{3}\delta_o + \frac{b}{6}\gamma \tag{115}$$

Similarly, for the equivalent tire with vertical deflection δ_2,

$$r_{e,o,2} = r - \frac{1}{3}\delta_o - \frac{b}{6}\gamma \tag{116}$$

However, since the two equivalent tires are considered to be coupled rigidly together on the same axle, they must have the same rolling radius r_e, which, as a first approximation, is equal to the average of the values given by equations (115) and (116) as

$$r_e = r - \frac{1}{3}\delta_o \tag{117}$$

As a consequence of the difference between the actual rolling radii and the rolling radii for free (unbraked) rolling, the individual equivalent tires behave like either braked or accelerated tires and experience different drag forces F_1 and F_2 (see, for example, the derivation of eq. (74)), which are given approximately by equations (105), (106), and (115) to (117) as

$$F_1 = 0.067K_x\left(r_e - r_{e,o,1}\right)$$

$$= -\frac{0.067}{6} bK_x\gamma \tag{118}$$

$$F_2 = \frac{0.067}{6} bK_x\gamma \tag{119}$$

The corresponding turning moment $M_{z,\gamma}$ about the wheel center is then

$$M_{z,\gamma} = F_2(b/2) - F_1(b/2)$$

$$= \frac{0.067}{6} b^2K_x\gamma$$

$$\approx 0.01b^2K_x\gamma \tag{120}$$

No definite conclusions can be reached in regard to the accuracy of equations (120), since the only available pertinent experimental data (ref. 7) are not complete enough to allow direct comparisons with the predictions of the equations.

VERTICAL FORCE-DEFLECTION VARIATION

In this section the variation of tire vertical force with vertical deflection for the case of landing or prerotation drop tests of a rotating or rolling tire is discussed. The case of a nonrotating tire has been treated in a previous section.

Apparent and Effective Tire Deflections

As a preliminary step for the subsequent discussion, it is important to distinguish between two types of tire deflection which are referred to as apparent tire deflection δ and effective tire deflection δ_e. The apparent tire deflection δ is defined as the change in wheel-axle height subsequent to ground contact, and the effective tire deflection δ_e is defined as the difference between the instantaneous free tire radius (which depends on wheel angular velocity) and the instantaneous distance from wheel axle to ground. Because of the change in wheel angular velocity during a drop or a landing involving wheel rotation, the tire radius may grow or shrink. Consequently, these two definitions are not identical, or, more specifically, the two types of tire deflection are related by the equation

$$\delta_e = \delta + \Delta r \tag{121}$$

where Δr is the increase in the tire radius subsequent to the instant of ground contact. It should be noted that the effective tire deflection is a direct measure of tire distortion, whereas the apparent tire deflection is not. On the other hand, in order to make time-history solutions of the equations of motion for a landing gear, the absolute positions of the wheels in space must be considered. These absolute positions are represented by the apparent tire deflection and not by the effective tire deflection.

Static-Force-Deflection Variation

As a second preliminary step, the equations previously obtained for the static-force-deflection variation of a standing tire (for increasing force) should be recalled and restated in the form

$$F_z = \left[p_o + \kappa p_{o,a}(\delta/w)^2 + 0.08p_r\right] w\sqrt{wd}\, f_1(\delta/w) \tag{122}$$

where

$$\left.\begin{aligned}
f_1(\delta/w) &= 0.96(\delta/w) + 0.216(\delta/w)^2/c_z \qquad && \left(\delta/w \leq \frac{10}{3} c_z\right) \\
f_1(\delta/w) &= 2.4\left[(\delta/w) - c_z\right] && \left(\delta/w \geqq \frac{10}{3} c_z\right)
\end{aligned}\right\} \tag{123}$$

(see eqs. (17) and (23)).

Force-Deflection Variation for Slow Rolling

Now consider the case of pure rolling (zero vertical velocity) at rolling speeds sufficiently small that inertia effects are negligible. According to some experimental measurements made with the equipment described in references 22 to 24 for two pairs of type VII tires (see fig. 57), the vertical-force-deflection relationship for a slowly rolling tire is essentially the same as the vertical-force-deflection relationship for the increasing-force branch of a static-force-deflection curve. It follows from this observation and from the previous analysis of the static-force-deflection relationship (see eq. (122)) that the vertical-force-deflection relationship for a slowly rolling tire can be fairly accurately predicted by use of equation (122).

Force-Deflection Variation for Landing Impact

Inertia effects.- Consider the case of the landing impact of a tire for large horizontal landing speeds where inertia effects may be important. For this case, it is important to recognize the difference noted previously between apparent tire deflection δ and effective tire deflection δ_e and to realize that the effective tire deflection is the deflection or distortion that determines the tire force. Hence, if equation (122) is to be extended to apply not only to the pure slow-rolling case, but also to the impact case, the expression δ/w in this equation must at least be replaced by δ_e/w in the function $f_1(\delta/w)$. (The other term involving $(\delta/w)^2$ is probably not critical enough to be worth modifying.) Thus,

$$F_z = \left[p_o + \kappa p_{o,a}(\delta/w)^2 + 0.08p_r\right] w\sqrt{wd}\, f_1\left(\delta_e/w\right) \qquad (124)$$

or, in terms of δ (which is the basic variable needed for theoretical solutions of landing impacts), this equation may be restated in the form

$$F_z = \left[p_o + \kappa p_{o,a}(\delta/w)^2 + 0.08p_r\right] w\sqrt{wd}\, f_1\left(\frac{\delta + \Delta r}{w}\right) \qquad (125)$$

(see eq. (121)).

Equation (125) takes into account the effects of tire centrifugal forces insofar as tire radial growth is concerned. However, it is also possible that the centrifugal forces may cause, in addition to the tire radial growth, a change in the tire stiffness which might, for example, be interpreted in terms of an additional pressure term proportional to the centrifugal force. In this case, equation (125) should be modified as follows:

$$F_z = \left[p_o + \kappa p_{o,a}(\delta/w)^2 + 0.08p_r + p_i\right] w\sqrt{wd}\, f_1\left(\frac{\delta + \Delta r}{w}\right) \qquad (126)$$

where p_i represents the additional inertia pressure.

Next, consider the relative importance of these two inertia effects insofar as they influence the variation of vertical force with apparent tire deflection. Apparently, the only available pertinent experimental data are contained in references 47 and 60. These references present variations of vertical force with rolling speed for a given vertical deflection for pure rolling conditions. Since these references do not tell what kind of vertical deflection is meant (apparent or effective deflection), an unambiguous interpretation of these data is not possible; however, it can be concluded from these data that the net effect of these two inertia effects for these data is of the same order of magnitude as would be expected from a consideration of the tire-growth effect alone. Also, depending on whether the data are assumed to involve apparent or effective deflection, it appears that either the tire-growth effect alone is important (the inertia-pressure effect being negligible) or that both effects are of the same order of magnitude.

Drag and side-load effects.- In order to take into account the effects of drag and side loads on the vertical-force-deflection variation, equation (126) must be modified as follows:

$$F_z = \left[p_o + \kappa p_{o,a}(\delta/w)^2 + 0.08p_r + p_i\right] w\sqrt{wd}\, f_1\left(\frac{\delta + \Delta r - \delta_x - \delta_\lambda}{w}\right) \qquad (127)$$

where the expressions δ_x and δ_λ represent the vertical sinking of the tire at a given vertical load due to drag and side loads, respectively (see eqs. (54) and (39)).

Hysteresis effects.- Equation (127) is the final equation for the vertical-force-deflection variation during a landing impact. This equation takes into account effects of centrifugal, drag, and side forces but does not provide for any hysteresis effects. Hysteresis effects are of some importance for static tests, drop tests without prerotation, and for the later stages of prerotation drop tests (after the wheels have stopped rotating); however, for conditions in which the tires are rotating with peripheral velocities which are large compared with their vertical velocity, the hysteresis effects on different parts of the tires tend to cancel out insofar as net vertical forces are concerned (see refs. 15 and 47). Since a high ratio of peripheral velocity to vertical velocity always exists during realistic landing impacts (except for a probably unimportant instant just after ground contact), hysteresis effects probably need not be taken into account in establishing the relationship between vertical force and deflection for a landing impact.

Illustrative data.- At present, insufficient information is available to permit a direct evaluation of the reliability of equation (127) for landing-impact conditions by comparisons of calculated and experimental force-deflection variations. However, some qualitative indication of the reliability of this equation may be obtained by examination of figure 58. This figure presents comparisons of experimental vertical-force-deflection curves for static (increasing-force) conditions and for landing-impact conditions at several horizontal velocities. It may first be noted from this figure that the experimental differences between the static and landing curves are small; however, the landing curves do appear to be very slightly lower for the early small-vertical-load (spin-up) stages of the landings (see parts of curves below horizontal bars) and appear to be higher for the later large-vertical-load (post-spin-up) stages of the landings (see parts of curves above horizontal bars). Such differences might also be expected from a comparison of the predictions of equations (127) and (122). The calculated force for the landing case (eq. (127)) would be initially smaller than that for the static case (eq. (122)) because of the drag-load effect (see δ_x factor in eq. (127)) and would be larger after spin-up than that for the static case because of the tire-radius-growth effect (see Δr factor in eq. (127)).

Force-Deflection Variation for Prerotation Drop Tests

The force-deflection variation for the early stages of prerotation drop tests, where the wheels are still rotating, is similar to the static force-deflection variation (see fig. 59), involves basically the same types of phenomena as are involved in landings with finite horizontal speed, and can probably be predicted with fair accuracy by equation (127). However, the radius change Δr is positive for landings (the tire grows after ground contact) but is negative for prerotation drop tests.

During later stages of prerotation drop tests the tire ceases rotation; this cessation of rotation permits hysteresis effects to exert a not easily predicted effect on the force-deflection variation, and, eventually, in the last stages of such tests, the force-deflection variation becomes similar to that for a drop test without prerotation (see ref. 53).

MISCELLANEOUS TIRE PROPERTIES

This section considers the following tire and wheel characteristics: centrifugal growth of the tire radius, wheel and tire inertia properties, and tire hysteresis properties.

CENTRIFUGAL GROWTH OF TIRE RADIUS

When a tire is rotated its radius increases, because of the centrifugal forces, by a small fraction which increases with increasing rotational speed. For small rotational speeds, Davison (as cited in ref. 18) has suggested that the fractional radius increase $\Delta r/r_o$ is linearly proportional to the ratio of the tire centrifugal forces to the tire spring forces. For a given tire shape, the tire centrifugal forces will be proportional to $m_t r_o \omega^2$ (where m_t is the tire mass and ω is the angular velocity in radian measure) and the spring forces will be proportional to $p r_o^2$ (where p is the inflation pressure). Consequently, Davison's suggestion implies that the radius growth obeys an equation of the type

$$\frac{\Delta r}{r_o} = d_1 \frac{m_t r_o \omega^2}{p r_o^2} \tag{128}$$

where d_1 is a constant depending on tire shape. According to some data, which are given in tables III and IV and discussed in appendix B, for two 26×6.6-12PR-VII and 56×16-32PR-VII tires, equation (128) is fairly realistic for radius changes of less than 1.5 percent for a wide range of inflation pressures, and the constant d_1 is approximately equal to 0.01; therefore, equation (128) can be written in the form

$$\Delta r = 0.01 \frac{m_t \omega^2}{p} \tag{129}$$

(See fig. 60.)

Some additional experimental data, obtained from reference 53, are shown in figure 61 for a pair of 57×20-16Ply-I(56-inch) tires. These data are also seen to be in fair agreement with the predictions of equation (129).

WHEEL AND TIRE INERTIA PROPERTIES

Table V of this paper presents a list of coefficients suitable for rough computations of the following inertia properties of a wheel and tire: mass of tire plus tube m_t; mass of tire, tube, and wheel m_w; polar moment of inertia of tire and tube about the wheel axle $I_{y,t}$; polar moment of inertia of tire, tube, and wheel about the wheel axle $I_{y,w}$; polar moment of inertia of tire, tube, and wheel about an axis perpendicular to the wheel axle $I_{x,w}$; and the three corresponding radii of gyration $k_t = \sqrt{I_{y,t}/m_t}$, $k_w = \sqrt{I_{y,w}/m_w}$, and $k_x = \sqrt{I_{x,w}/m_w}$. The values of the various coefficients listed in this table are average values established on the basis of data obtained from tire manufacturers, from tire specifications, from tire tests conducted at the Langley Laboratory, and from several published papers (refs. 3, 21 to 24, and 59). More specifically, the values of r_t/r listed in table V were obtained from reference 61, which indicates that these values are accurate within about 5 percent for new tires. The values of k_x/r and $I_{x,w}/r^5$ were estimated from data contained in reference 3 and from some unpublished data obtained at the Langley Laboratory, which are listed in table VI. The values of m_t/r^3 were obtained from tire manufacturers' data. The values of m_w/r^3 were established from data in references 3 and 21 to 24, and from the unpublished data listed in table VI. The values of k_w/r were estimated by making use of the corresponding values of k_t/r, m_t/r^3, and m_w/r^3 together with an empirical equation for the radius of gyration of the wheel assembly (exclusive of the tire and tube) which is given in reference 61. The values of $I_{y,t}/r^5$ and $I_{y,w}/r^5$ were obtained from the relationships $I_{y,t} = m_t k_t^2$ and $I_{w,t} = m_w k_w^2$.

For different main- and nose-wheel tires of the same type (I, III, and so forth), the actual inertia coefficients do not appear to vary much with tire size from the average values of table V; however, for tail-wheel tires, there may be considerable variation from these average values. Some indication of the variation of these coefficients is provided by table VI, which presents comparisons of experimental inertia coefficients with the corresponding average coefficients from table V for a number of tires. (All the data given in table VI for types I, III, and VII tires are for main- or nose-wheel tires.)

TIRE HYSTERESIS PROPERTIES

This section presents a discussion and analysis of the hysteresis properties of a standing tire under the influence of lateral, vertical, fore-and-aft, and torsional cyclic forces or moments. (Some discussion of the importance and application of these hysteresis properties for the case of a rolling tire is given in ref. 54.)

Preliminary Discussion

As a preliminary step for defining tire hysteresis constants, it is convenient to consider briefly the general behavior of a standing tire as influenced by hysteresis effects for the special case where the base of an untilted tire is subjected to a periodic lateral deformation λ_o of the form

$$\lambda_o = \lambda_{o,max} \sin \nu t \tag{130}$$

by an applied lateral ground force $F_{y,\lambda}$. (See fig. 17.) Under these conditions, the lateral ground force is observed experimentally to vary with time in the manner indicated in sketch 1, and the corresponding

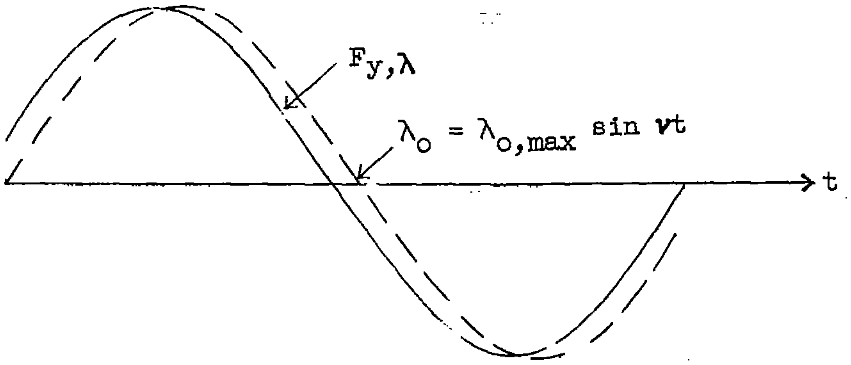

Sketch 1

variation of lateral ground force with lateral tire deformation, shown in sketch 1, appears in the form of a typical hysteresis loop (see sketch 2). This hysteresis loop arises largely as a consequence of the structural or hysteresis damping forces which oppose the tire deformation. In the case of metallic structures, such hysteresis forces appear to be independent of frequency, have an amplitude usually equal to a small fraction of the amplitude of the corresponding spring force, but shifted in phase by 90°, and can be analytically represented with fair accuracy as the damping force generated by an equivalent viscous damper whose damping coefficient is inversely proportional to the frequency of oscillation. (See, for example, ref. 64 or any other book on aeroelasticity.) The assumption is made henceforth that these same concepts are applicable to the treatment of hysteresis effects in standing tires.

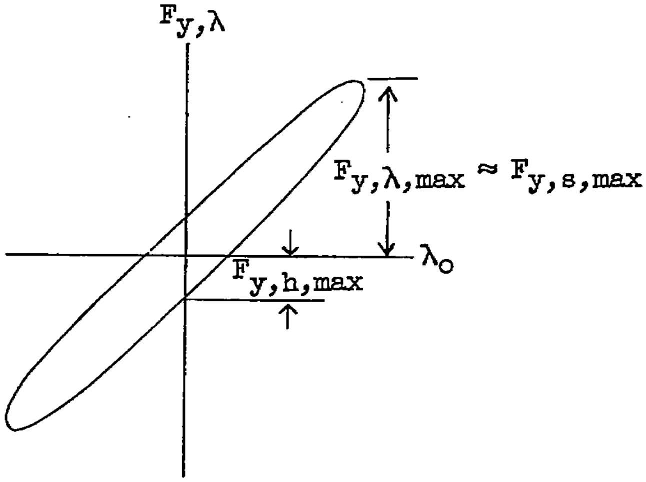

Sketch 2

The lateral spring force $F_{y,s}$ in a tire for purely lateral oscillations is

$$F_{y,s} = K_\lambda \lambda_o \tag{131}$$

where K_λ is the lateral spring constant. The corresponding hysteresis damping force, in accordance with the preceding assumptions, can be described by the equation

$$F_{y,h} = \frac{\eta_\lambda K_\lambda}{\nu} D_t \lambda_o \tag{132}$$

where the parameter η_λ is the ratio of the maximum hysteresis force $F_{y,h,max}$ to the maximum spring force $F_{y,s,max}$, or since the maximum total ground force $F_{y,\lambda,max}$ and the maximum spring force are approximately equal,

$$\eta_\lambda = \frac{F_{y,h,max}}{F_{y,\lambda,max}} \tag{133}$$

(See sketch 2.)

Equations (131) to (133) provide a simplified set of equations for the lateral hysteresis and spring force acting on a standing tire subjected to a cyclic lateral force. The corresponding equations for other types of loadings are analogous to these equations.

Evaluation of Lateral Hysteresis Parameter η_λ

Free-vibration tests.- Experimental evaluation of the lateral hysteresis parameter η_λ from the experimental dynamic free-vibration tests of reference 25 (at frequencies usually up to about 4 cps) gives variations of η_λ with tire inflation pressure of the type illustrated in figure 62 for two pairs of type VII tires. (The method of evaluating η_λ from the free-vibration test data is discussed in appendix C.) Figure 62 shows that the parameter η_λ appears to decrease with increasing inflation pressure and to obey roughly an equation of the type

$$\eta_\lambda = \frac{2\eta_{\lambda,r}}{1 + (p/p_r)} \tag{134}$$

where $\eta_{\lambda,r}$ (the value of η_λ at rated pressure) was found to be equal to 0.092 and 0.096 for the two pairs of type VII tires shown in the figure and was found to be equal to 0.092 and 0.120 for two pairs of type II tires.

Static tests.- Experimental evaluation of η_λ from the static tire-test data of references 21, 23, and 24 gives results of the type illustrated in figure 63. The data in this figure, in contrast with the vibration-test data (fig. 62), indicate no definite trends with inflation pressure. The wide scatter of the data may be due to several of the following causes: (1) For some of the data shown, only incomplete (half-cycle) hysteresis loops were available; consequently, accurate determination of η_λ from these data was sometimes difficult; (2) skidding of the tires may cause a falsified oversized hysteresis loop; and (3) the parameter η_λ may also depend on the amplitude of the lateral deformation and on the tire vertical deflection, neither of which variables is taken into account in figure 63.

Mean value of η_λ.- On the basis of an inspection of the preceding dynamic and static information on the lateral hysteresis parameter η_λ, this parameter appears to be roughly equal to

$$\eta_\lambda = 0.1 \tag{135}$$

for both static and dynamic conditions near rated pressure. While this parameter also varies with inflation pressure and perhaps with other variables, the available data do not appear to be sufficient to justify an expression any more refined than that of equation (135).

Evaluation of Vertical Hysteresis Parameter η_z

The vertical hysteresis parameter η_z, which is a measure of the hysteresis force experienced during small vertical periodical motions of a tire from a reference position (where $F_{z,o}$ is the average or reference vertical force), is hereby defined by the equation

$$\eta_z = \frac{F_{z,h,max}}{F_{z,max} - F_{z,o}} \tag{136}$$

(analogous to eq. (133) for η_λ) where F_z is the vertical force and $F_{z,h,max}$ is the half-height of the corresponding force-deflection hysteresis loop.

The only available experimental data pertinent to this parameter are the free-vibration data of reference 25, some of which are shown in figure 64 for two pairs of type VII tires. These data indicate that the parameter η_z varies with inflation pressure in the same manner as the parameter η_λ according to an equation like equation (134) or

$$\eta_z = \frac{2\eta_{z,r}}{1 + \left(p/p_r\right)} \tag{137}$$

where $\eta_{z,r}$ (the value of η_z at rated pressure) was found to be equal to 0.074 and 0.090 for the two pairs of type VII tires shown in figure 64 and 0.100 and 0.120 for two pairs of type II tires. In view of these data, apparently the value of η_z is approximately

$$\eta_z = 0.1 \tag{138}$$

near rated pressure conditions.

Evaluation of Fore-and-Aft Hysteresis Parameter η_x

The fore-and-aft hysteresis parameter η_x, which is a measure of the hysteresis force experienced in fore-and-aft tire vibrations, is defined by the equation

$$\eta_x = \frac{F_{x,h,max}}{F_{x,max}} \tag{139}$$

(analogous to eq. (133) for η_λ) where F_x is the fore-and-aft force and $F_{x,h,max}$ is the half-height of the corresponding force-deflection hysteresis loop. Most of the available experimental data pertinent to this parameter are the free-vibration data of reference 25. The variation of η_x with inflation pressure obtained from these data (in the manner described in appendix C) is shown in figure 65. From these data it appears that, approximately,

$$\eta_x = 0.12 \tag{140}$$

The only other available data from which η_x could be evaluated were data for a single half-cycle static hysteresis loop for a 56×16-32PR-VII tire (ref. 21). These data indicate a similar slightly larger value of η_x (≈ 0.16).

Evaluation of Torsional Hysteresis Parameter η_α

The torsional hysteresis parameter η_α, which is a measure of the hysteresis moment experienced by a tire during torsional vibrations, is hereby defined by the equation

$$\eta_\alpha = \frac{M_{z,h,max}}{M_{z,max}} \tag{141}$$

(analogous to eq. (133) for η_λ) where M_z is the twisting moment and $M_{z,h,max}$ is the half-height of the corresponding moment—twist-angle hysteresis loop.

Little directly pertinent information is available in regard to the magnitude of η_α. However, since all the similarly defined hysteresis parameters η_λ, η_z, and η_x were found to be approximately equal to 0.1, it seems reasonable to infer also that

$$\eta_\alpha = 0.1 \tag{142}$$

As an additional rough check on the reliability of equation (142), two static hysteresis loops were available for a 45×15-14PR-III(15.50-20) tire at its rated loading condition. These loops were taken at small twist angles to minimize tire skidding (which, according to the data of ref. 25, is usually important for twist angles greater than 1°); moreover, for this same purpose, the ground-contact surface of the tire was glued to the ground surface (in this case a steel plate). These tests gave a value of $\eta_\alpha \approx 0.14$ for a maximum twist angle of 1.5° and $\eta_\alpha \approx 0.24$ for an angle of 4° and indicate that equation (142) may be reasonable for small twist angles.

CONCLUDING REMARKS

In this paper a fairly comprehensive analysis has been made of the available experimental data on most of the mechanical properties of pneumatic tires which are of interest to aircraft designers, and some empirical equations have been established for most of these properties. These empirical equations probably furnish as accurate an overall estimate of the tire properties considered as can be obtained from the data presently available without going into a detailed analysis of the internal construction of tires. However, many of the experimental data on which these equations were based were obtained under static or slow-speed rolling conditions. Although the extremely limited available evidence for high-speed rolling conditions has not yet revealed any drastic effects of speed on most tire properties, a need still exists, of course, for further studies of the behavior of tires for the complete practical range of high-speed rolling conditions.

Langley Aeronautical Laboratory,
National Advisory Committee for Aeronautics,
Langley Field, Va., July 26, 1957.

APPENDIX A

SAMPLE OF METHOD OF DETERMINATION OF EMPIRICAL EQUATIONS

This appendix discusses the manner in which the form of the empirical equation (33) for lateral spring constant was established from the available experimental data. The forms of most of the other empirical equations in this paper were determined in a similar manner.

Plots were made of lateral spring constant K_λ against the ratio of inflation pressure p to rated pressure p_r for various vertical deflections and for different tires. These plots showed that most data could be described by the linear relation

$$K_\lambda = A\left(\frac{p}{p_r} + 0.24\right)$$

or, equivalently, by the relation

$$\frac{K_\lambda}{p + 0.24p_r} = B \tag{A1}$$

where A and B represent functions which depend on tire size, shape, and vertical deflection. Next, plots were made of the two simplest dimensionless stiffness parameters which could be formed in accordance with equation (A1) $\left(\text{namely, } \frac{K_\lambda}{d(p + 0.24p_r)} \text{ and } \frac{K_\lambda}{w(p + 0.24p_r)}\right)$ against the two simplest vertical-deflection parameters $\left(\text{namely, } \frac{\delta_o}{d} \text{ and } \frac{\delta_o}{w}\right)$. (In the corresponding analysis of a few other tire properties, it was occasionally possible to make use of theoretical considerations in selecting the best choice of parameters to condense the data; however, usually it was necessary to use a trial-and-error procedure.) These plots indicated that these spring-constant parameters decreased approximately linearly with increasing vertical deflection and that the best condensation of the data for a given tire type was obtained by plotting the stiffness parameter $\frac{K_\lambda}{w(p + 0.24p_r)}$ against the vertical-deflection parameter $\frac{\delta_o}{w}$ (see fig. (20)), and which plots were found to be fairly well fitted by the empirical equation (33), which is discussed in the text.

APPENDIX B

MEASUREMENTS OF TIRE GROWTH DUE TO CENTRIFUGAL FORCES

In order to obtain some quantitative measure of the growth of tires at high wheel angular velocities, tests were performed with two type VII tires, one a 56×16-32PR tire (see ref. 21 for properties of a tire of the same size and type) and the other a 26×6.6-12PR tire whose properties are described in reference 23 (see data for tire A at end of testing in ref. 23).

For these tests the tires were mounted in a heavy fixture. An air jet attached to the test fixture and trained on the tires permitted angular velocities from approximately 0 to 2,000 rpm for the 26×6.6 tire and from 0 to 900 rpm for the 56×16 tire, which corresponded to rolling speeds from about 0 to 220 feet per second for both tires.

Angular velocities of the tires were measured with a strobotachometer. The tire radial growth was obtained by reading a radially oriented ruler, placed behind the tires, through a transit or theodolite placed about 30 feet in front of the tires.

Experimental tire growth measurements were obtained for three inflation pressures for each tire and are listed in tables III and IV. These data are also plotted in figure 60 in dimensionless form.

APPENDIX C

DETERMINATION OF HYSTERESIS CONSTANTS FROM FREE-VIBRATION TESTS

This appendix discusses a procedure for determining the lateral hysteresis coefficient η_λ (see eq. (133)) from information gained by free-vibration tests of a two-wheel cart of the type described in reference 25. Such a cart can be approximately represented by the linear mass-spring-damper system in the following sketch:

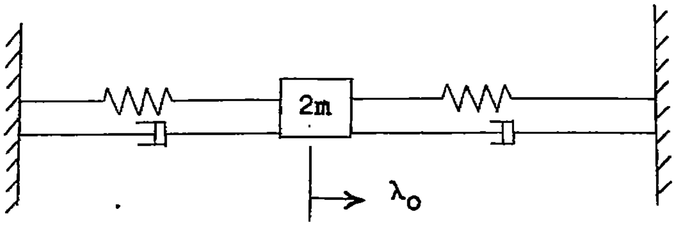

where the springs represent the two tire stiffnesses, the dampers represent the hysteresis damping, and 2m represents the mass of the cart. The spring and damping forces are given by equations (131) and (132), respectively, and the corresponding differential equation for the system for free oscillations is

$$2mD_t^2\lambda_o + 2\frac{\eta_\lambda K_\lambda}{\nu}D_t\lambda_o + 2K_\lambda\lambda_o = 0 \tag{C1}$$

The solution of this equation is of the form

$$\lambda_o = \varphi_1 e^{-\frac{\eta_\lambda K_\lambda}{2\nu m}t}\sin\left(\nu t + \varphi_2\right) \tag{C2}$$

where φ_1 and φ_2 are constants and

$$\nu = \sqrt{\frac{K_\lambda}{m} - \left(\frac{\eta_\lambda K_\lambda}{2\nu m}\right)^2} = \sqrt{\frac{K_\lambda}{m}\left(1 - \frac{\eta_\lambda^2 K_\lambda}{4m\nu^2}\right)} \tag{C3}$$

Inasmuch as $\frac{\eta_\lambda{}^2 K_\lambda}{4m\nu^2} \ll 1$ for conventional tires, equation (C3) can almost always be replaced by the simpler expression

$$\nu = \sqrt{\frac{K_\lambda}{m}} \tag{C4}$$

and, thus, equation (C2) can be reduced to the form

$$\lambda_o = \varphi_1 e^{-\frac{1}{2}\eta_\lambda \nu t} \sin\left(\nu t + \varphi_2\right) \tag{C5}$$

The decrease in amplitude of the lateral oscillation per cycle $\left(\text{of period } T = \frac{1}{f} = \frac{2\pi}{\nu}\right)$ is then

$$\frac{\lambda_o(t + T)}{\lambda_o(t)} = e^{-\frac{1}{2}\eta_\lambda \nu T} = e^{-\pi\eta_\lambda} \tag{C6}$$

Since this ratio can be directly measured in free-vibration tests, equation (C6) provides the necessary relation for determining the parameter η_λ from such test data. In addition, equation (C4) gives the necessary equation for determining the lateral spring constant K_λ in terms of the experimental frequency and the cart mass $2m$.

REFERENCES

1. Becker, Gabriel, Fromm, Hans, and Maruhn, Herbert: Schwingungen in Automobillenkungen ("Shimmy"). M. Krayn (Berlin), 1931.

2. Bird, G., and Miller, R. A.: Studies in Road Friction - II. An Analysis of the Factors Affecting Measurement. Road Res. Tech. Paper No. 2, British Dept. Sci. and Ind. Res. and Ministry of Transport, 1937.

3. Boeckh: Ermittlung der elastischen Konstanten von Flugzeugreifen. (Determination of the Elastic Constants of Airplane Tires.) Focke-Wulf Flugzeugbau G.m.b.H. (Bremen), Dec. 1944. (Available in English translation as NACA TM 1378, 1954.)

4. Bourcier de Carbon, Christian: Étude Théorique du Shimmy des Roues d'Avion. (Analytical Study of Shimmy of Airplane Wheels.) Office National d'Études et de Recherches Aéronautiques, Publication No. 7, 1948. (Available in English translation as NACA TM 1337, 1952.)

5. Bull, A. W.: Tire Behavior in Steering. SAE Jour., vol. 45, no. 2, Aug. 1939, pp. 344-350.

6. Chudakov, Y. A.: Tilted Rolling of an Automobile Wheel. Rep. Acad. Sci. (USSR), vol. 90, no. 3, May 21, 1953, pp. 343-346.

7. Chudakov, Y. A.: On the Tilted Rolling of an Automobile Wheel. Rep. Acad. Sci. (USSR), vol. XCII, no. 1, Sept. 1, 1953, pp. 13-15.

8. Dietz, O., and Harling, R.: Seitensteifigkeit und Seitenführung von Flugzeugreifen. FB Nr. 1498, ZWB, Oct. 1941. (Available in English translation from ASTIA as ATI 18905.)

9. Drake, D. W.: Torsional and Side Load Spring Constants for P2V-4 Nose Wheel Tire. Rep. No. 6984, Lockheed Aircraft Corp., Burbank, May 6, 1949.

10. Evans, R. D.: Cornering Power of Airplane Tires. The Goodyear Tire & Rubber Co., Oct. 17, 1946.

11. Evans, R. D.: Properties of Tires Affecting Riding, Steering and Handling. SAE Jour., vol. 36, no. 2, Feb. 1935, pp. 41-49.

12. Fiala, E.: Seitenkräfte am rollenden Luftreifen. Zeitschr. V.D.I., Bd. 96, Nr. 29, Oct. 11, 1954, pp. 973-979.

13. Förster, B.: Versuche zur Feststellung des Haftvermögens von Personenwagen-Bereifungen. (Tests To Determine the Adhesive Power of Passenger-Car Tires.) Deutsche Kraftfahrtforschung Zb. No. 22 (Berlin), (Undated). (Available in English translation as NACA TM 1416, 1956.)

14. Fromm, H.: Seitenschlupf und Führungswert des rollenden Rades. (Sideslip and Guiding Characteristics of the Rolling Wheel.) Bericht 140 der L.G.L., 1941, pp. 56-63. (Available in English translation as NACA TM 1365, pp. 191-216.)

15. Fromm, H.: Schwingungsdämpfung am rollenden Rade. (Oscillation Damping on the Rolling Wheel.) Bericht 140 der L.G.L., 1941, pp. 66-67. (Available in English translation as NACA TM 1365, pp. 229-233.)

16. Fromm, H.: Untersuchungen über Seitenkräfte und Wendemomente am Fahrwerk und ihre Bedeutung für die Verbesserung der Lastannahmen. Bericht 169 der L.G.L., 1943, pp. 9-18.

17. Hadekel, R.: Some Notes on Pneumatic Tyres. Aircraft Engineering, vol. XVI, no. 179, Jan. 1944, pp. 11-13, 17.

18. Hadekel, R.: The Mechanical Characteristics of Pneumatic Tyres. S & T Memo. No. 5/50, British Ministry of Supply, TPA 3/TIB, Mar. 1950.

19. Harling, R.: Seitenführungskräfte bei Schräglauf von Flugzeugreifen. (Lateral Guiding Forces on Obliquely Running Airplane Tires.) Bericht 140 der L.G.L., 1941, pp. 4-7. (Available in English translation as NACA TM 1365, pp. 7-15.)

20. Hample, W. G.: Friction Study of Aircraft Tire Material on Concrete. NACA TN 3294, 1955.

21. Horne, Walter B.: Static Force-Deflection Characteristics of Six Aircraft Tires Under Combined Loading. NACA TN 2926, 1953.

22. Horne, Walter B., Stephenson, Bertrand H., and Smiley, Robert F.: Low-Speed Yawed-Rolling and Some Other Elastic Characteristics of Two 56-Inch-Diameter, 24-Ply-Rating Aircraft Tires. NACA TN 3235, 1954.

23. Horne, Walter B., Smiley, Robert F., and Stephenson, Bertrand H.: Low-Speed Yawed-Rolling Characteristics and Other Elastic Properties of a Pair of 26-Inch-Diameter, 12-Ply-Rating, Type VII Aircraft Tires. NACA TN 3604, 1956.

24. Horne, Walter B., and Smiley, Robert F.: Low-Speed Yawed-Rolling Characteristics and Other Elastic Properties of a Pair of 40-Inch-Diameter, 14-Ply-Rating, Type VII Aircraft Tires. NACA TN 4109, 1957.

25. Horvay, G., and Crowe, R. E.: Spring and Damping Constants of Helicopter Tires. Eng. Rep. No. H-122-1 (Contract NO a(S)-3703), Helicopter Res. Div., McDonnell Aircraft Corp., July 17, 1945.

26. Howard, Walter B., Jr.: A Full-Scale Investigation of the Effect of Several Factors on the Shimmy of Castering Wheels. NACA TN 760, 1940.

27. Huber, L.: Die Fahrtrichtungsstabilität des schnellfahrenden Kraftwagens. Deutsche Kraftfahrtforschung, No. 44, 1940, pp. 18-64.

28. Joy, T. J. P., and Hartley, D. C.: Tyre Characteristics As Applicable to Vehicle Stability Problems. Proc. Automobile Div., Inst. Mech. Eng. (London), No. 6, 1953-4, pp. 113-133.

29. Joy, T. J. P., Hartley, D. C., and Turner, D. M.: Tyres for High Performance Cars. Preprint No. 549, SAE Golden Anniversary Summer Meeting, June 12-17, 1955.

30. Kantrowitz, Arthur: Stability of Castering Wheels for Aircraft Landing Gears. NACA Rep. 686, 1940.

31. Klaue, H.: Bremswerkuntersuchungen am Kraftfahrzeug. Deutsche Kraftfahrtforschung im Auftrag des Reichs-Verkehrsministeriums. Heft 13, VDI - Verlag G.m.b.H. (Berlin), 1938.

32. Knoroz, V. E.: Use of Motion Pictures for Tire Contact Studies. Bull. Acad. Sci. (USSR), no. 10, 1954, pp. 93-98.

33. Kraft, P.: Die Kräfteverteilung in der Berührungsfläche zwischen Reifen und Fahrbahn. (Force Distribution in the Contact Surface Between Tire and Runway.) Bericht 140 der L.G.L., 1941, pp. 11-14. (Available in English translation as NACA TM 1365, pp. 31-40.)

34. Luthman, Robert R.: Coefficient of Friction of Aircraft Tires on Concrete Runways. WADC Tech. Rep. 55-179, Wright Air Dev. Center, U. S. Air Force, Mar. 1955.

35. Maier, E.: Zur Frage der Seitenbeanspruchungen von Flugzeugfahrwerken. Bericht 169 der L.G.L., 1943, pp. 19-27.

36. Maier, E.: Probleme am schwenkbaren Flugzeugrad. (Problems of the Swivellable Airplane Wheel.) Tech. Berichte der Z.W.B., Bd. 10, Heft 8, Aug. 15, 1943, pp. 229-238. (Also available in English translation from ASTIA as ATI No. 36989.)

37. Melzer, M.: Beitrag zur Theorie des Spornradflatterns. (Contribution to the Theory of Tail-Wheel Shimmy.) Tech. Berichte, Bd. 7, Heft 2, ZWB, 1940, pp. 59-70. (Available in English translation as NACA TM 1380, 1954.)

38. Michael, Franz: Zur Frage der Abmessungen von Luftreifen für Flugzeuglaufräder. (The Problem of Tire Sizes for Airplane Wheels.) Z.F.M., Bd. 23, Nr. 13, July 14, 1932. (Available in English translation as NACA TM 689, 1932.)

39. Milwitzky, Benjamin, and Cook, Francis E.: Analysis of Landing-Gear Behavior. NACA Rep. 1154, 1953. (Supersedes NACA TN 2755, 1952.)

40. Milwitzky, Benjamin, Lindquist, Dean C., and Potter, Dexter M.: An Experimental Study of Applied Ground Loads in Landing. NACA Rep. 1248, 1956. (Supersedes NACA TN 3246, 1954.)

41. Moyer, R. A.: Skidding Characteristics of Automobile Tires on Roadway Surfaces and Their Relation to Highway Safety. Bull. 120, Iowa Engr. Exp. Station, Iowa State Col., vol. XXXIII, no. 10, Aug. 8, 1934.

42. Pike, E. C.: Coefficients of Friction. Jour. R.A.S., vol. 53, Dec. 1949, pp. 1085-1094.

43. Robson, J. J.: High Speed Cornering Forces. Preprint No. 550, SAE Golden Anniversary Summer Meeting, June 12-17, 1955.

44. Rotta, J.: Zur Statik des Luftreifens. Ing.-Archiv, Bd. XVII, Heft 1 and 2, 1949, pp. 129-141.

45. Rotta, J.: Properties of the Aeroplane During Take-Off and Alighting. Reps. and Translations No. 969, Dec. 15, 1947, British M.A.P. Völkenrode.

46. Sawyer, Richard H., Hall, Albert W., and McKay, James M.: Vertical and Drag Ground-Reaction Forces Developed in Landing Impacts of a Large Airplane. NACA RM L55E12c, 1955.

47. Schippel, H. F.: Airplane Tires and Wheels. Aero. Eng., Trans. A.S.M.E., vol. 3, no. 1, Jan.-Mar., 1931, pp. 45-52.

48. Von Schlippe, B., and Dietrich, R.: Zur Mechanik des Luftreifens. (The Mechanics of Pneumatic Tires.) Junkers Flugzeug- und Motorenwerke, A.-G. (Dessau). (Translation available from ASTIA as ATI 105296.)

49. Schrode, H.: Steifigkeiten verschiedenartiger Reifen. (Stiffnesses of Various Tires.) Bericht 140 der L.G.L., 1941, pp. 8-10. (Available in English translation as NACA TM 1365, pp. 17-29.)

50. Schrode: Beitrag zur Frage des Reifenaufbaus und der Belastungsfähigkeit von Flugzeugreifen. (Construction and Load Capacity of Aircraft Tires.) FB Nr. 1205, Deutsche Luftfahrtforschung (Berlin-Adlershof), 1940. (Available in English translation from ASTIA as ATI No. 27064.)

51. Schuster, Robert, and Weichsler, Paul: Der Kraftschluss zwischen Rad und Fahrbahn. Automobiltechnische Zeitschrift, Jahrgang 38, Heft 20, Oct. 25, 1935, pp. 499-504.

52. Smiley, Robert F.: Correlation, Evaluation, and Extension of Linearized Theories for Tire Motion and Wheel Shimmy. NACA TN 3632, 1956.

53. Smiley, Robert F., and Horne, Walter B.: Vertical Force-Deflection Characteristics of a Pair of 56-Inch-Diameter Aircraft Tires From Static and Drop Tests With and Without Prerotation. NACA TN 3909, 1956.

54. Smiley, Robert F.: On Tire Hysteresis Effects in Tire Motion and Wheel Shimmy. NACA TN 4001, 1957.

55. Temple, G.: Note on American Work on Kinematic and Dynamic Shimmy. Rep. No. A.D. 3158, British R.A.E., Nov. 1940.

56. Theisen, Jerome G., and Edge, Philip M., Jr.: An Evaluation of an Accelerometer Method for Obtaining Landing-Gear Drag Loads. NACA TN 3247, 1954.

57. Thorson, K. R.: A Rational Method for Predicting Tire Cornering Forces and Lateral Stiffness. Boeing Doc. No. D-11719, Boeing Airplane Co., Mar. 28, 1951.

58. Winter, H., and Kranz, M.: Ermittlung der Federkennbilder von Flugzeugreifen deutscher Normgrösse. (The Elasticity Characteristics of Standard German Aircraft Tires.) FB Nr. 388, Deutsche Versuchsanstalt für Luftfahrt, E.V. (Berlin-Adlershof). (Available in English translation from ASTIA as ATI 23005.)

59. Zahrt, K. W.: Aircraft Wheel Inertia Drag Loads. Eng. Div. Memo. Rep. No. TSELA-2B-4263-46-4, ATSC, Army Air Forces, Sept. 30, 1944.

60. Zahrt, K. W.: Aircraft Wheel Inertia Drag Loads. Tire Load-Deflection Characteristics. Engr. Div. Memo. Rep. TSEAL24263-46-4, ADD. 2, ATSC, Army Air Forces, 1945. (Also available from ASTIA as ATI No. 169885.)

61. Anon.: Year Book, the Tire and Rim Assoc., Inc., 1955.

62. Anon.: Military Specification - Casings; Aircraft Pneumatic Tire. Military Specification, MIL-C-5041, Sept. 16, 1949; Amendment-2, Feb. 8, 1951.

63. Anon.: Army-Navy Aeronautical Specification Casings; Aircraft Landing, Nose, Tail, and Beaching Tire. Army-Navy Aeronautical Specification, AN-C-55e, Dec. 20, 1946; Amendment-1, June 16, 1947.

64. Scanlan, Robert H., and Rosenbaum, Robert: Introduction to the Study of Aircraft Vibration and Flutter. The Macmillan Co., 1951.

TABLE I.- RATIO a OF NET FOOTPRINT AREA TO GROSS FOOTPRINT AREA FOR SEVERAL TIRES

Tire	Tread pattern	a
26×6.6-12PR-VII-R23-A	Rib	0.75
26×6.6-12PR-VII-R23-B	Rib	.76
40×12-14PR-VII-R24-A	Rib	.76
40×12-14PR-VII-R24-B	Rib	.76
56×16-24PR-VII-R22-A	Rib	.70
56×16-24PR-VII-R22-B	Rib	.65
57×20-16 Ply-I(56-inch)R53	Diamond (nonskid)	.60

TABLE II.- COMPARISON OF EXPERIMENTAL AND CALCULATED VALUES OF CORNERING POWER

$\frac{\delta}{d}$	$\frac{p}{p_r}$	Cornering power N, lb/deg		Tire
		Experimental	Calculated from equation (83)	
0.031	0.95	1,890	2,060	56x16-24PR-VII-R22
.032	.94	2,170	2,150	
.050	1.30	2,980	3,320	
.052	.98	2,590	2,810	
0.061	1.41	1,140	1,150	40x12-14PR-VII-R24
.066	1.22	970	980	
.076	1.02	860	870	
.089	.82	680	740	
.102	1.50	850	1,260	
.115	1.31	715	950	
.132	1.11	515	780	

TABLE III.- CENTRIFUGAL GROWTH OF A 26x6.6-12PR-VII TIRE

[Weight of tire plus tube, 26.9 lb]

p_o, lb/sq in.	r_o, in.	ω, rpm	Δr, in.
46	12.5	0	0
46	12.5	500	.04
46	12.5	700	.09
46	12.5	1,050	.16
46	12.5	1,345	.23
46	12.5	1,710	.32
46	12.5	1,980	.40
46	12.5	1,580	.30
46	12.5	1,260	.22
46	12.5	840	.12
80	12.5	0	0
80	12.5	610	.03
80	12.5	790	.06
80	12.5	900	.07
80	12.5	1,000	.08
80	12.5	1,070	.10
80	12.5	1,140	.11
80	12.5	1,235	.12
80	12.5	1,352	.14
80	12.5	1,590	.20
80	12.5	1,740	.23
80	12.5	1,990	.29
80	12.5	1,590	.20
80	12.5	1,310	.15
80	12.5	1,225	.14
80	12.5	1,120	.11
80	12.5	1,080	.10
80	12.5	850	.08
157	12.6	0	0
157	12.6	625	.01
157	12.6	810	.03
157	12.6	970	.04
157	12.6	1,175	.06
157	12.6	1,285	.07
157	12.6	1,540	.11
157	12.6	1,945	.17
157	12.6	1,515	.11
157	12.6	1,243	.07

TABLE IV.- CENTRIFUGAL GROWTH OF A 56×16-32PR-VII TIRE

[Weight of tire plus tube, 308 lb]

p_o, lb/sq in.	r_o, in.	ω, rpm	Δr, in.
66	27.5	0	0
66	27.5	280	.06
66	27.5	375	.15
66	27.5	480	.24
80	27.7	0	0
80	27.7	260	.04
80	27.7	440	.15
80	27.7	580	.28
80	27.7	680	.40
80	27.7	750	.50
80	27.7	840	.61
80	27.7	780	.54
80	27.7	670	.43
80	27.7	550	.30
80	27.7	440	.18
158	27.8	0	0
158	27.8	365	.08
158	27.8	420	.11
158	27.8	510	.17
158	27.8	640	.25
158	27.8	900	.47
158	27.8	760	.36
158	27.8	680	.30
158	27.8	590	.23
158	27.8	470	.14

TABLE V.- AVERAGE VALUES OF INERTIA COEFFICIENTS

Type	Description	$\frac{r_w}{r}$	$\frac{r_t}{r}$	$\frac{r_x}{r}$	$\frac{m_w}{r^3}$, slugs	$\frac{m_t}{r^3}$, slugs	$\frac{I_{y,w}}{r^5}$, slugs	$\frac{I_{y,t}}{r^5}$, slugs	$\frac{I_{x,w}}{r^5}$, slugs
I	Main and nose wheels Tail wheels	0.65 .65	0.80 .74	0.50 .50	1.10 ----	0.6 1.2	0.46 ----	0.38 ----	0.28 ----
II	Main and nose wheels	0.65	0.80	0.50	----	0.6	----	----	----
III	Main and nose wheels (to 11:00-12) Main and nose wheels (11:00-12 and up) Tail wheels	0.65 .65 .65	0.79 .77 .79	0.50 .50 .50	1.20 1.20 ----	0.7 .7 1.1	0.51 .51 ----	0.44 .42 ----	0.30 .30 ----
VI	Nose wheels	0.65	0.76	0.50	----	0.8	----	----	----
VII	Main and nose wheels Tail wheels	0.65 .65	0.79 .77	0.50 .50	1.25 ----	0.7 1.7	0.53 ----	0.44 ----	0.31 ----
Others		0.65	0.78	0.50	1.20	0.7	0.51	0.43	0.30

TABLE VI.- COMPARISON OF ACTUAL VALUES OF INERTIA COEFFICIENTS WITH AVERAGE VALUES

Type	Description	$\frac{r_w}{r}$	$\frac{r_t}{r}$	$\frac{r_x}{r}$	$\frac{m_w}{r^3}$, slugs	$\frac{m_t}{r^3}$, slugs	$\frac{I_{y,w}}{r^5}$, slugs	$\frac{I_{y,t}}{r^5}$, slugs	$\frac{I_{x,w}}{r^5}$, slugs	Source	
I	28×9-10PR (27-inch)				1.09	0.64				Reference 21	Experimental data
	28×9-10PR	0.65			1.18		0.50			Unpublished	
	28×9						.51			Unpublished	
	28×9						.56			Unpublished	
	36×13-12PR(36-inch)	.69		0.46	.91		.44		0.19	Unpublished	
	44×15-10PR(44-inch)				.79	.57				Reference 21	
	56×20 (56-inch)	.60		.49	1.36		.49		.32	Unpublished	
	56×20						.46			Reference 59	
	57×20-16Ply						.46			Unpublished	
	110× – (110-inch)						.41			Reference 59	
	Average value	.65		.50	1.10	.60	.46		.28	Table IV	
III	45×15-14PR(15.50-20)				1.15	0.76				Reference 21 - Experimental data	
	Average value				1.20	.70				Table IV	
VII	26×6.6-12PR-A	0.65	0.79		1.34	0.72	0.55	0.43		Reference 23	Experimental data
	26×6.6-12PR-B	.64	.77		1.37	.72	.56	.43		Reference 23	
	40×12-14PR-A				1.25	.71				Reference 24	
	40×12-14PR-B				1.24	.69				Reference 24	
	56×16-24PR-A				1.20	.67				Reference 22	
	56×16-24PR-B				1.18	.66				Reference 22	
	56×16-32PR				1.28	.75				Reference 21	
	Average value	.65	.79		1.25	.70	.53	.44		Table IV	
Others	22×8			0.51	1.34				0.35	Reference 3 - Experimental data	
	25×9			.52	1.58				.44		
	27×10			.50	1.21				.31		
	28×7			.47	1.15				.25		
	Average value			.50	1.20				.30	Table IV	

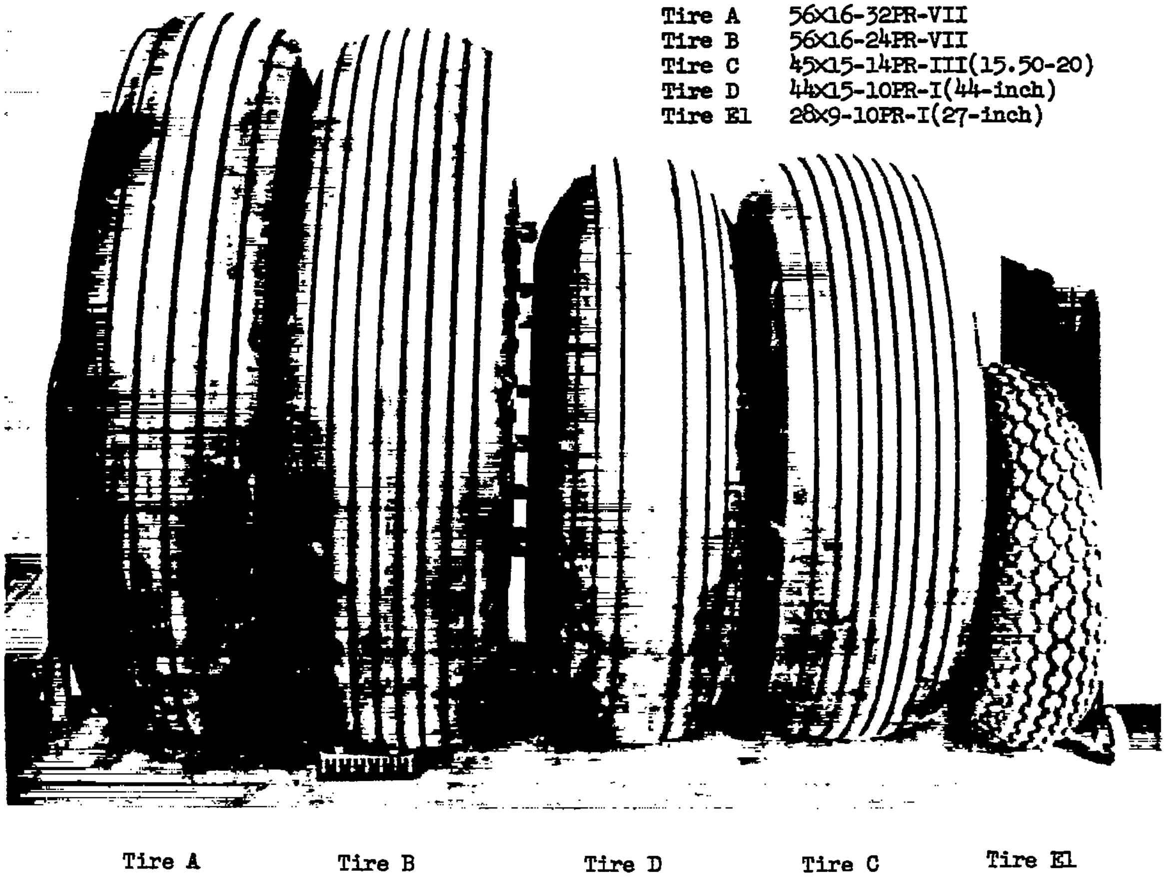

(a) Photograph of tires. L-74867.1

Figure 1.- Profiles of several types I, III, and VII American tires from reference 21.

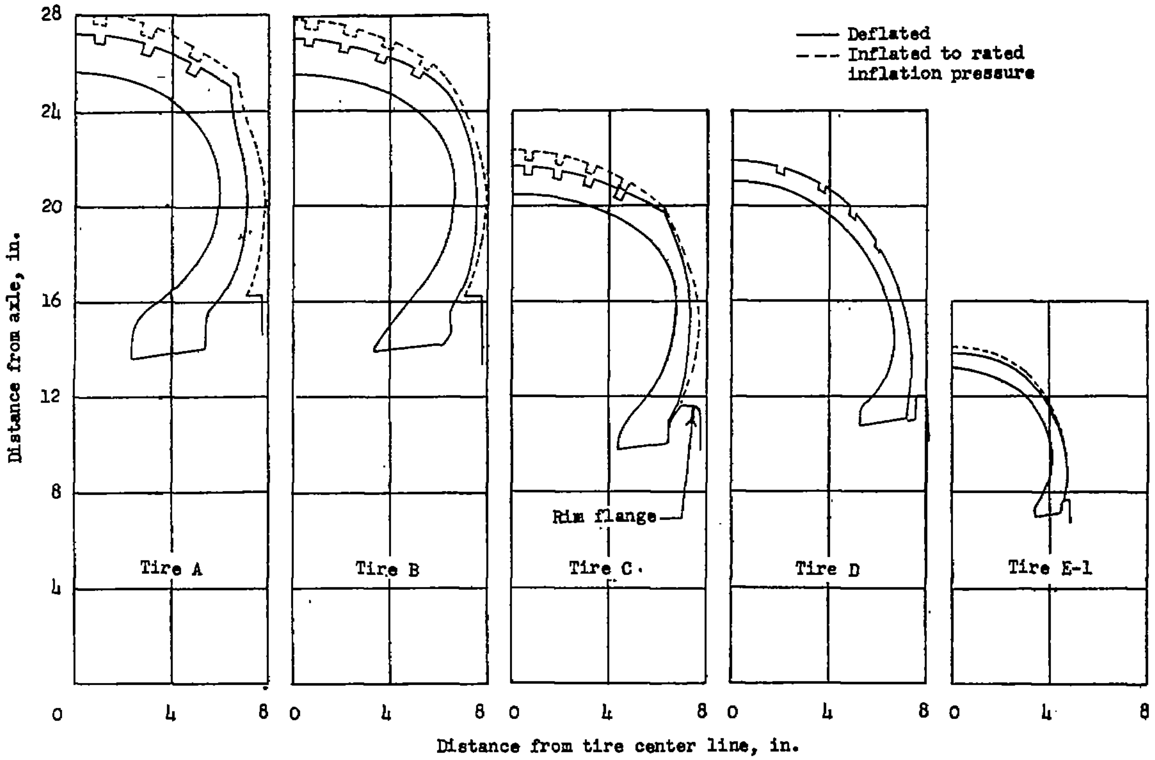

(b) Cross sections of tires.

Figure 1.- Concluded.

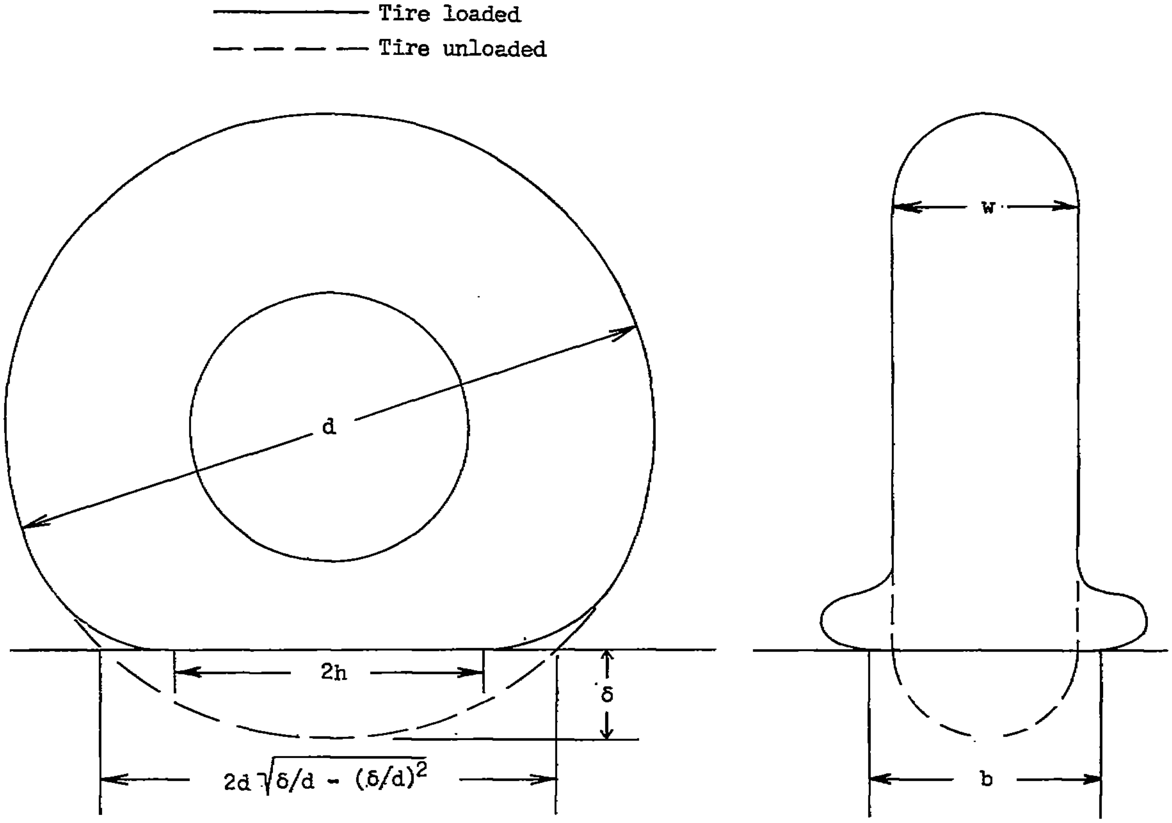

Figure 2.- Sketch of tire under pure vertical loading.

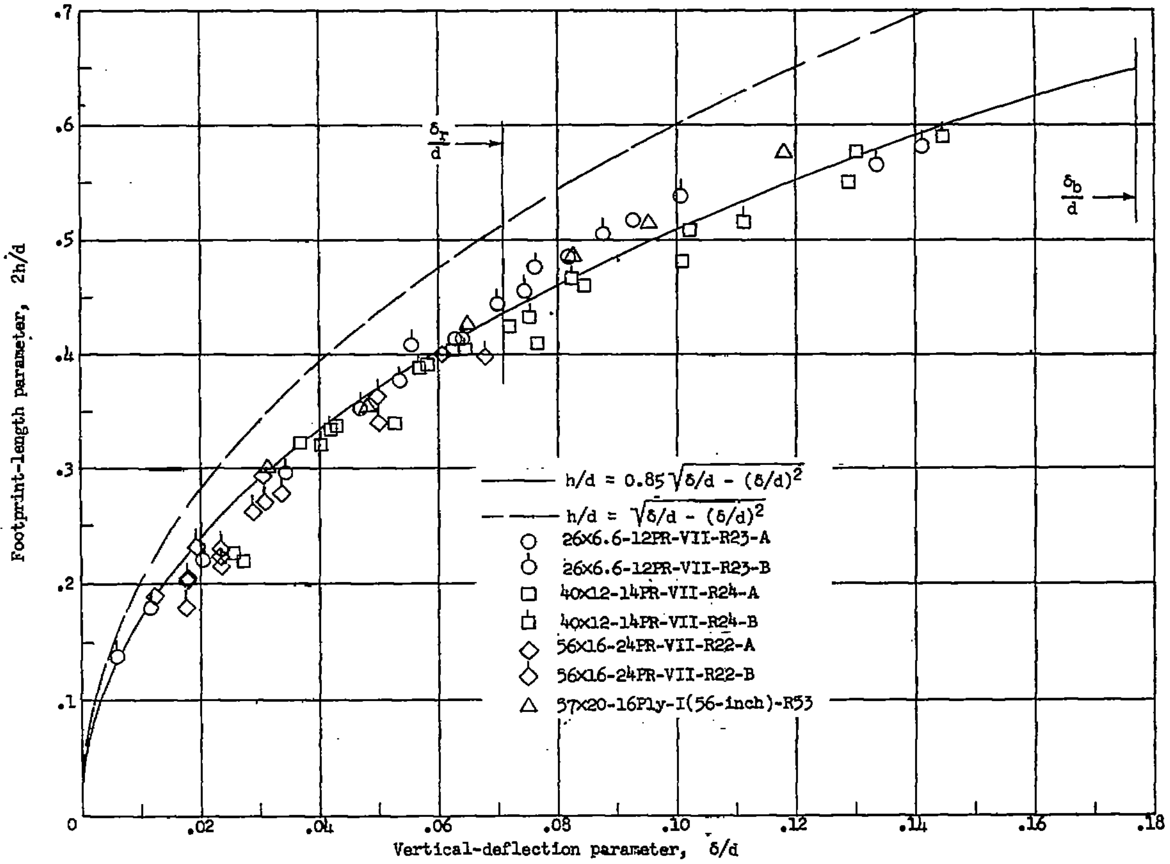

Figure 3.- Variation of footprint-length parameter with vertical-deflection parameter for several types I and VII tires.

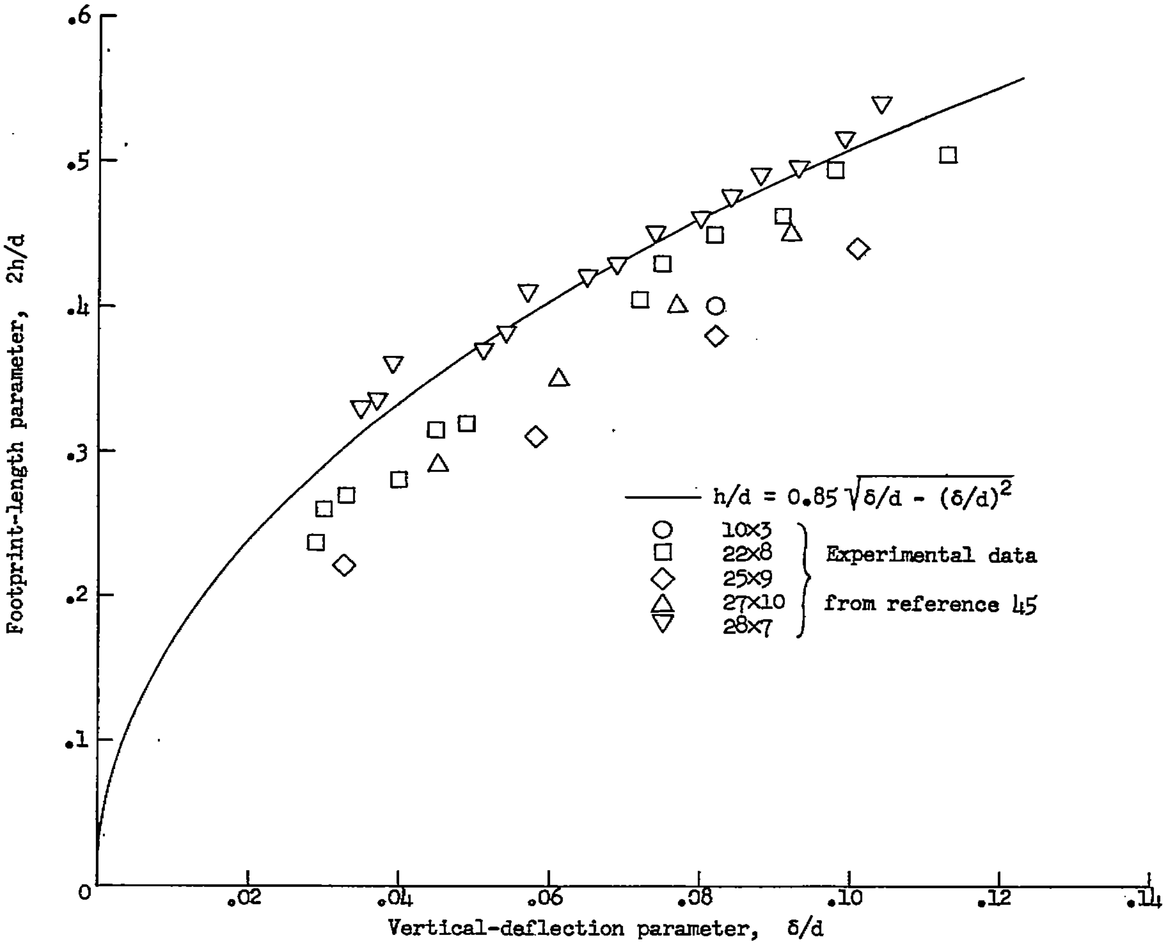

Figure 4.- Variation of footprint-length parameter with vertical-deflection parameter for several German aircraft tires.

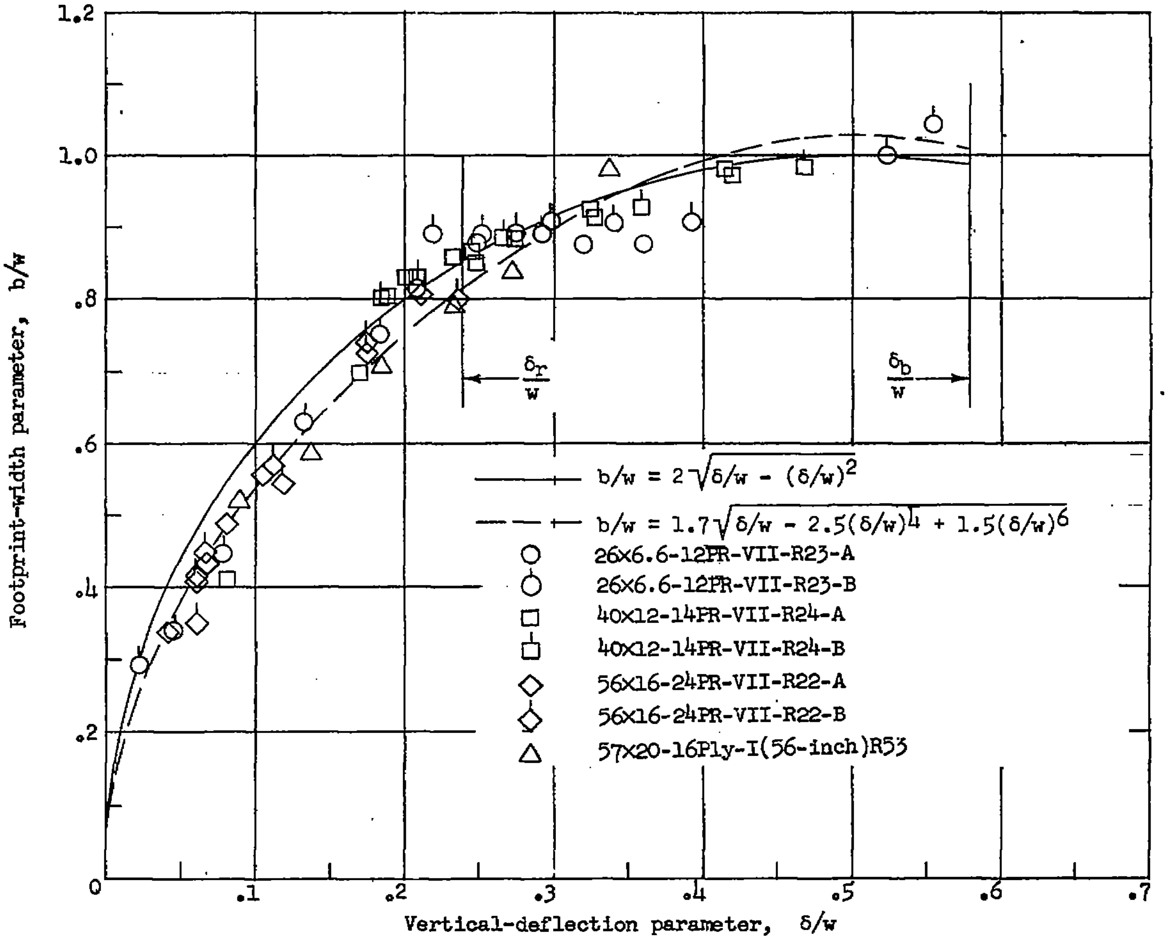

Figure 5.- Variation of footprint-width parameter with vertical-deflection parameter.

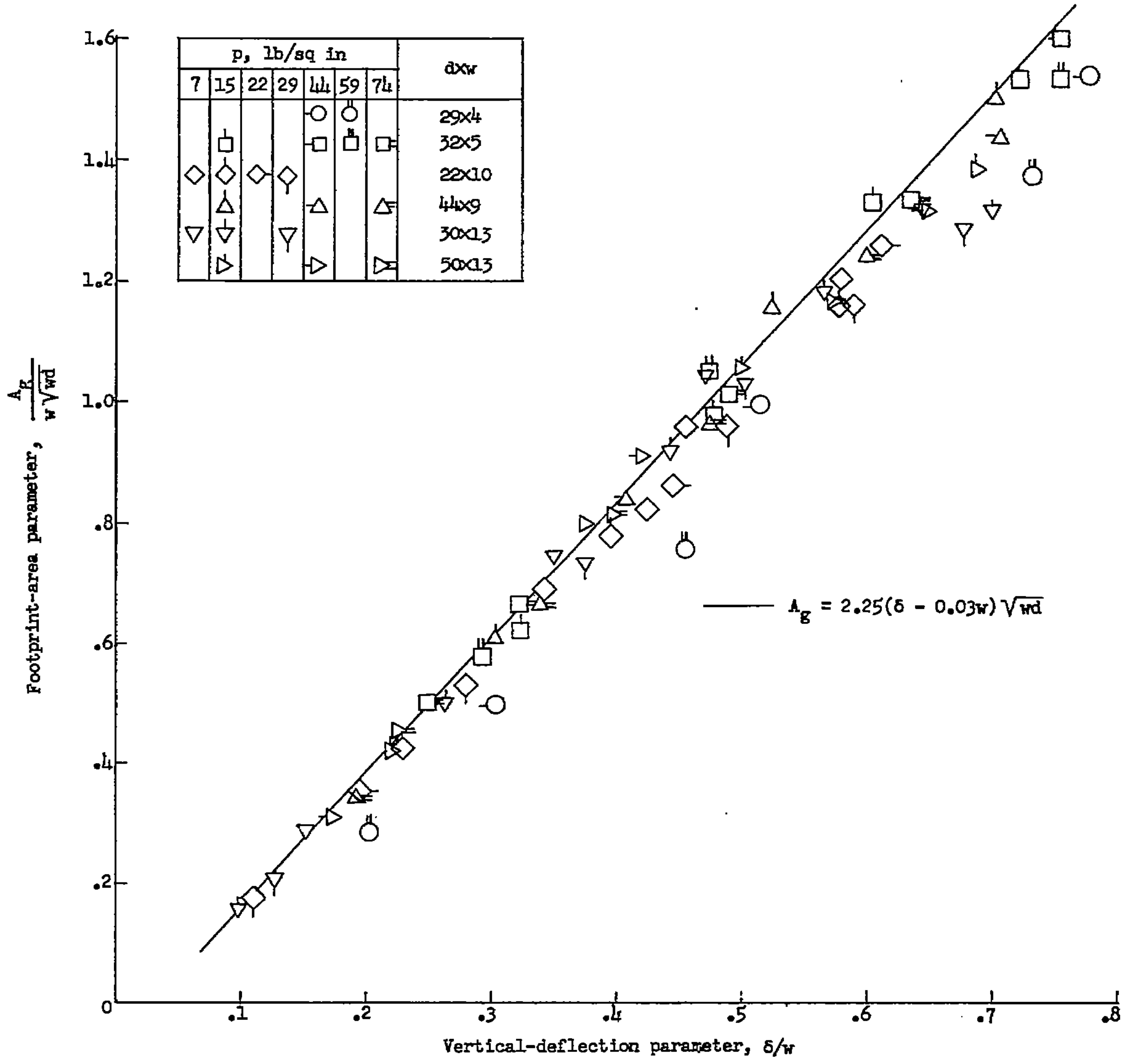

Figure 6.- Variation of gross-footprint-area parameter with vertical-deflection parameter for several obsolete tires. (Experimental data from ref. 38.)

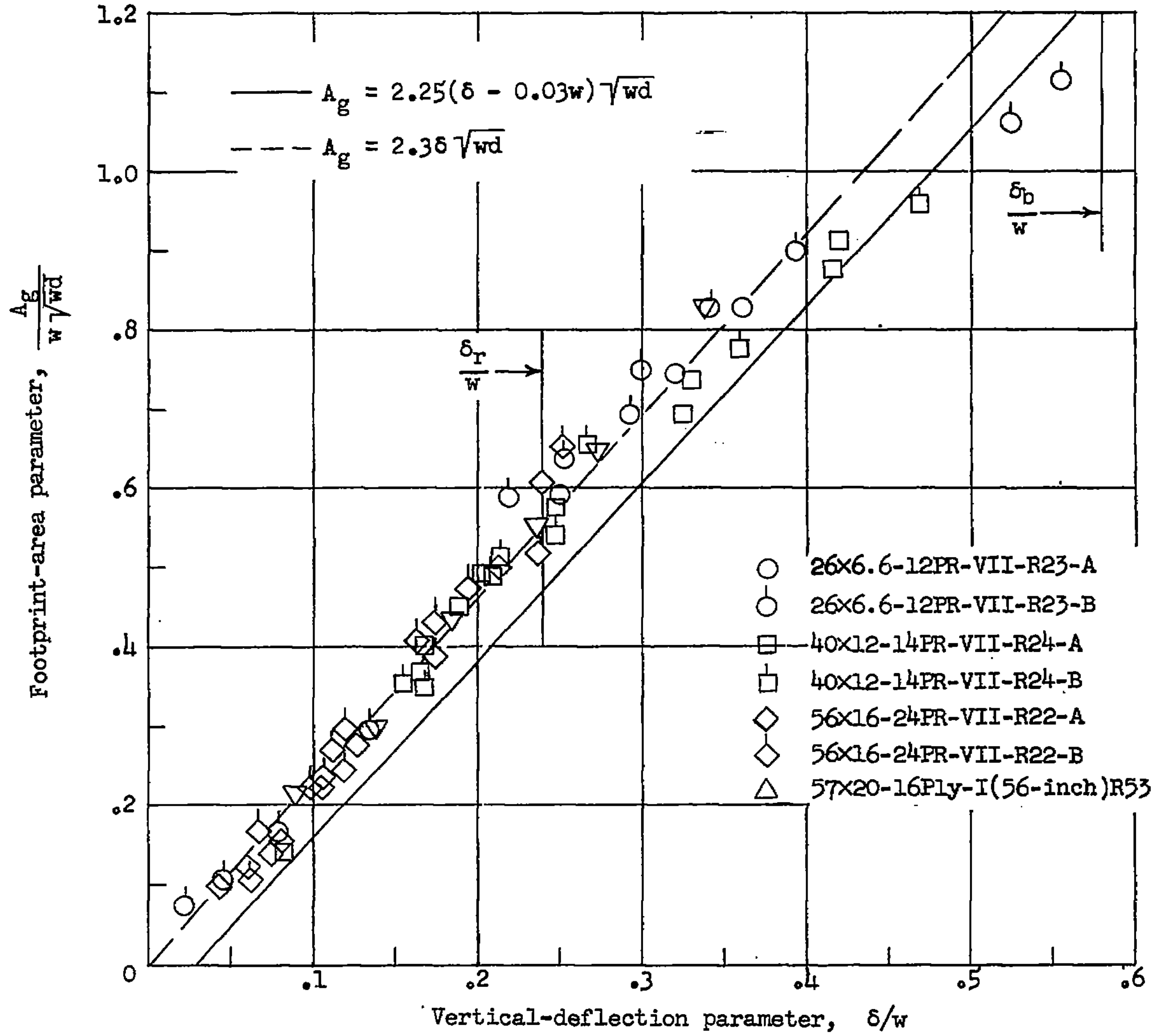

Figure 7.- Variation of gross-footprint-area parameter with vertical-deflection parameter for types I and VII tires.

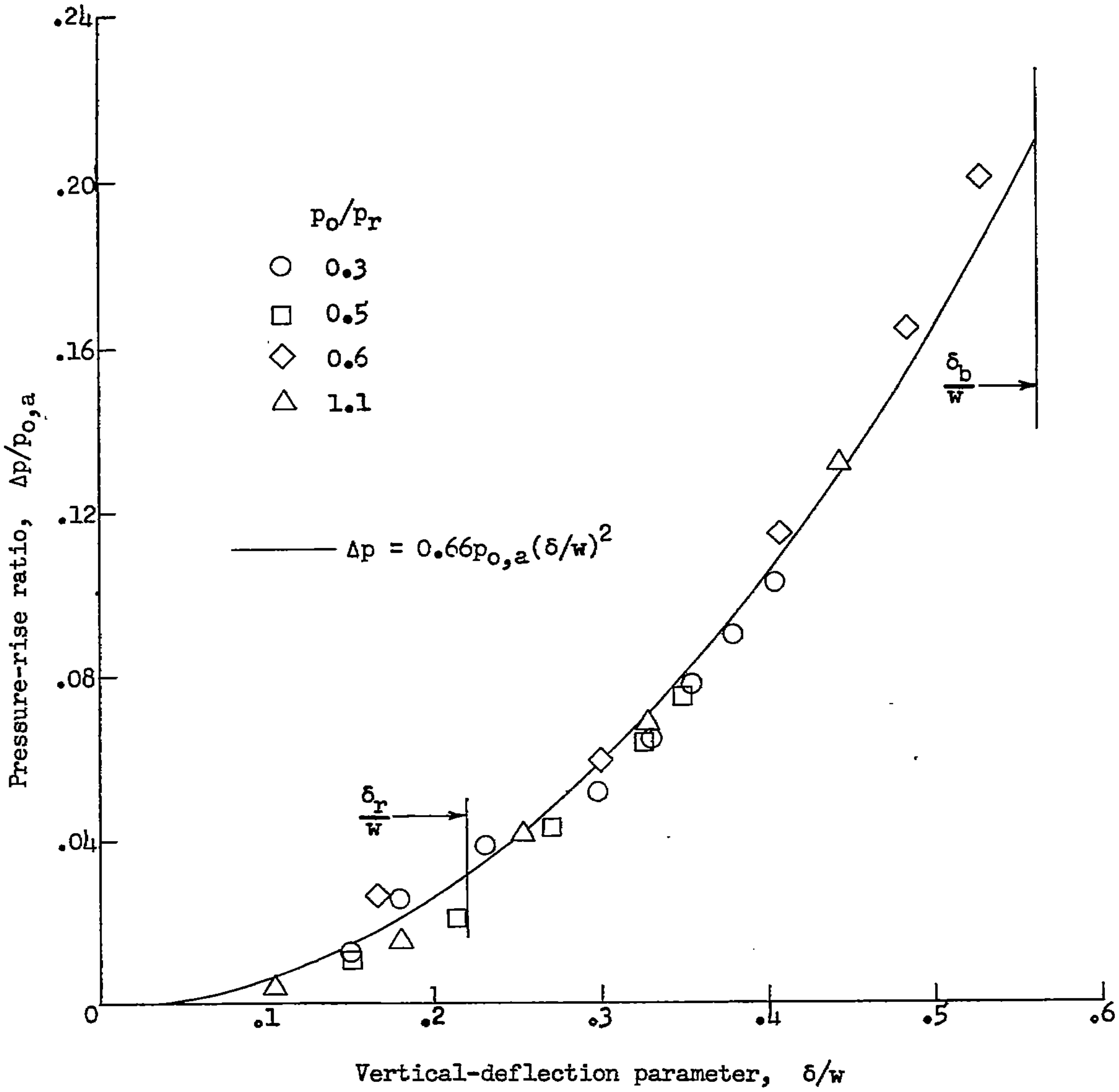

Figure 8.- Variation of pressure-rise ratio $\Delta p/p_{o,a}$ with vertical-deflection parameter for a 28×9-10PR-I(27-inch)R21-E2 tire.

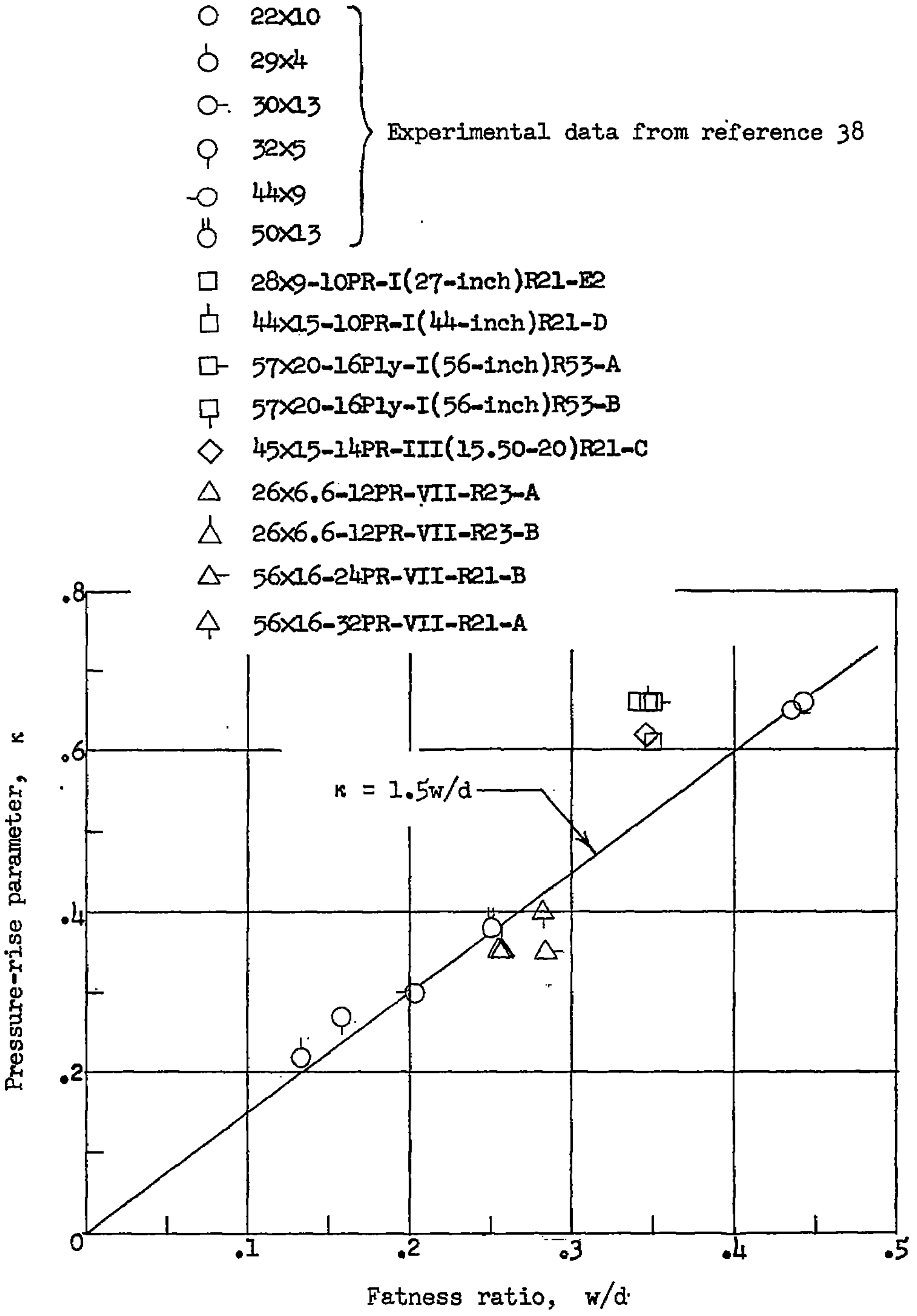

Figure 9.- Variation of pressure-rise parameter κ with tire fatness ratio.

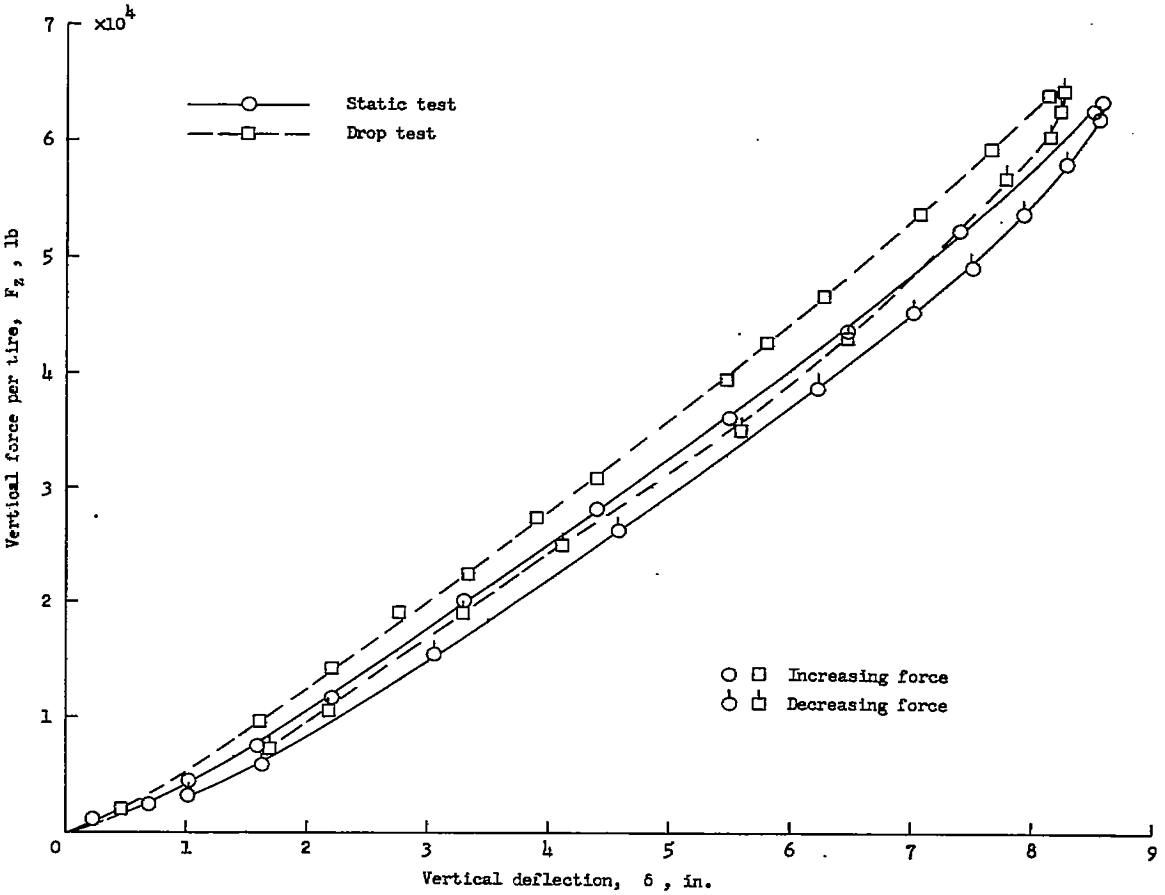

Figure 10.- Comparison of vertical-force-deflection curves from static test and from drop test without prerotation at initial vertical velocity of 9.9 feet per second. Data for pair of 57×20-16Ply-I-(56-inch)R53 tires. p_o = 80 pounds per square inch.

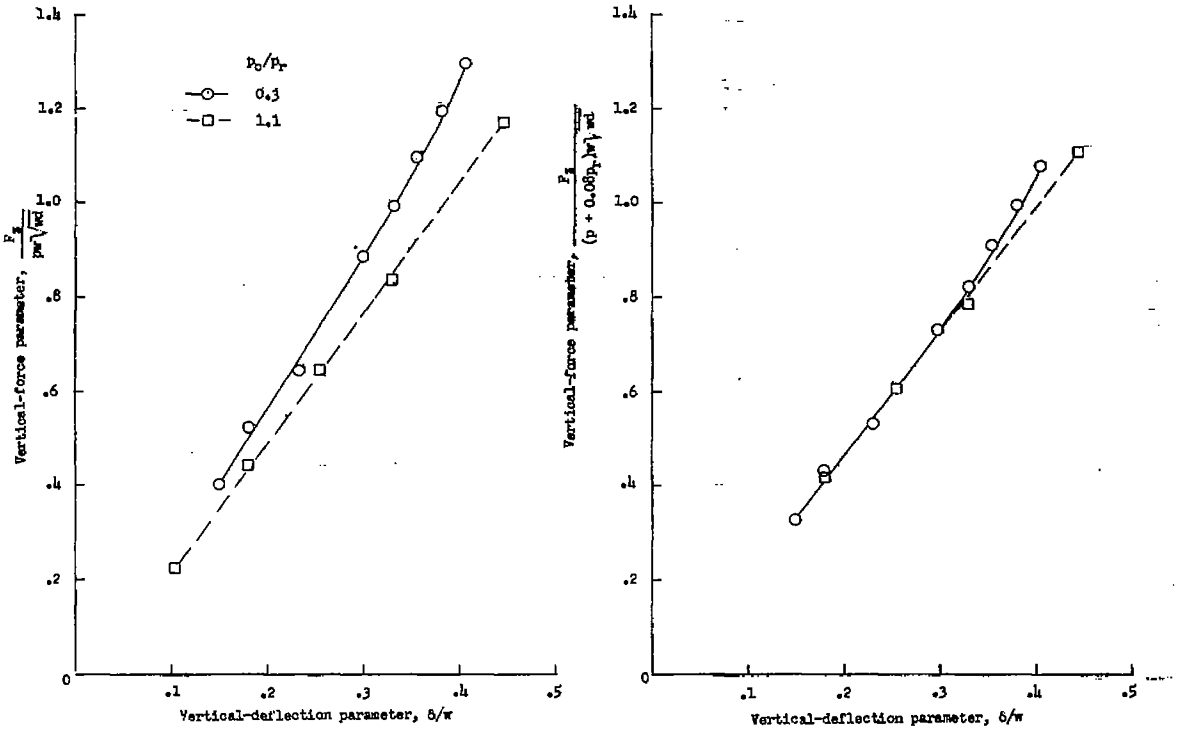

(a) Variation of $\frac{F_z}{pw\sqrt{wd}}$. (b) Variation of $\frac{F_z}{(p + 0.08p_r)w\sqrt{wd}}$.

Figure 11.- Experimental variation of two vertical-force parameters with vertical-deflection parameter for a 28×9-10PR-I(27-inch)R21-E2 tire at two different inflation pressures.

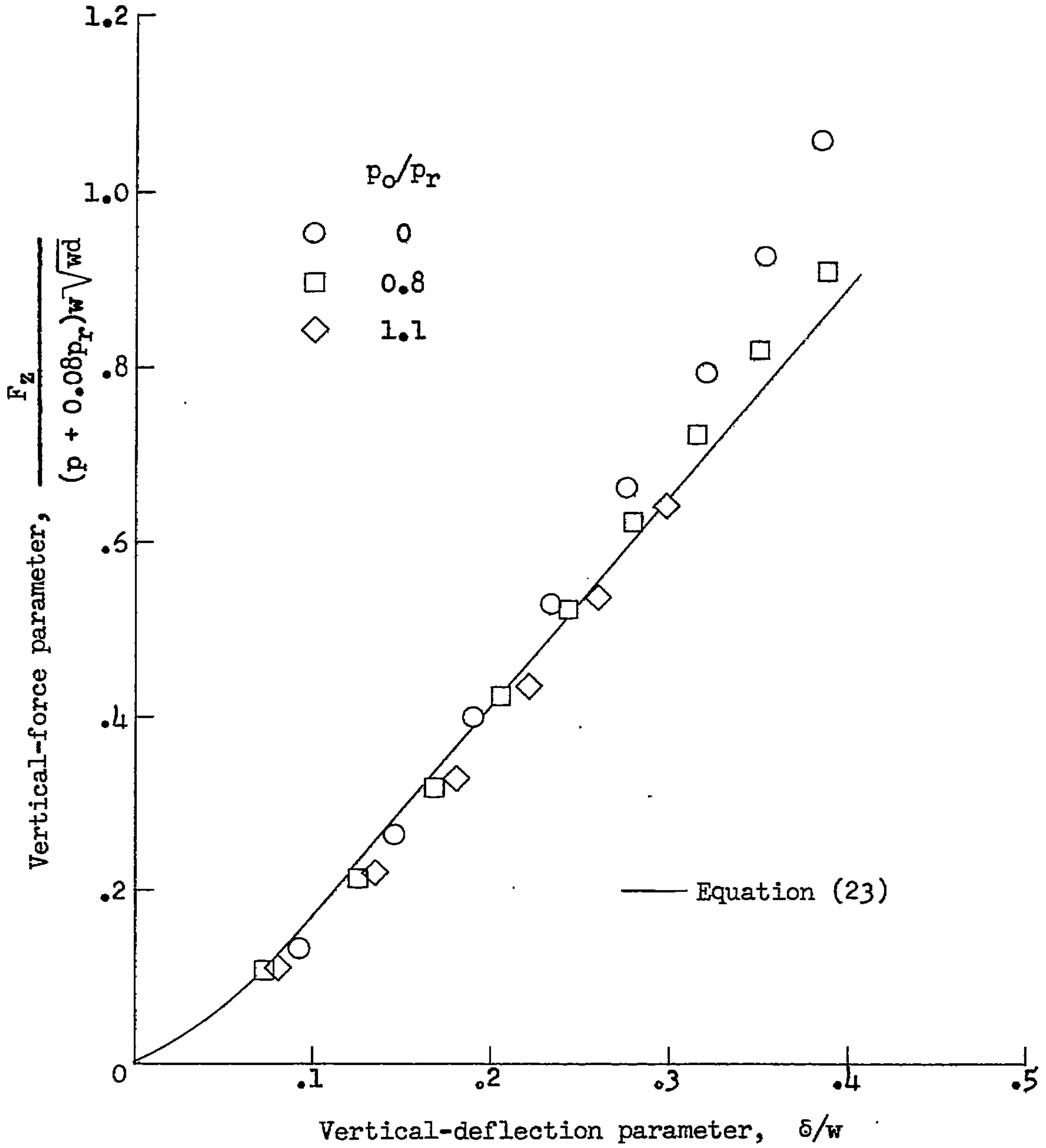

Figure 12.- Variation of vertical-force parameter with vertical-deflection parameter for a 56×16-32PR-VII-R21-A tire at several inflation pressures.

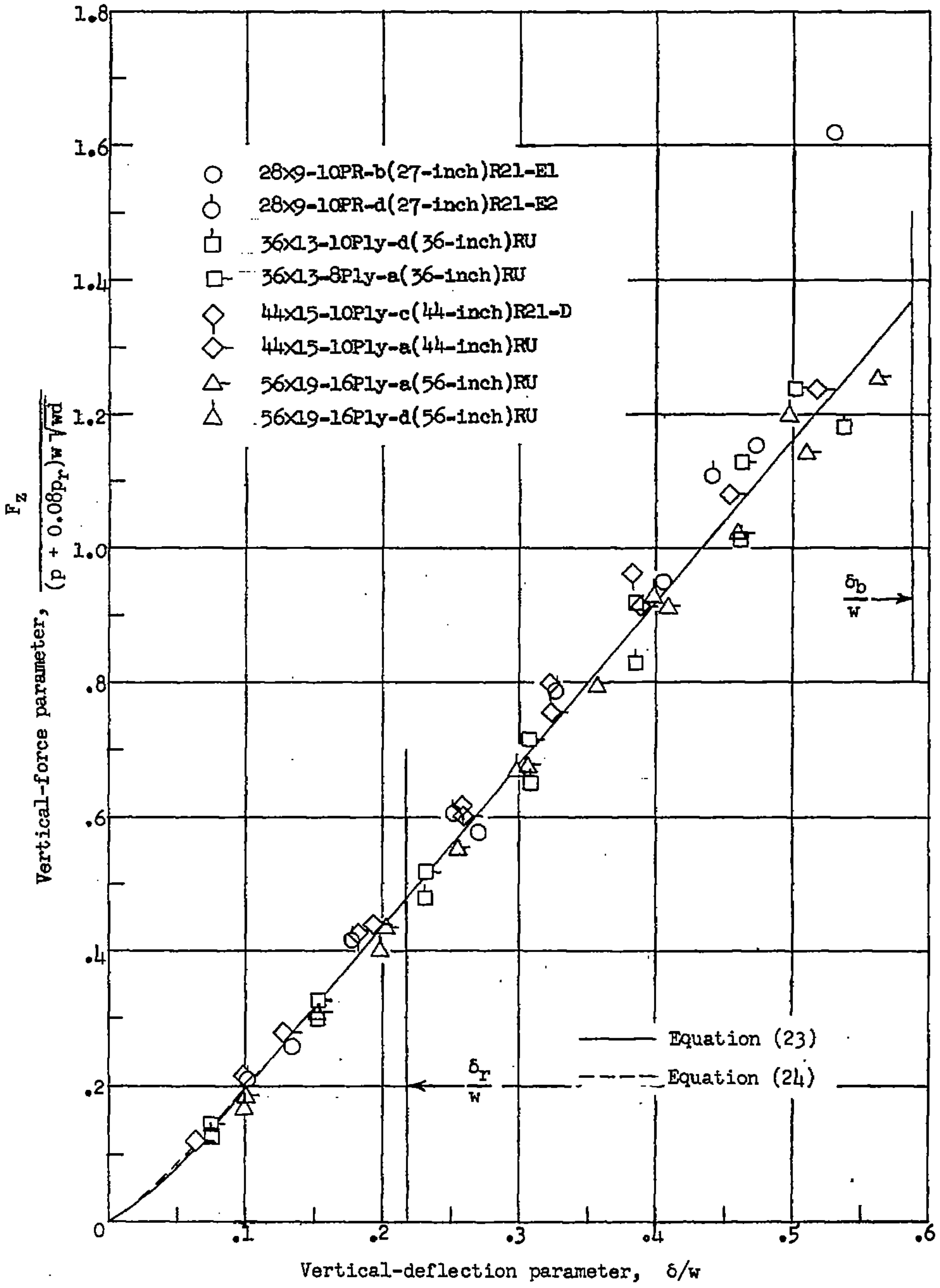

(a) Type I tires.

Figure 13.- Variation of vertical-force parameter with vertical deflection for several types I, III, and VII tires.

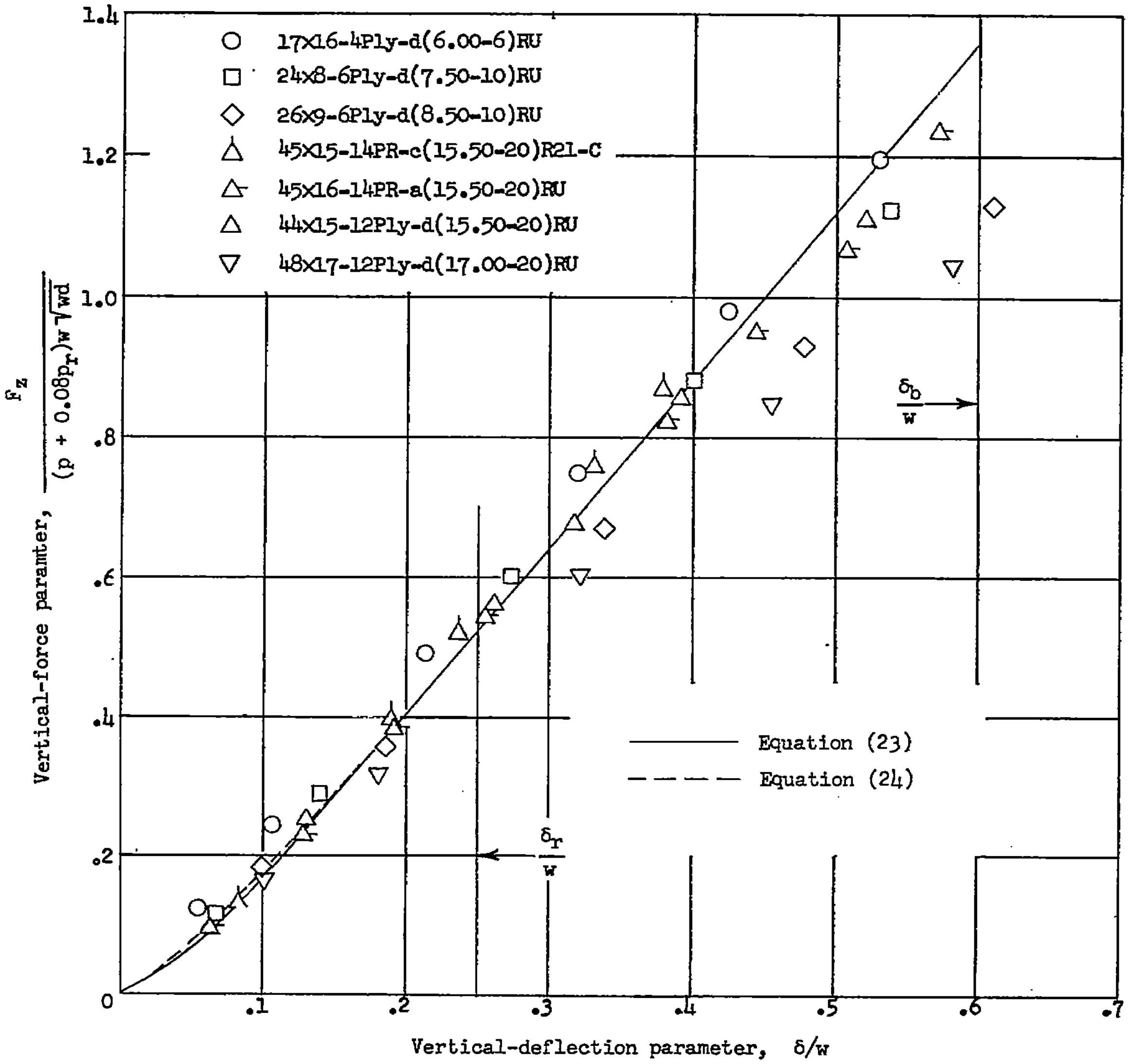

(b) Type III tires.

Figure 13.- Continued.

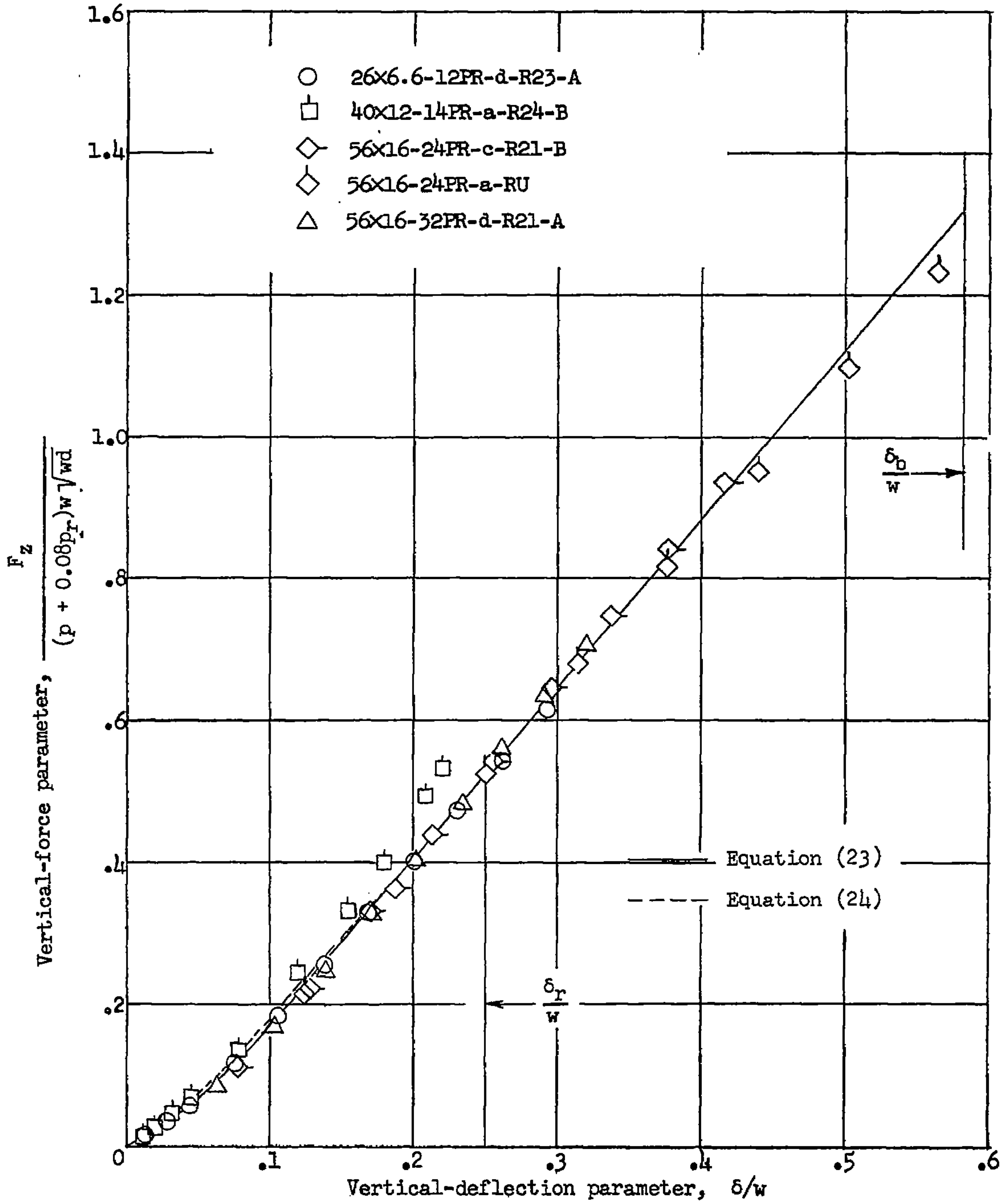

(c) Type VII tires.

Figure 13.- Concluded.

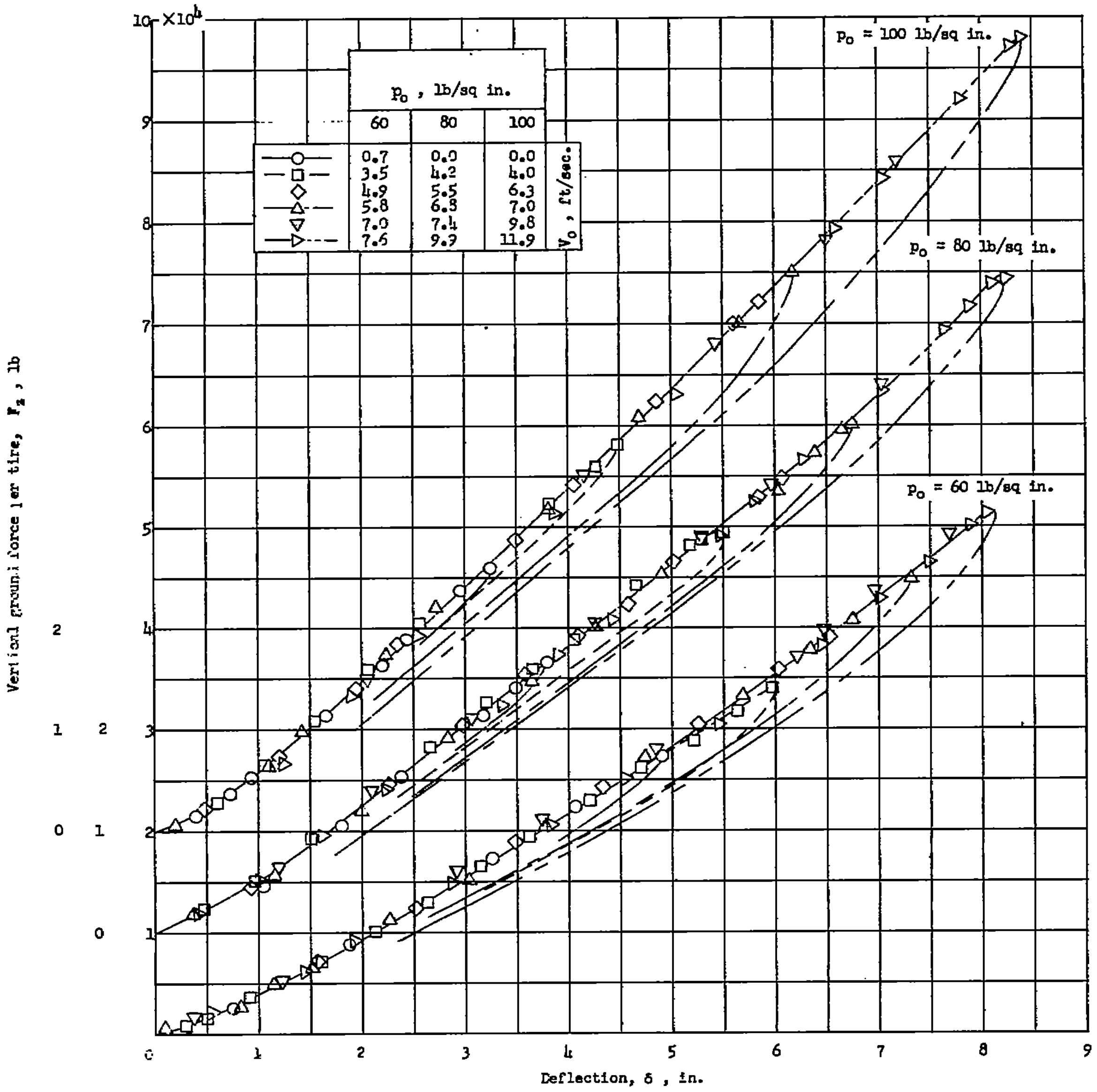

Figure 14.- Variations of vertical ground force, with vertical tire deflection obtained from drop tests without prerotation for pair of 57×20-16Ply-I(56-inch)R53 tires.

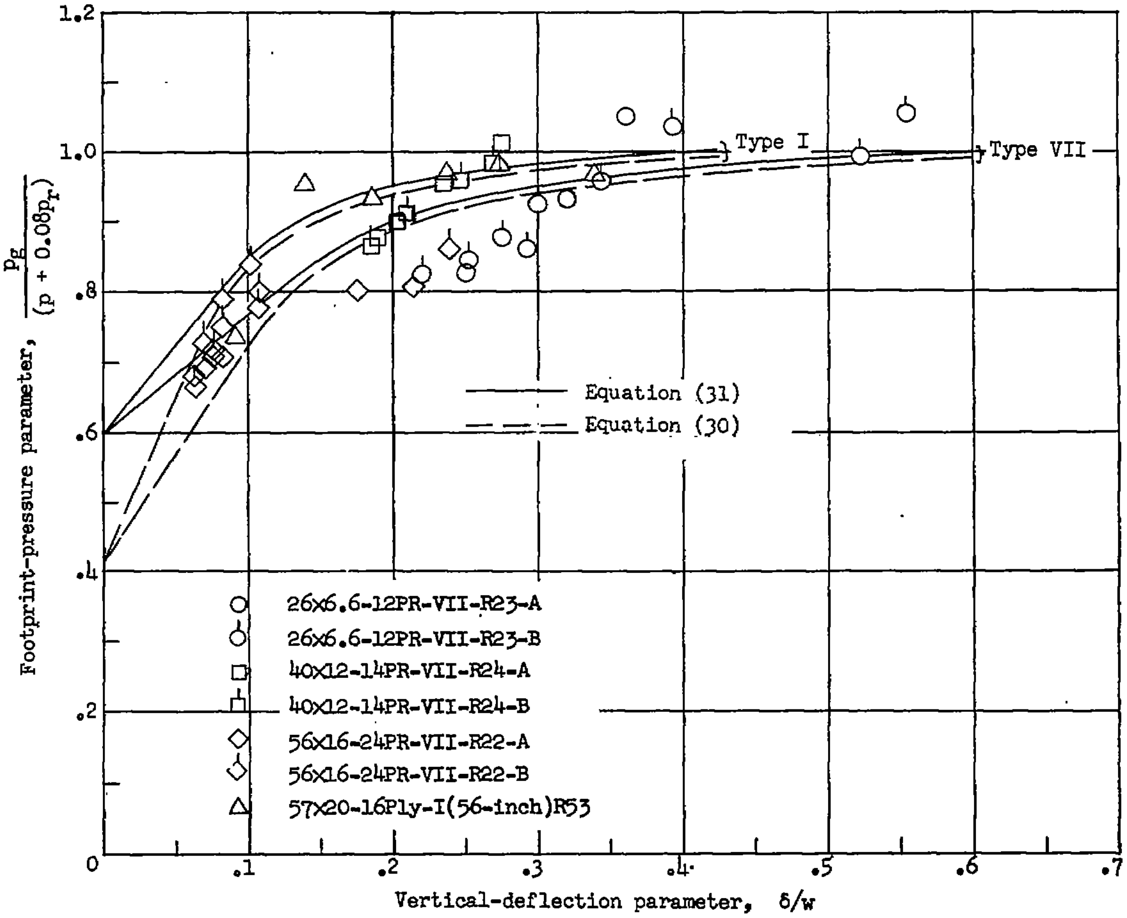

Figure 15.- Variation of footprint-pressure parameter with vertical-deflection parameter.

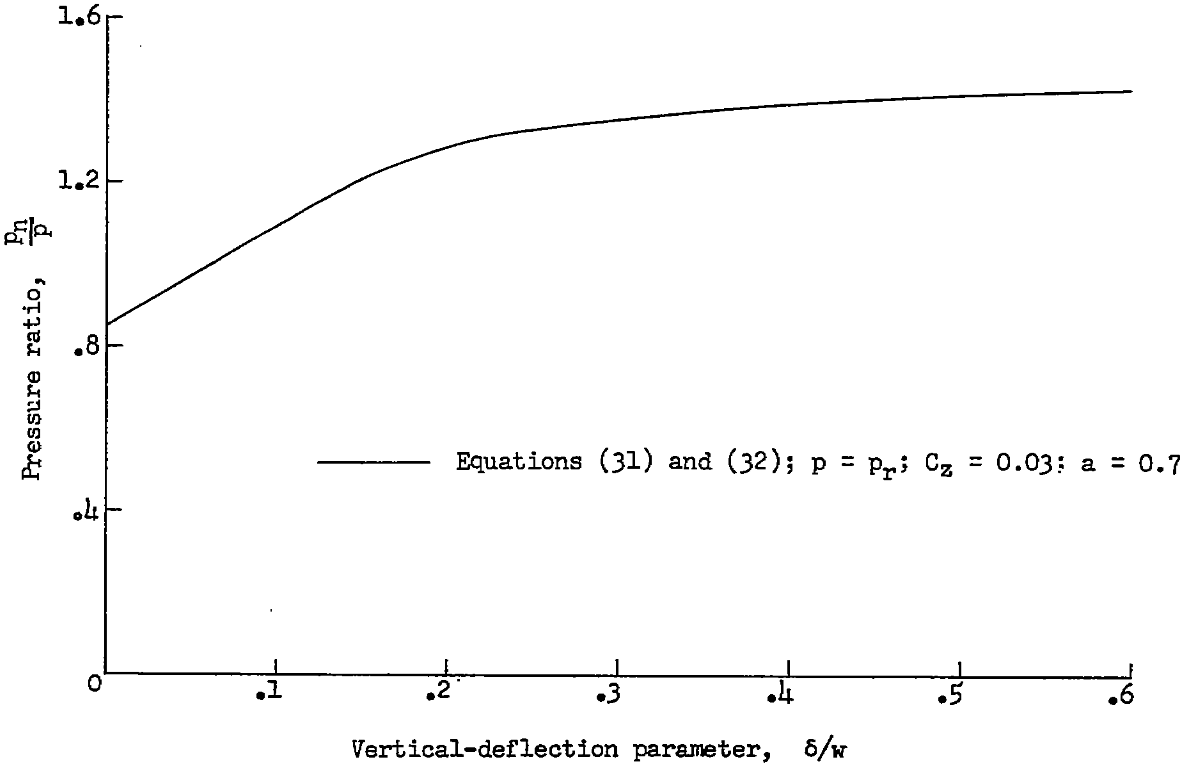

Figure 16.- Variation with vertical-deflection parameter of ratio of net footprint pressure to inflation pressure.

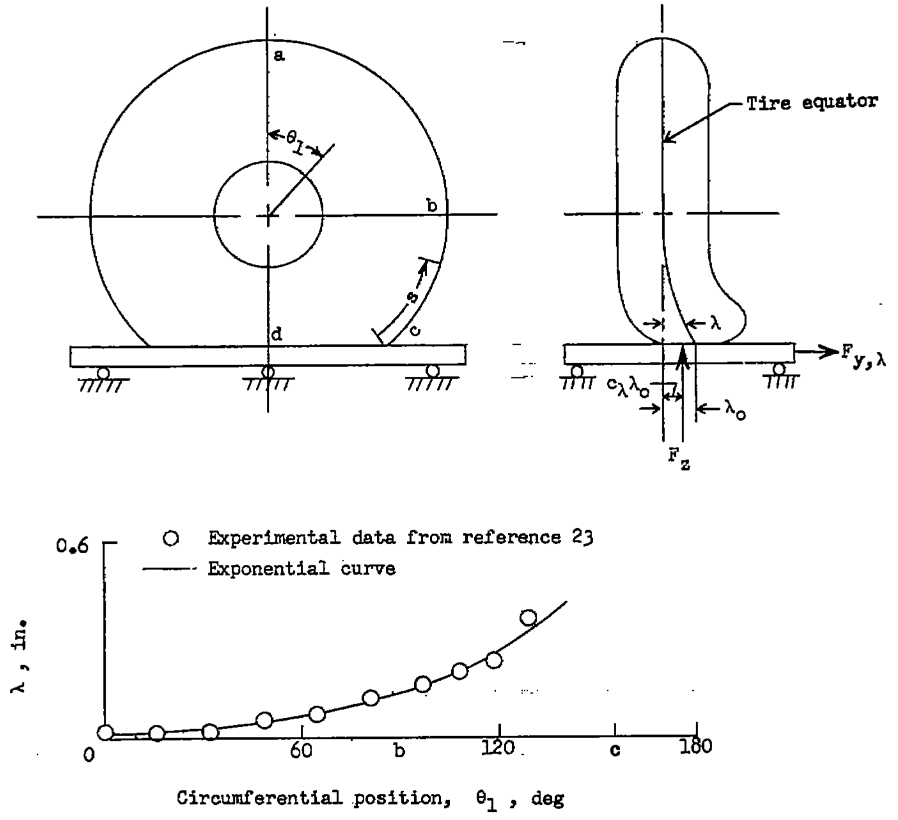

Figure 17.- Sketch illustrating tire lateral distortion for combined vertical and lateral loading.

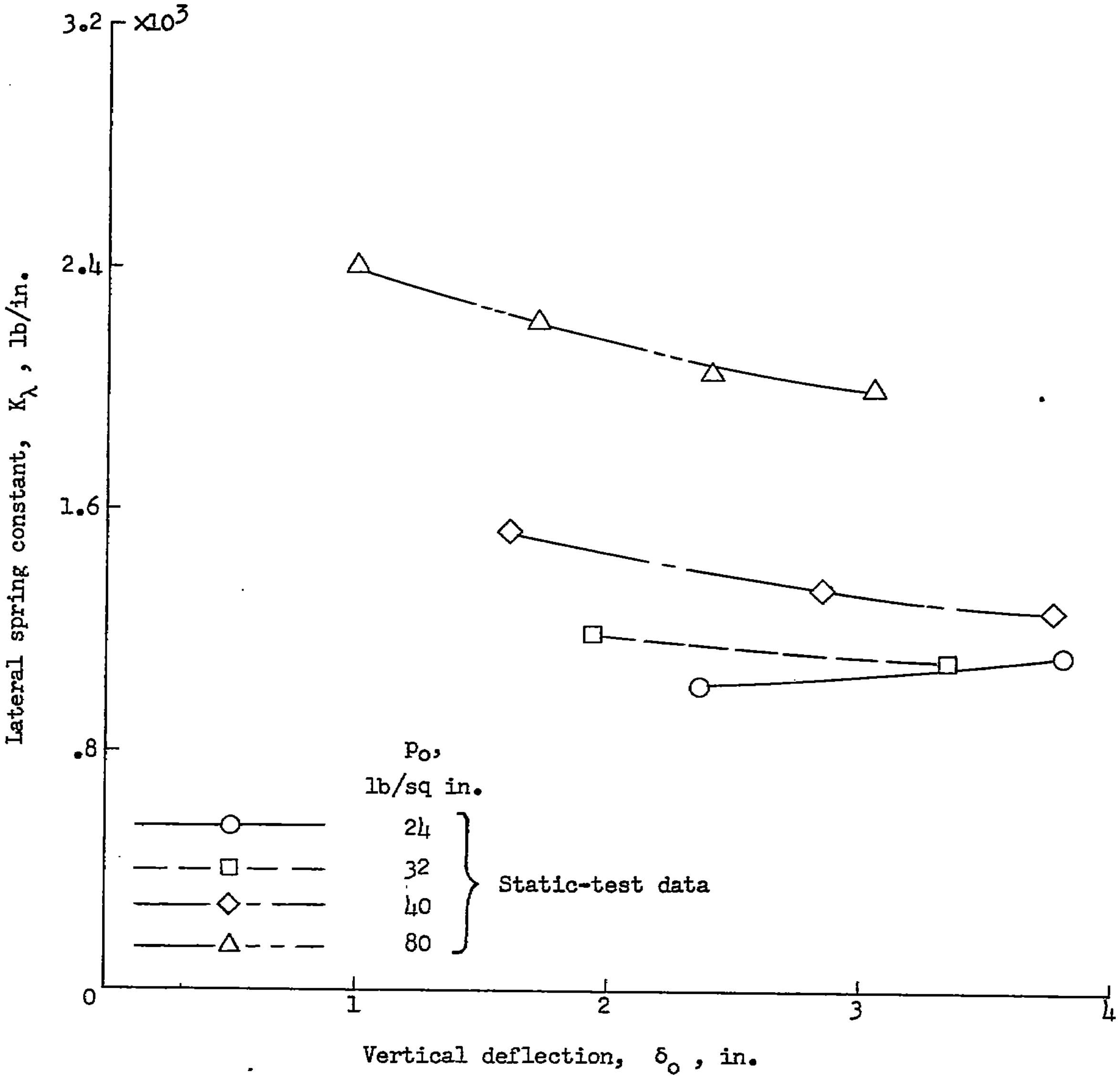

Figure 18.- Variation of lateral spring constant with vertical deflection and inflation pressure for a 28×9-10PR-I(27-inch)-R21-E2 tire.

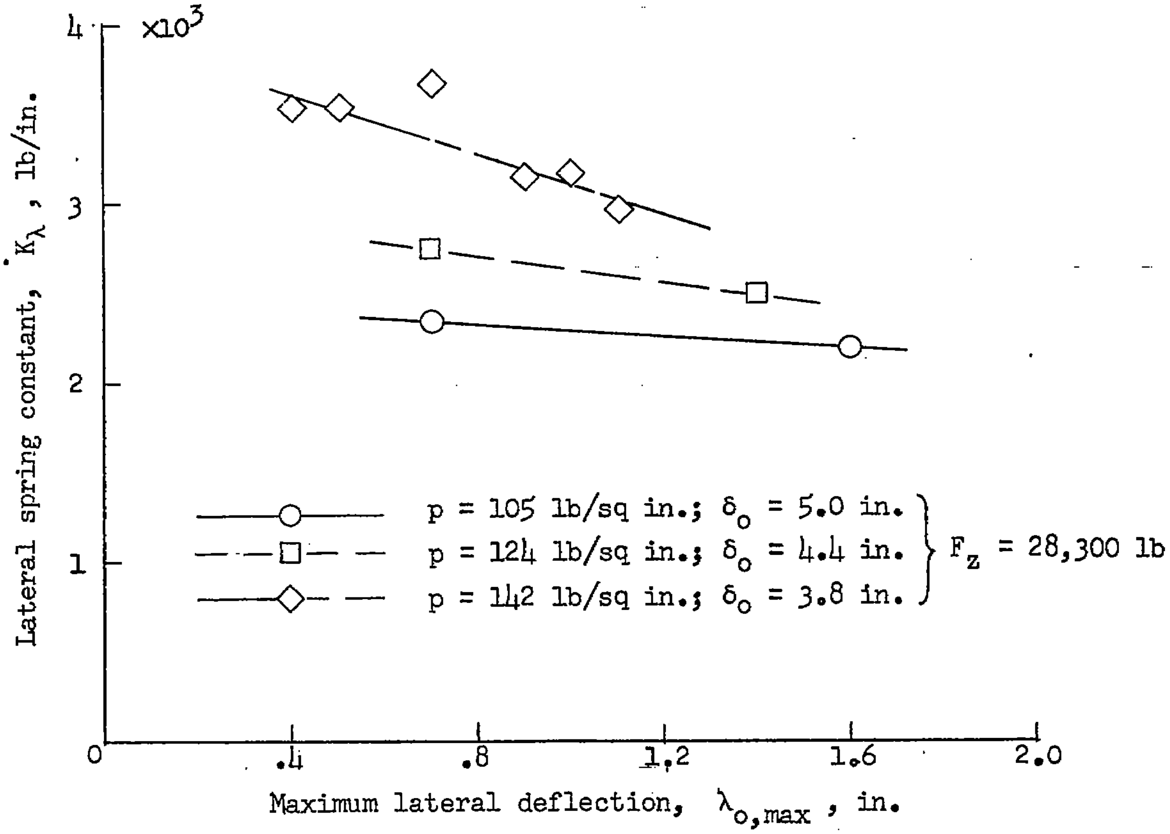

(a) Static data for 40×12-14PR-R24 tires.

Figure 19.- Variation of lateral spring constant with amplitude of lateral deflection for two pairs of type VII tires.

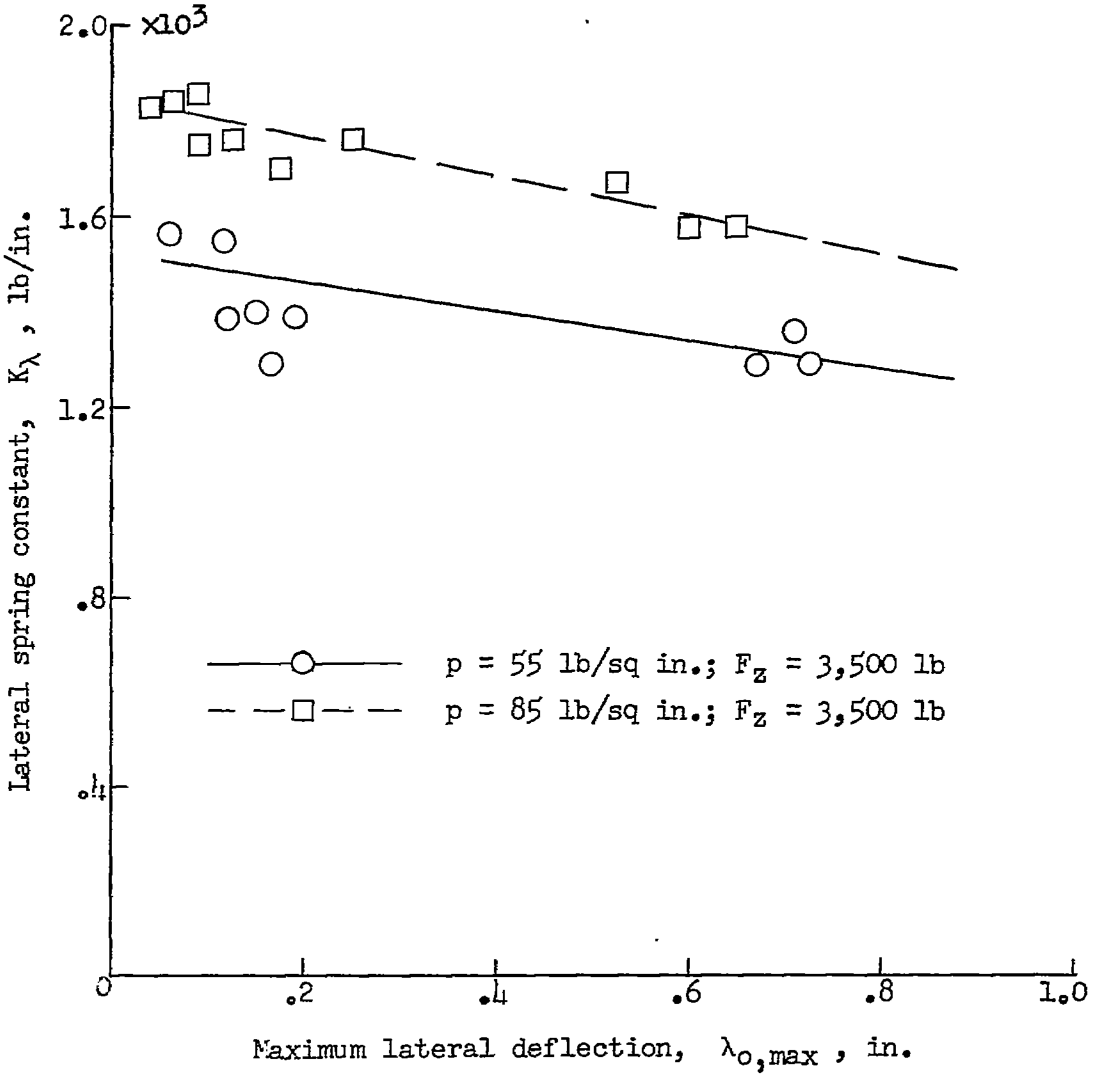

(b) Vibration data for 24×7.7-R25-B tires.

Figure 19.- Concluded.

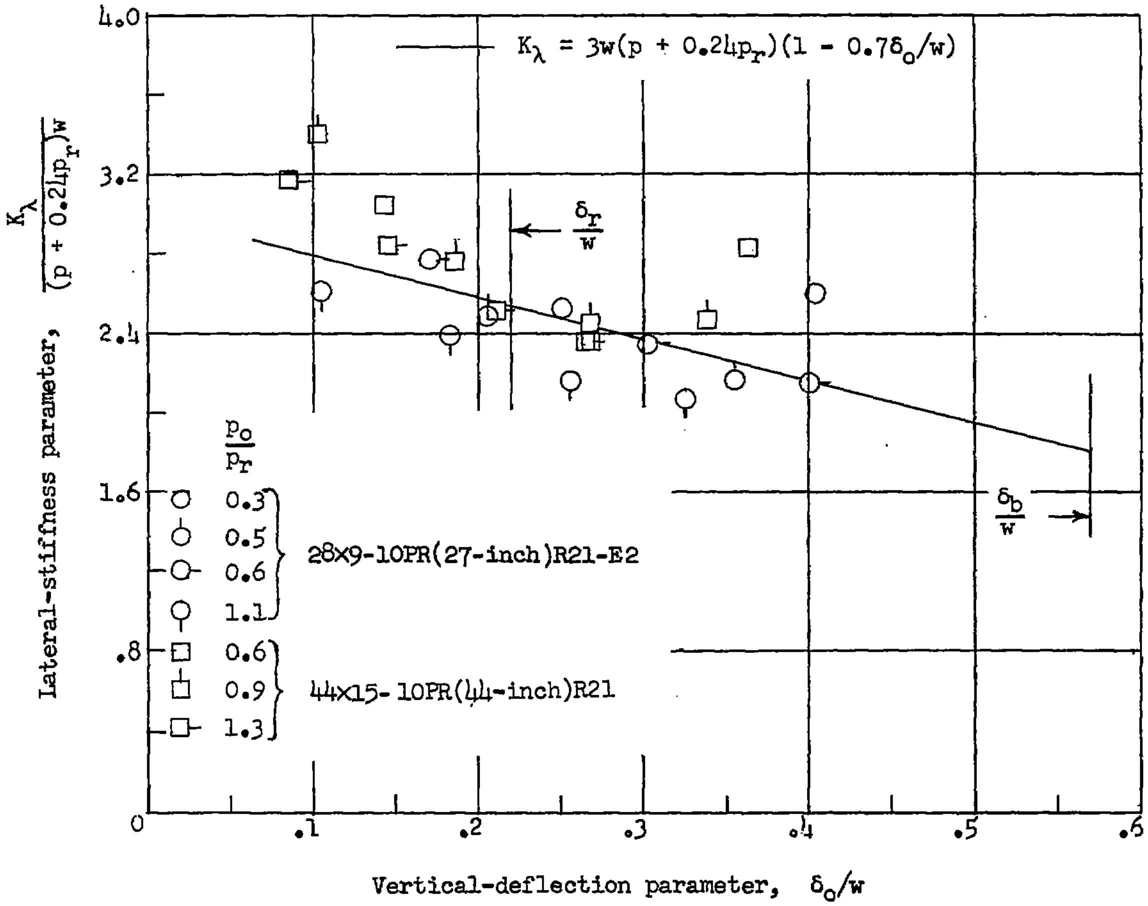

(a) Type I tires.

Figure 20.- Variation of lateral-stiffness parameter with vertical-deflection parameter for types I, III, and VII tires.

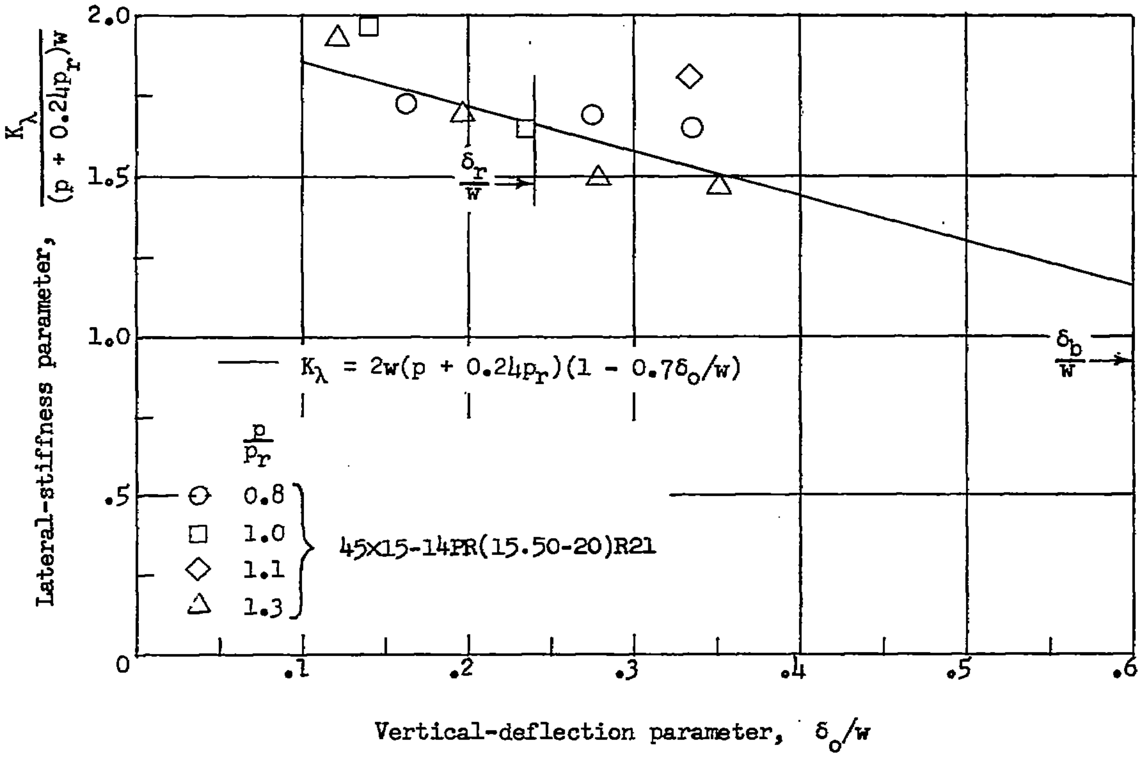

(b) Type III tire.

Figure 20.- Continued.

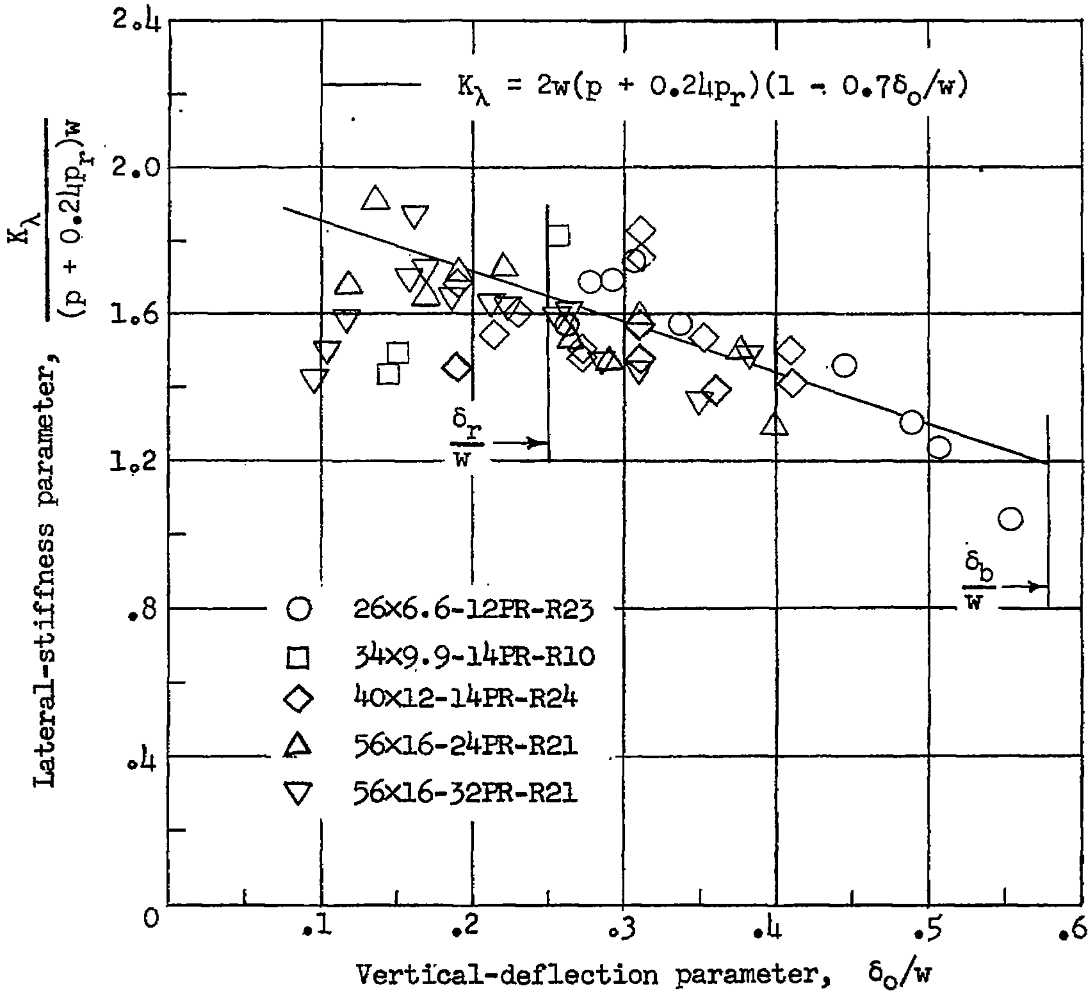

(c) Type VII tires.

Figure 20.- Concluded.

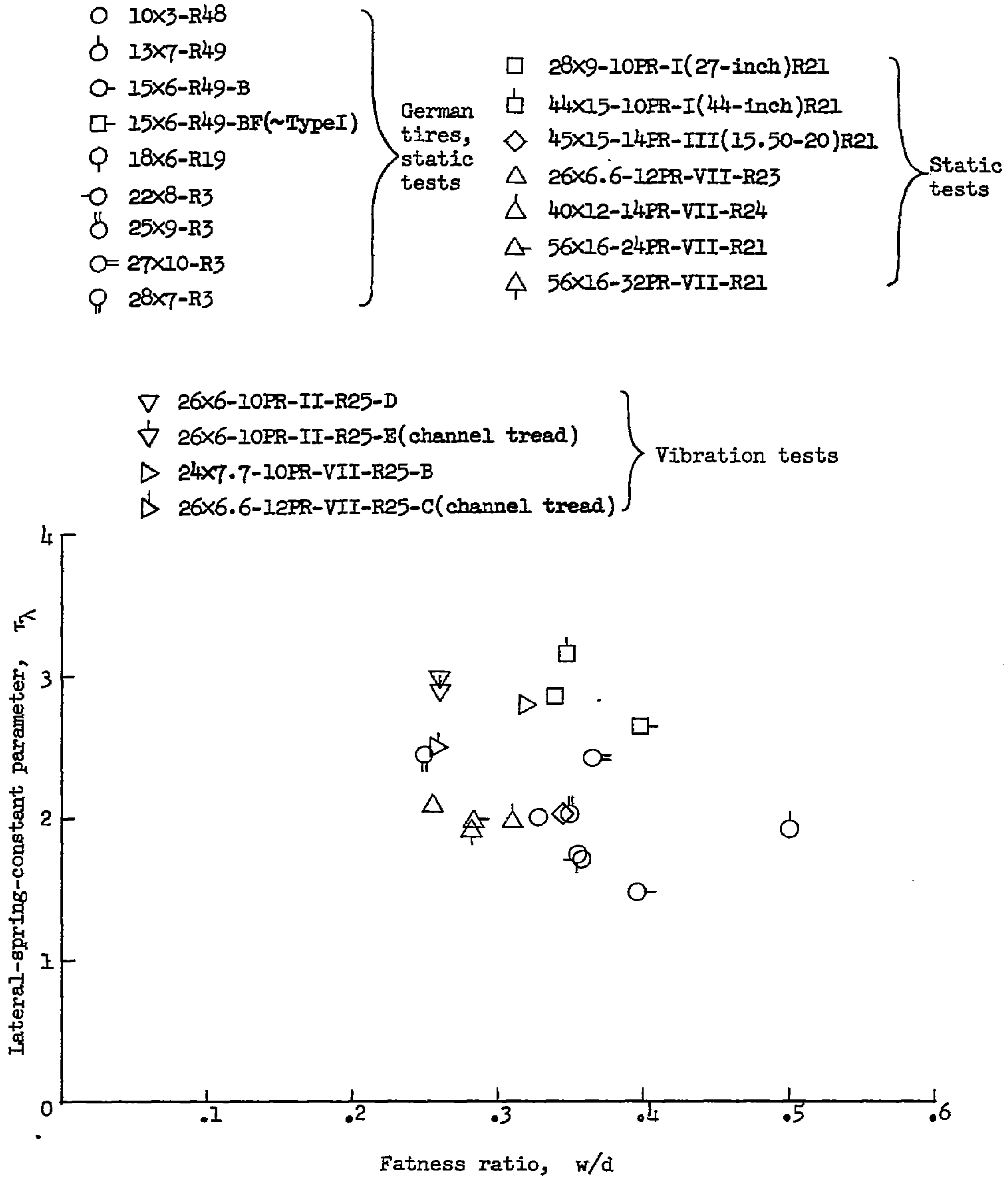

Figure 21.- Variation of lateral-spring-constant parameter τ_λ with fatness ratio.

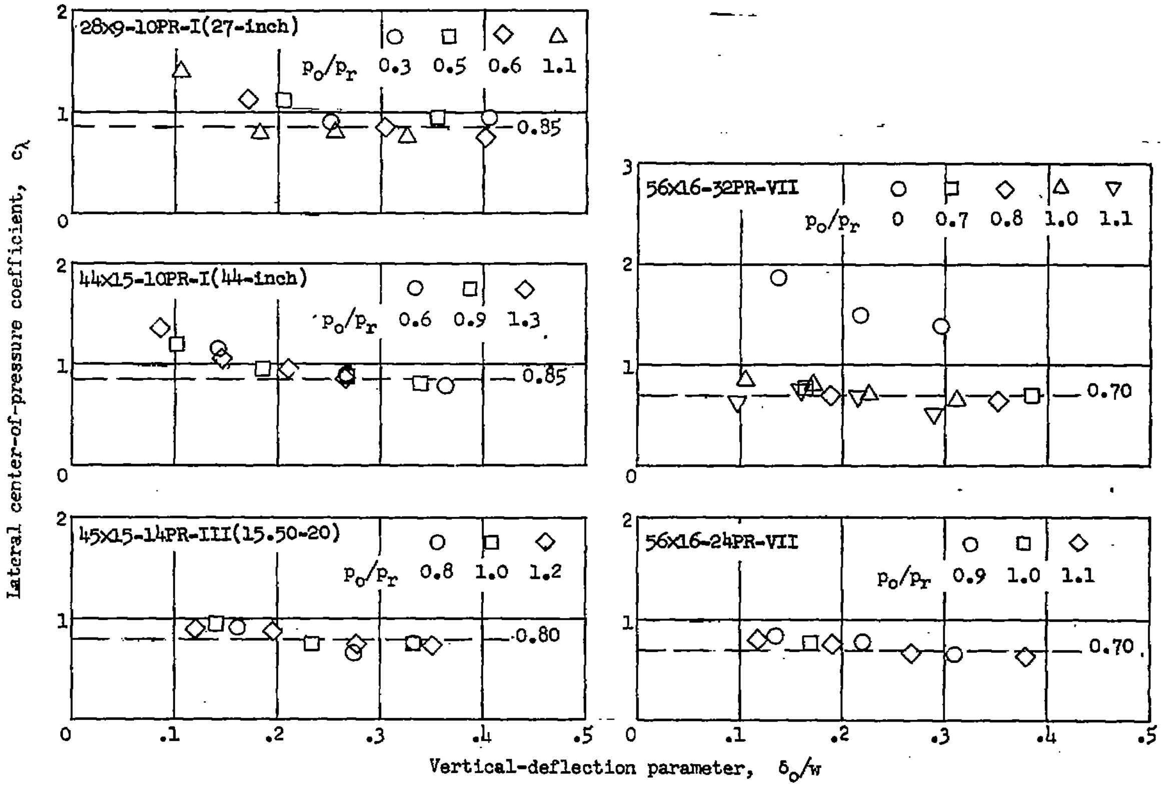

Figure 22.- Variation of lateral center-of-pressure coefficient with vertical-deflection parameter for types I, III, and VII tires. (Experimental data from ref. 21.)

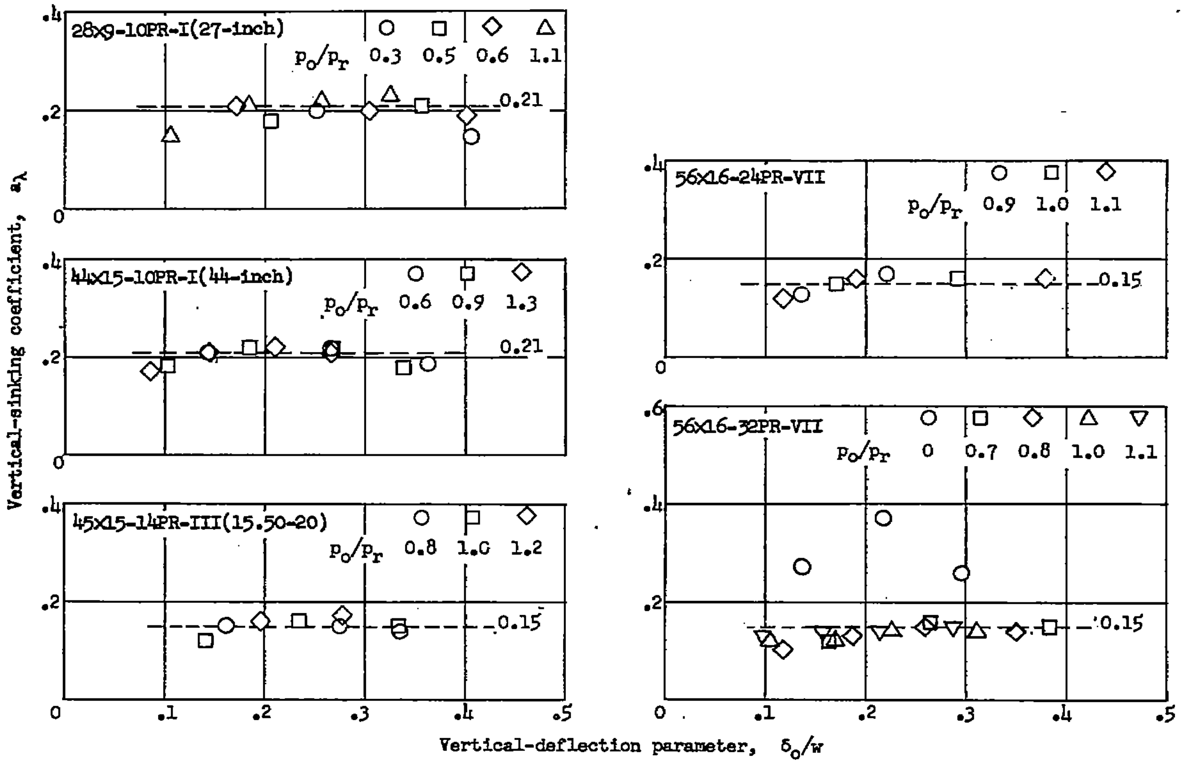

Figure 23.- Variation of vertical-sinking coefficient with vertical-deflection parameter for types I, III, and VII tires. (Experimental data from ref. 21.)

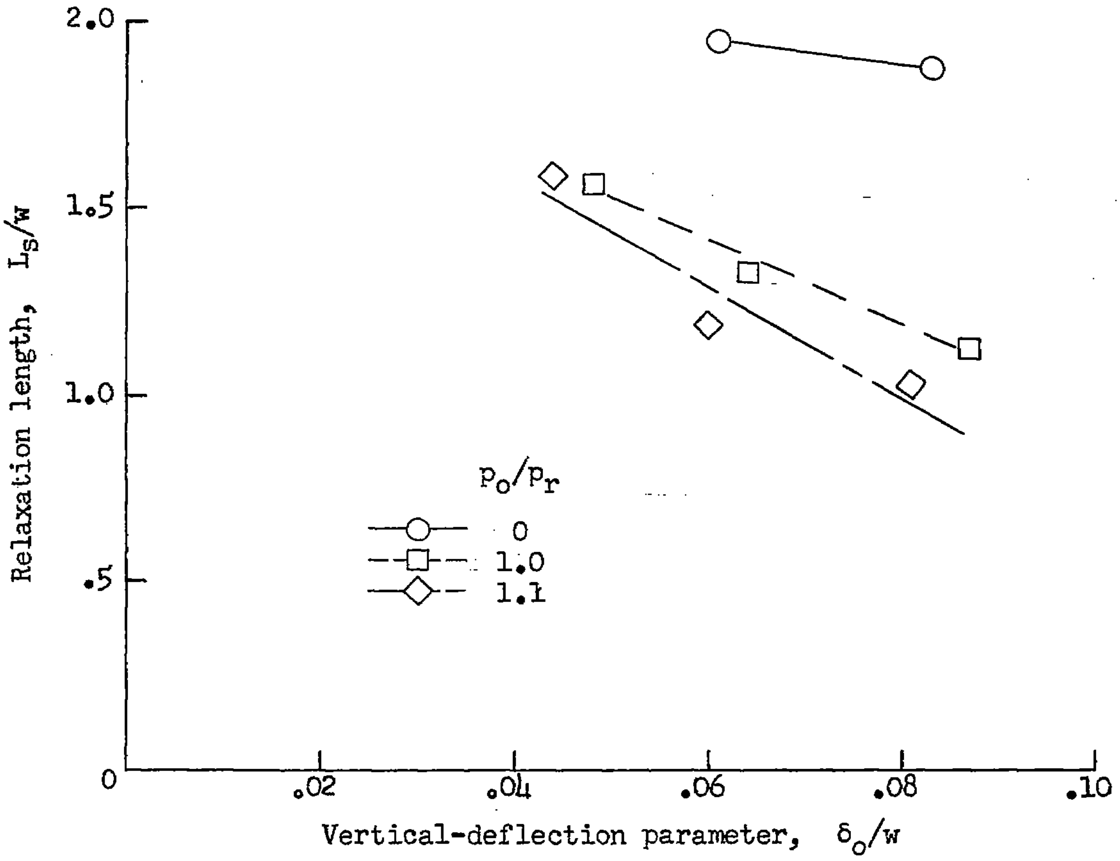

Figure 24.- Experimental variation of static relaxation length with vertical-deflection parameter and inflation pressure for a 56×16-32PR-VII-R21A tire.

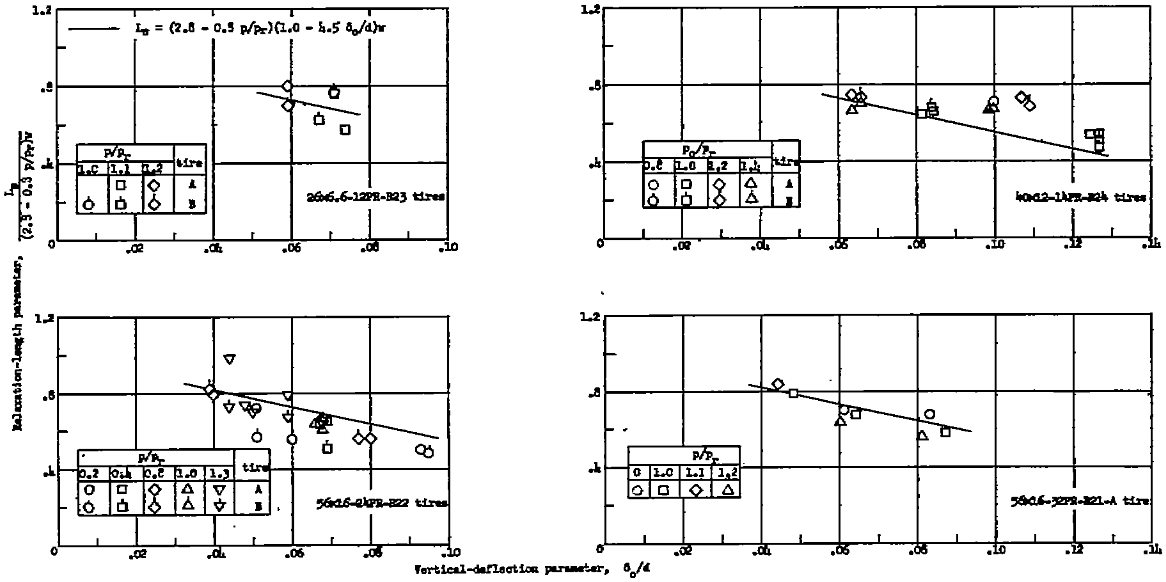

(a) Type VII tires.

Figure 25.- Variation of static-relaxation-length parameter with vertical-deflection parameter.

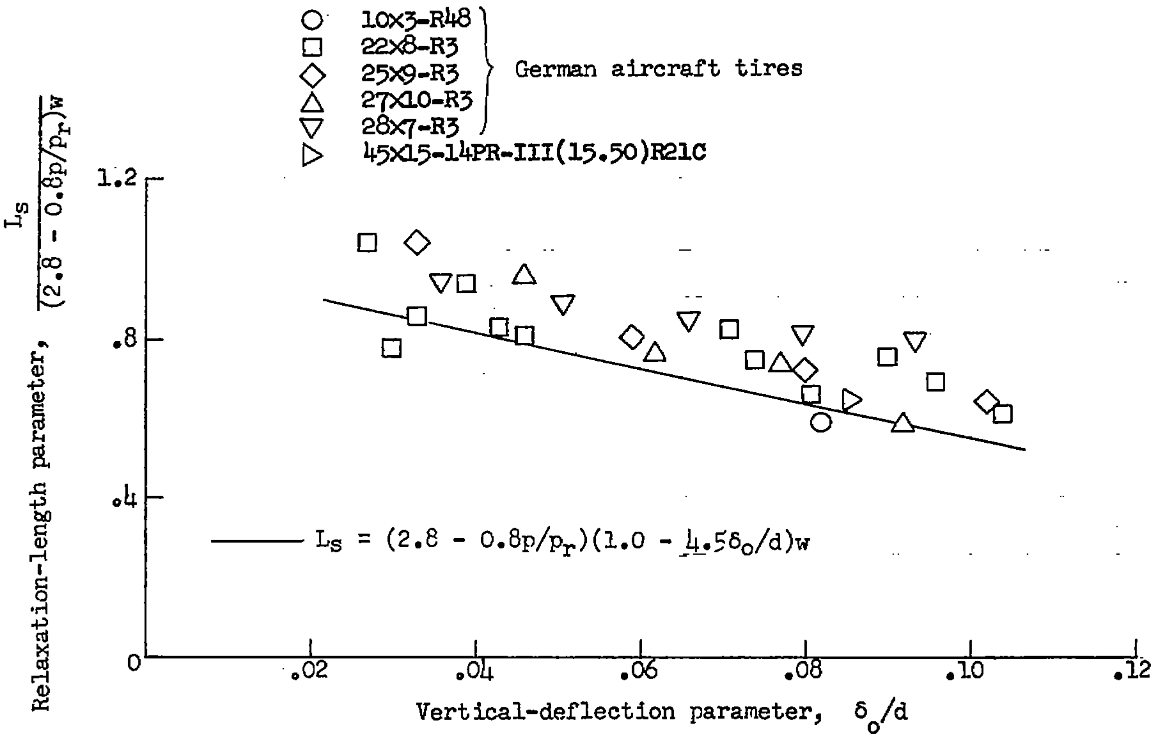

(b) Type III and German aircraft tires.

Figure 25.- Concluded.

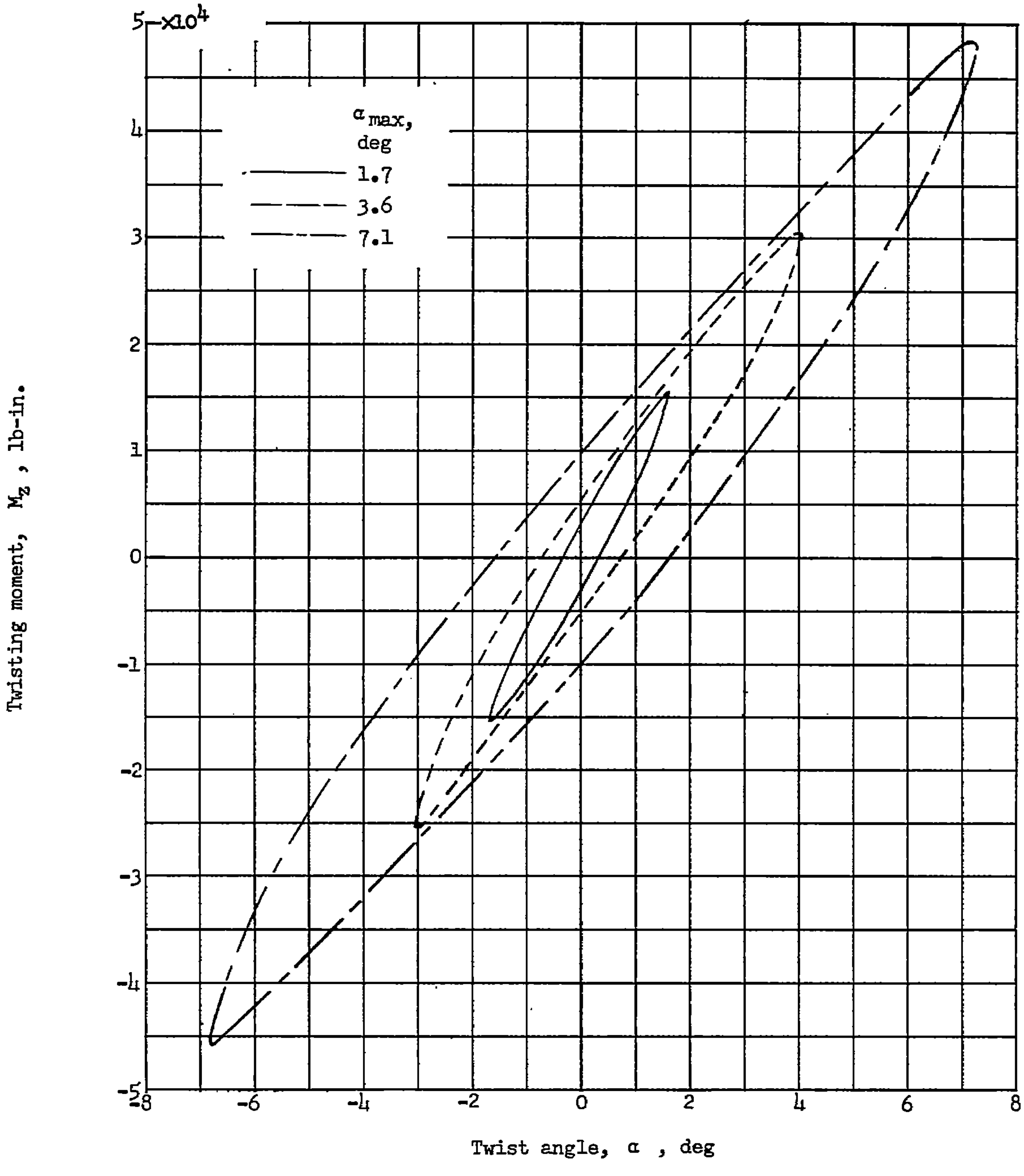

Figure 26.- Variation of twisting moment with twist angle for a 40×12-14PR-VII-R24-B tire for several different amplitudes. $p/p_r = 1.5$; $\delta_o/d = 0.10$.

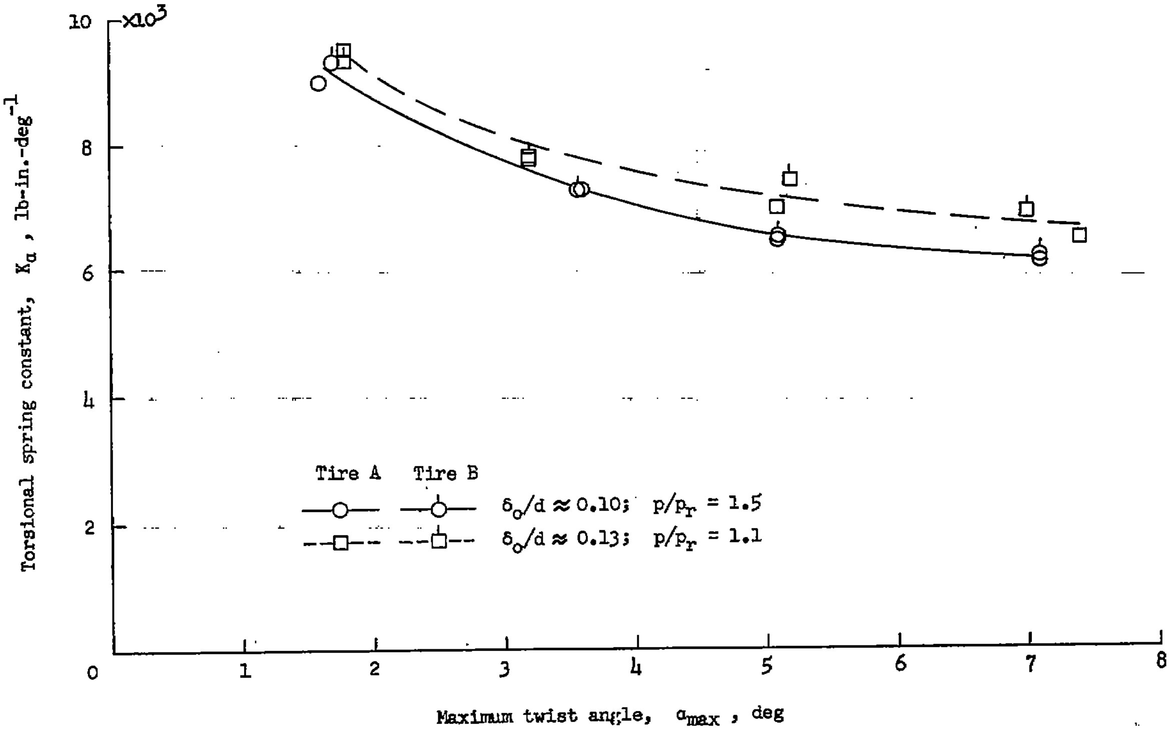

Figure 27.- Variation of torsional spring constant with amplitude of hysteresis loop for a pair of 40×12-14PR-VII-R24 tires.

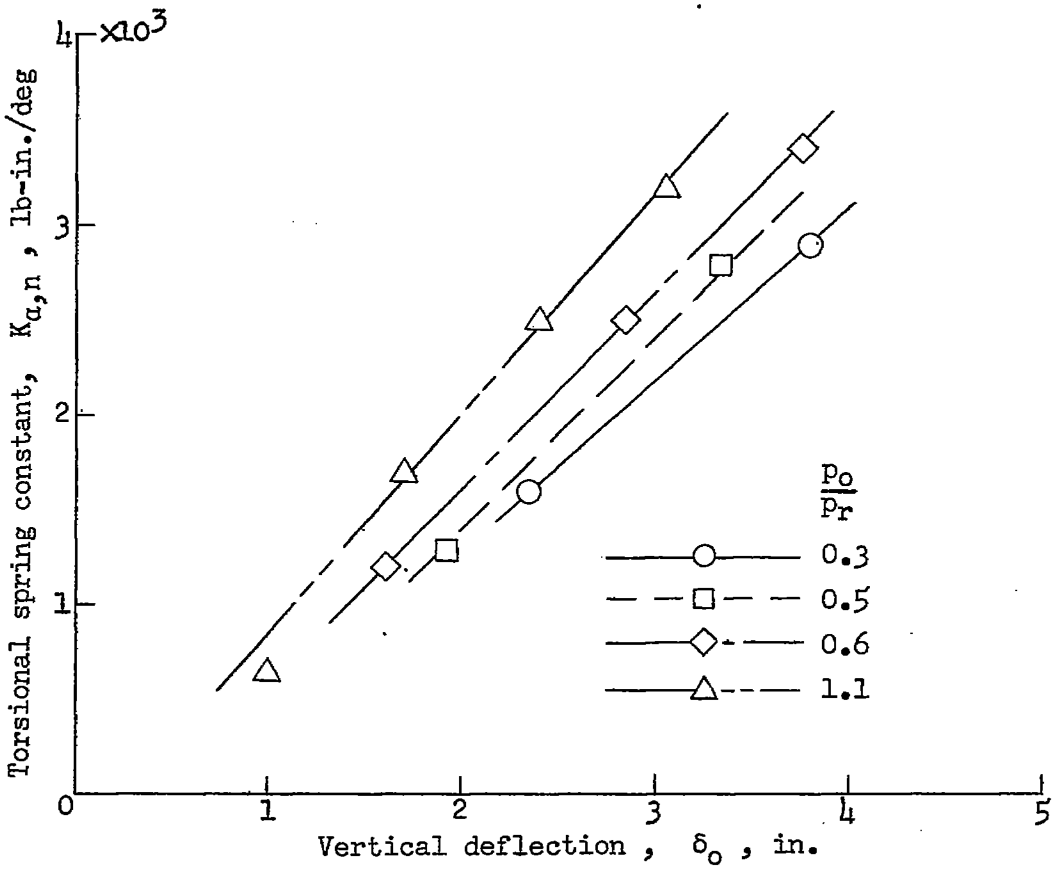

Figure 28.- Experimental variation of static torsional spring constant with vertical deflection and inflation pressure for a 28×9-10PR-I(27-inch)R21-E2 tire.

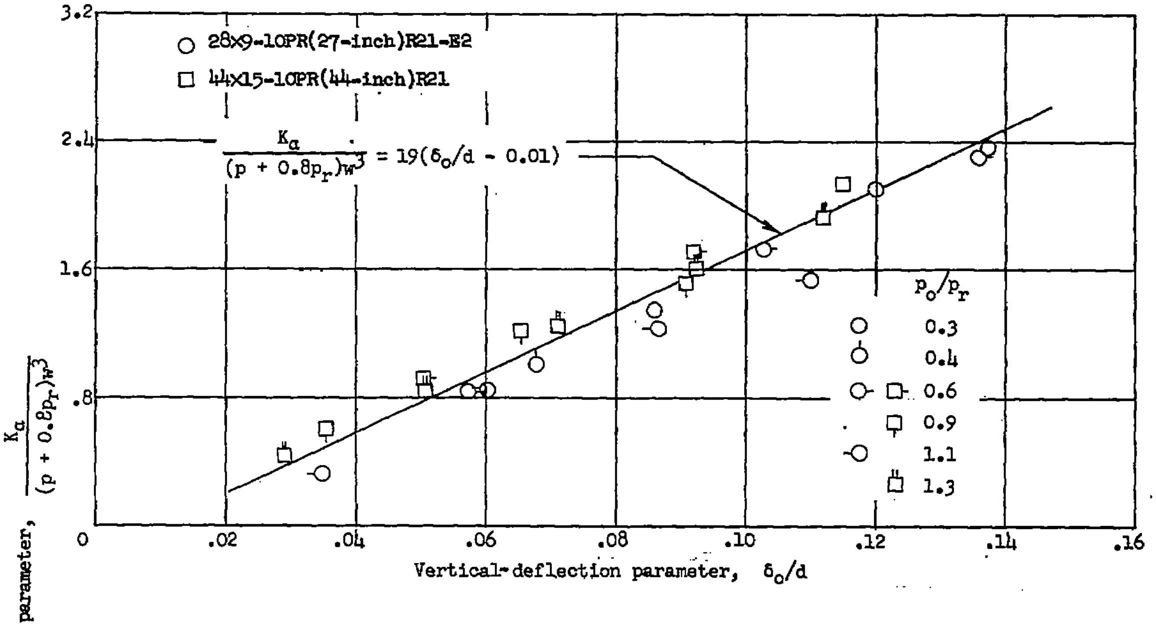

(a) Type I tires.

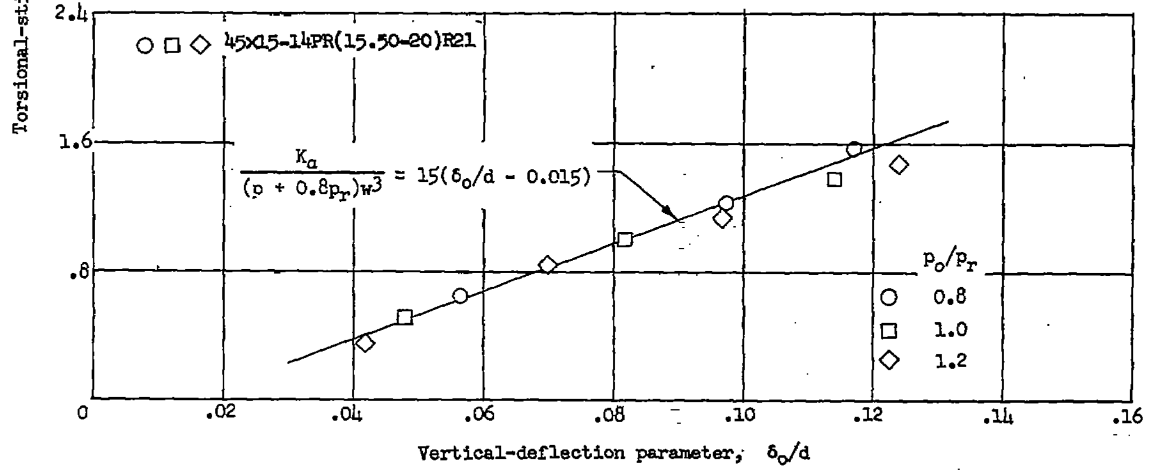

(b) Type III tire.

Figure 29.- Variation of static torsional stiffness parameter with vertical deflection for several aircraft tires.

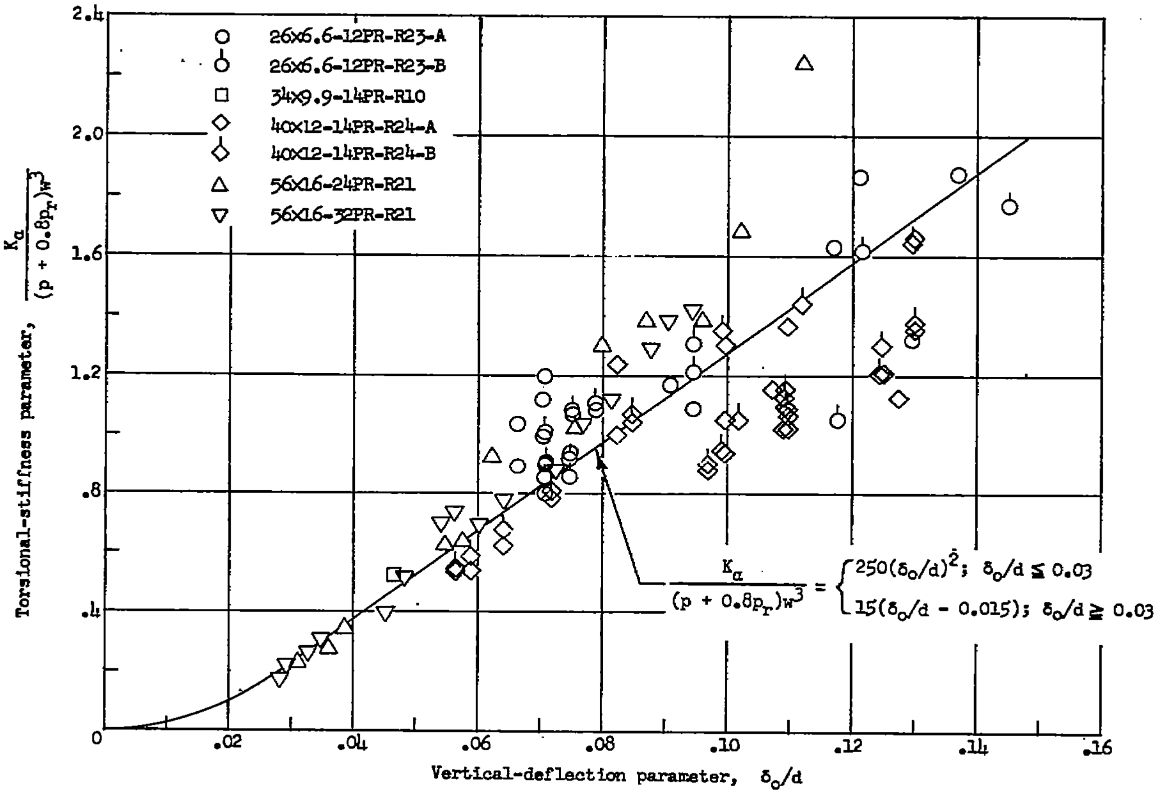

(c) Type VII tires.

Figure 29.- Continued.

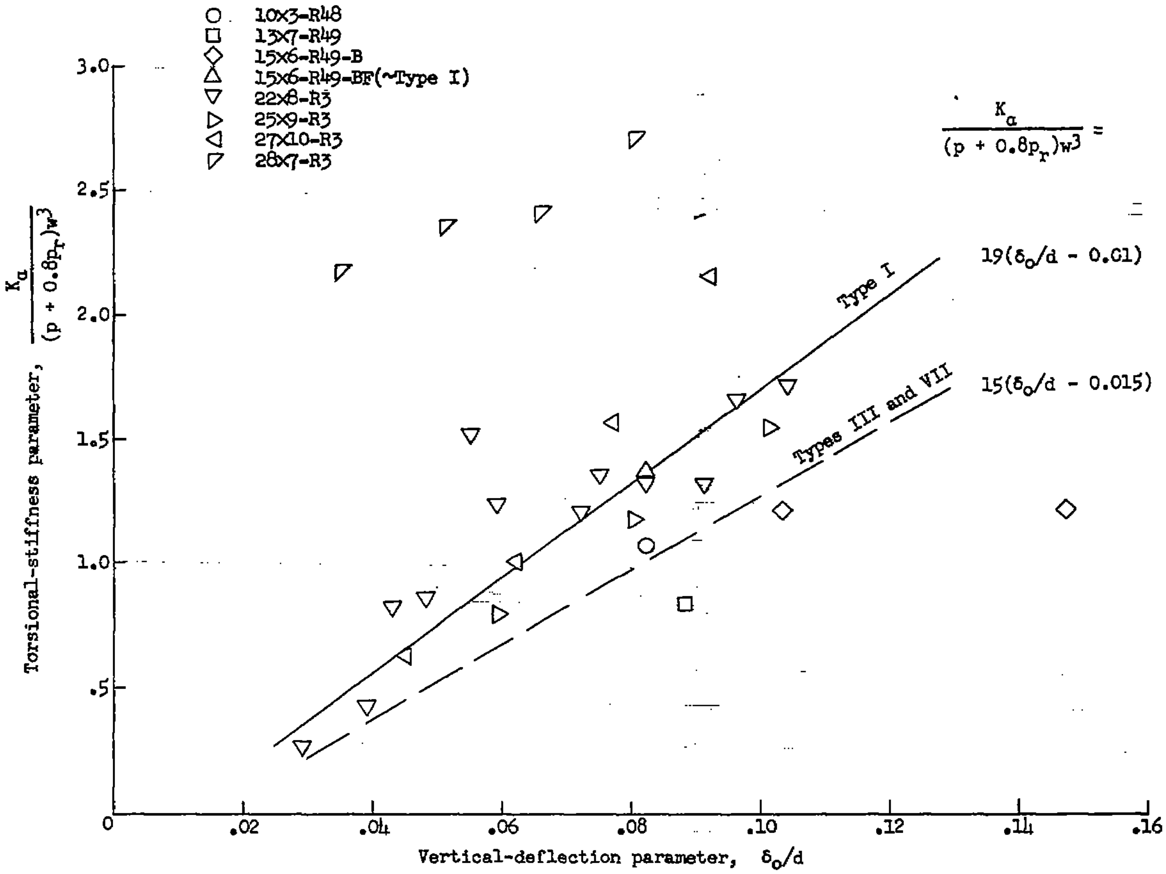

(d) German tires.

Figure 29.- Concluded.

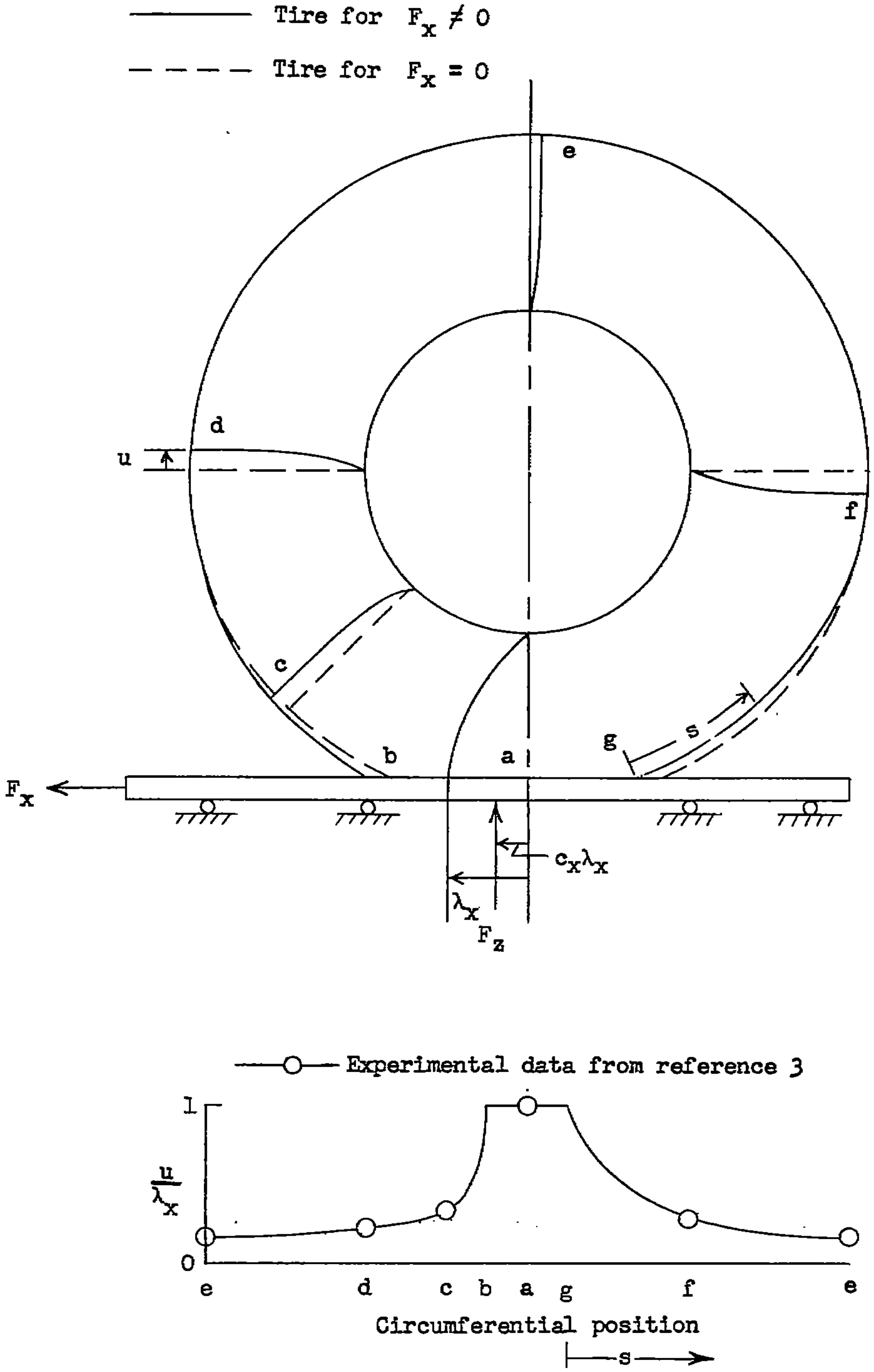

Figure 30.- Sketch illustrating tire distortion for combined vertical and fore-and-aft loading.

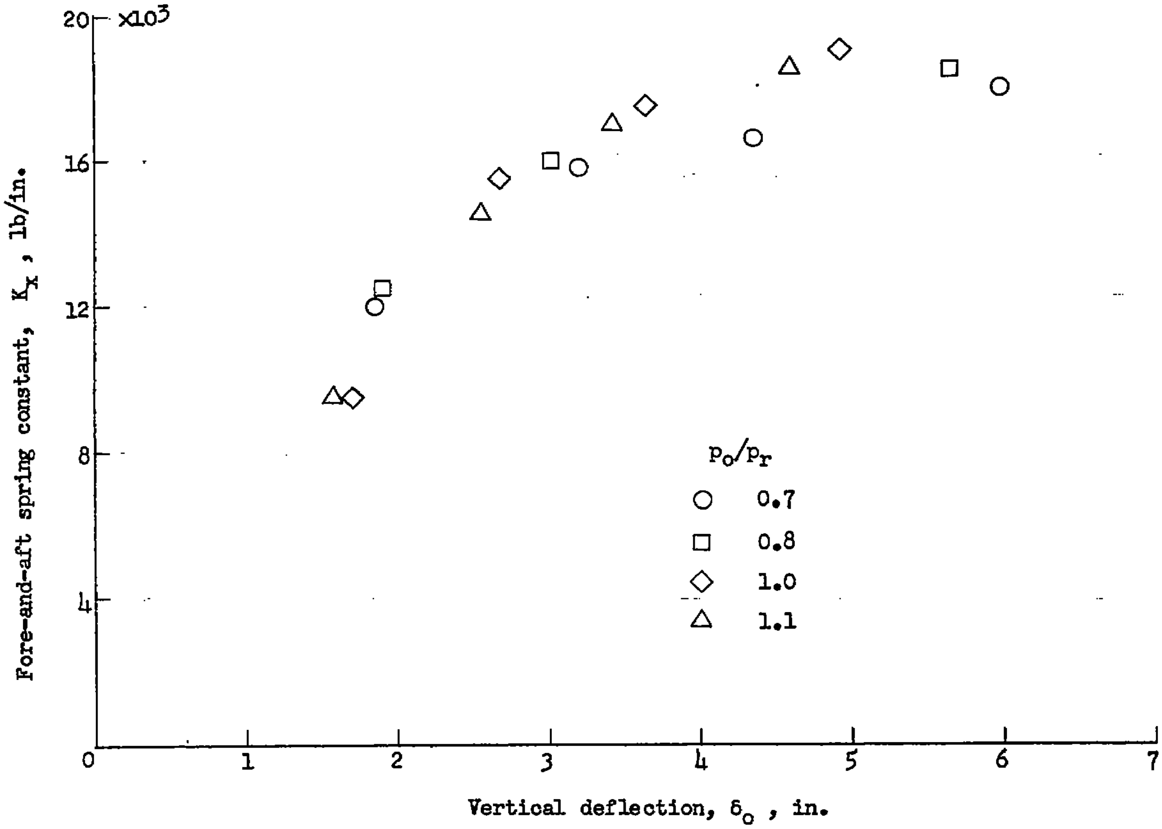

Figure 31.- Experimental variation of fore-and-aft spring constant with vertical deflection and inflation pressure for a 56x16-32PR-VII tire. (Data from ref. 21.)

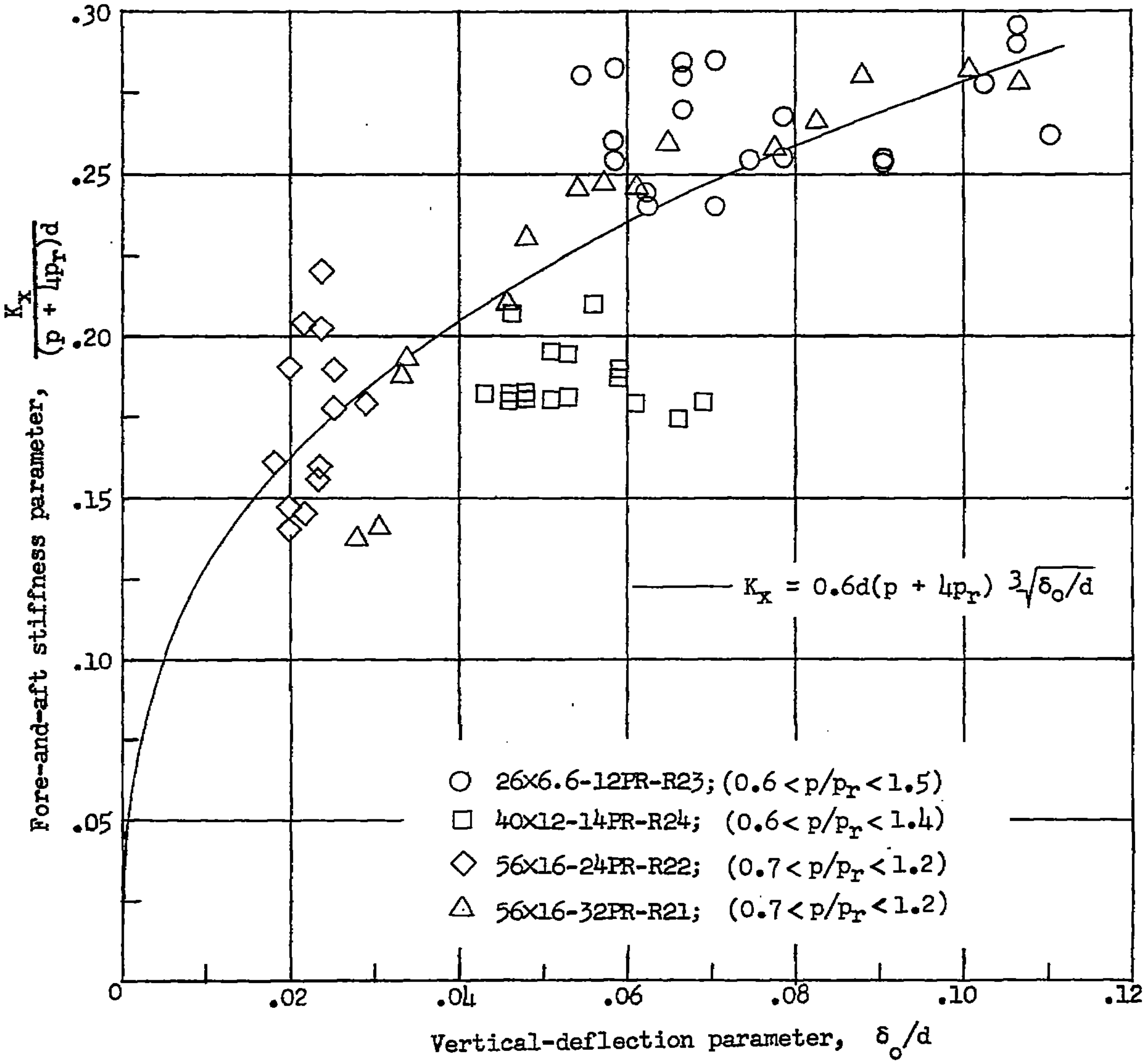

(a) Static data for type VII tires.

Figure 32.- Experimental variation of fore-and-aft stiffness parameter with vertical-deflection parameter for several tires.

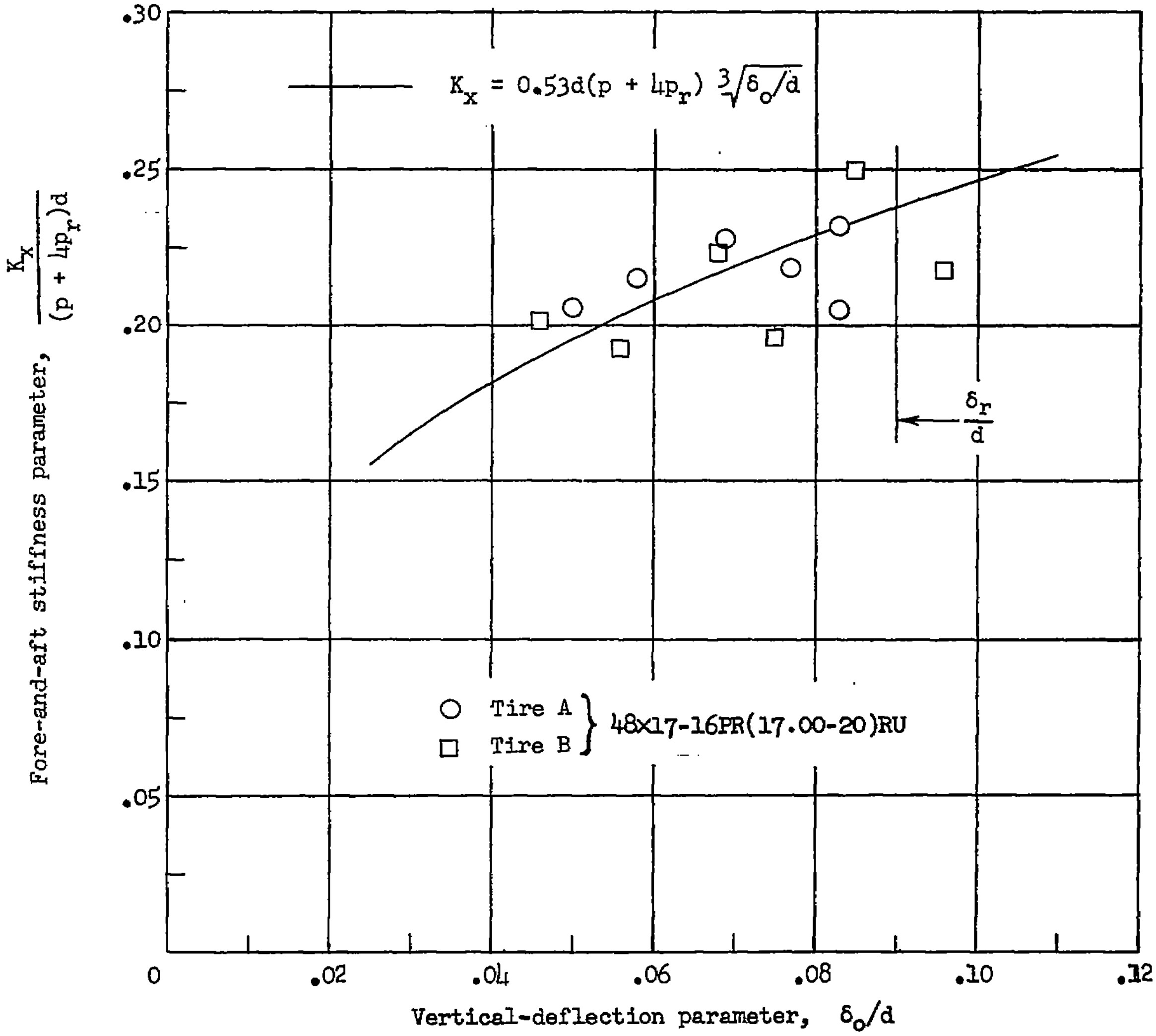

(b) Static data for type III tires.

Figure 32.- Continued.

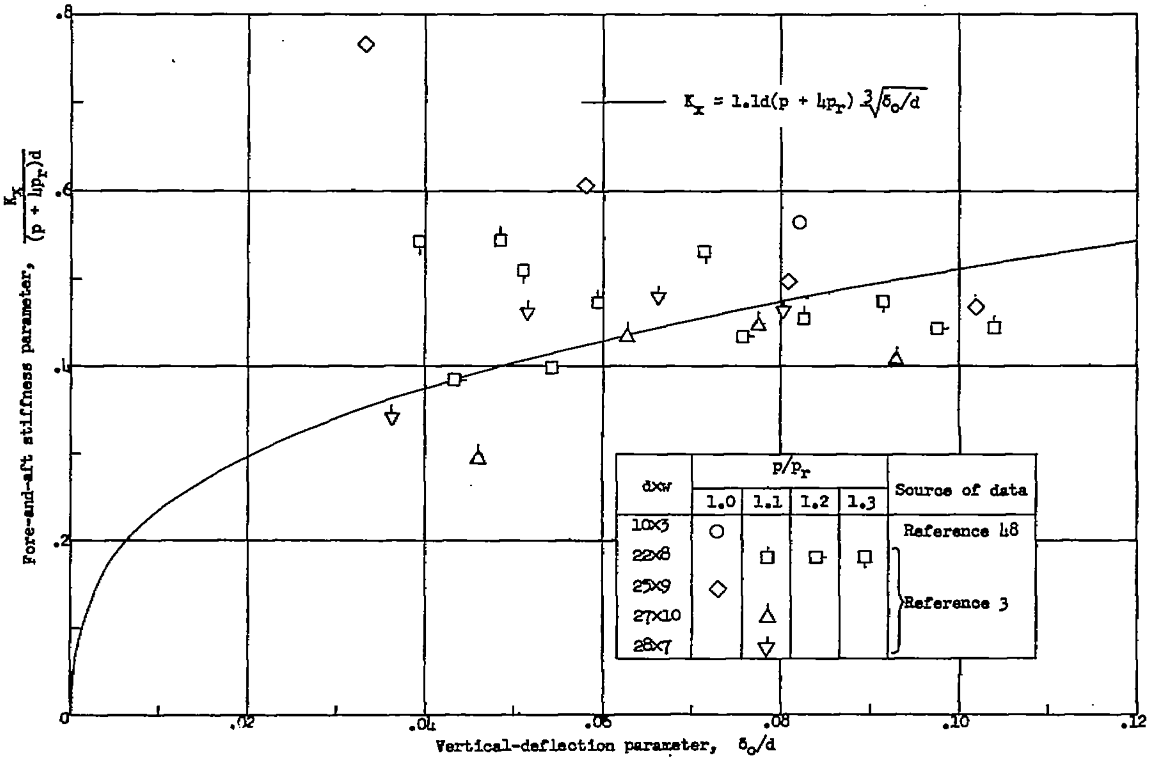

(c) Static data for German aircraft tires.

Figure 32.- Continued.

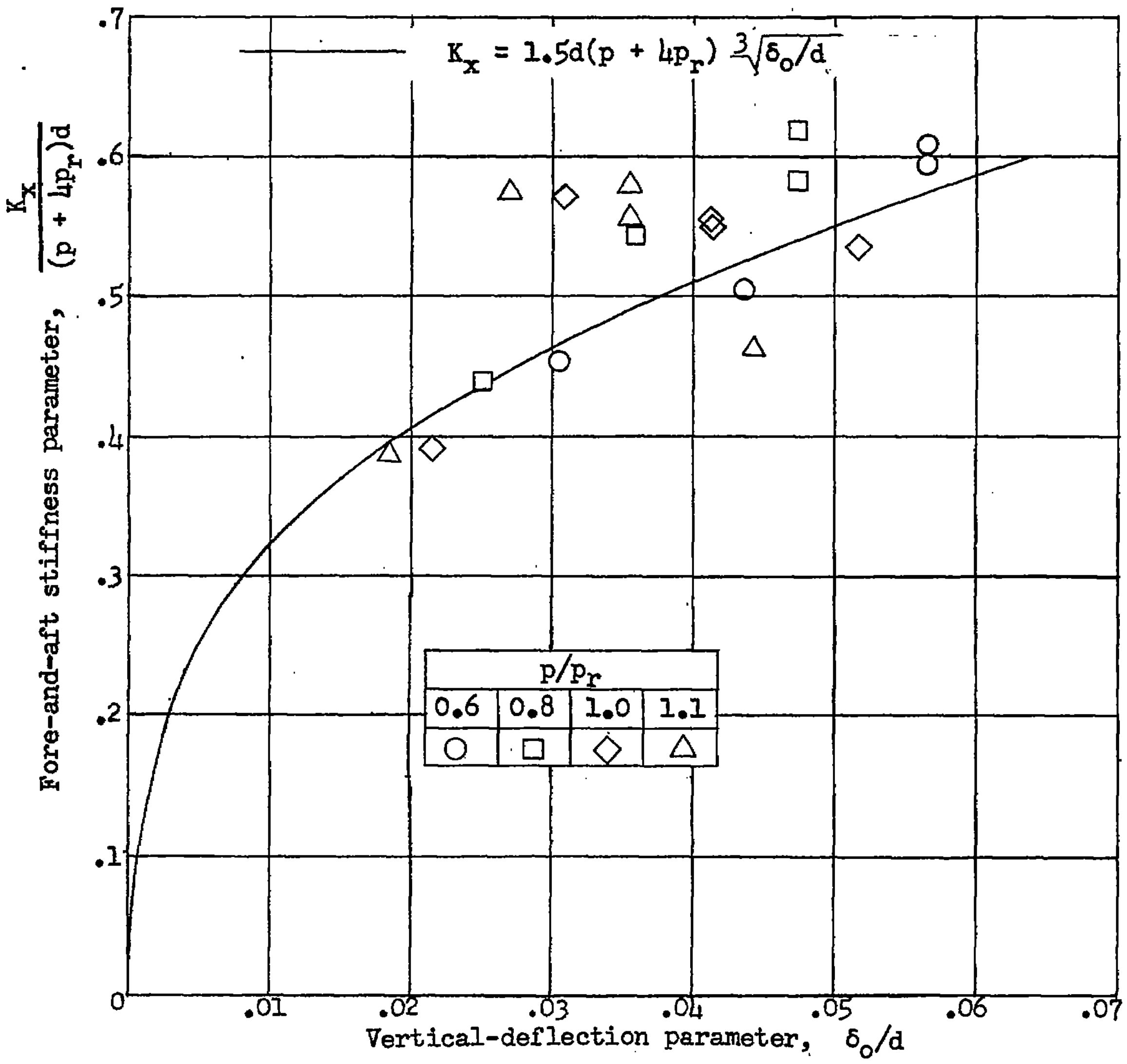

(d) Vibration data (from ref. 25) for 26x8 tire.

Figure 32.- Concluded.

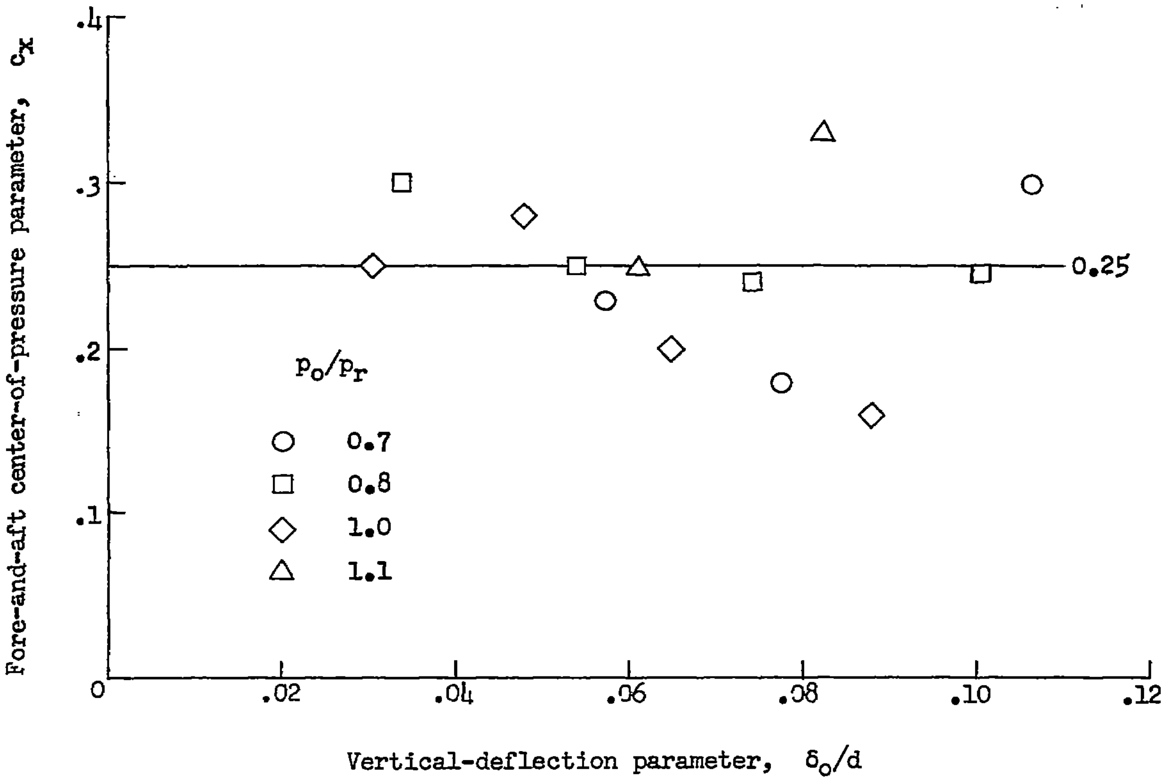

Figure 33.- Experimental variation of vertical-force center-of-pressure parameter with vertical-deflection parameter and inflation pressure for fore-and-aft loading of a 56x16-32PR-VII tire. (Data from ref. 21.)

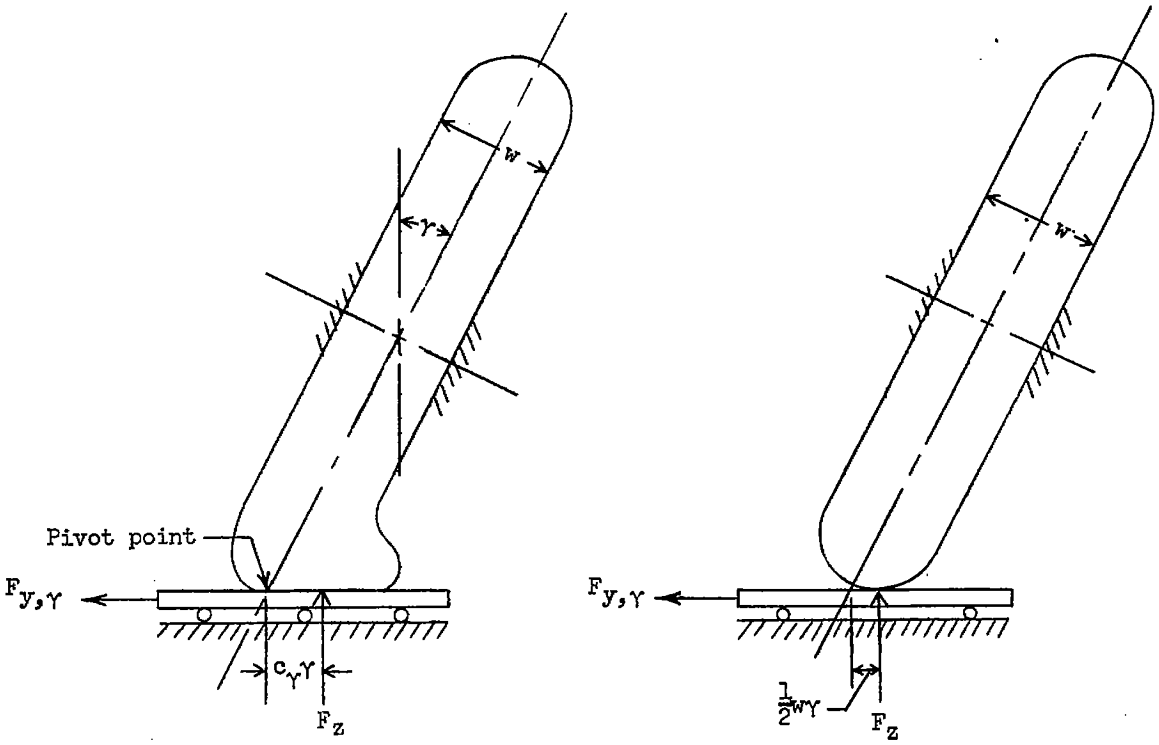

(a) Elastic tire. (b) Rigid tire.

Figure 34.- Sketch of standing tire under combined vertical force and tilt.

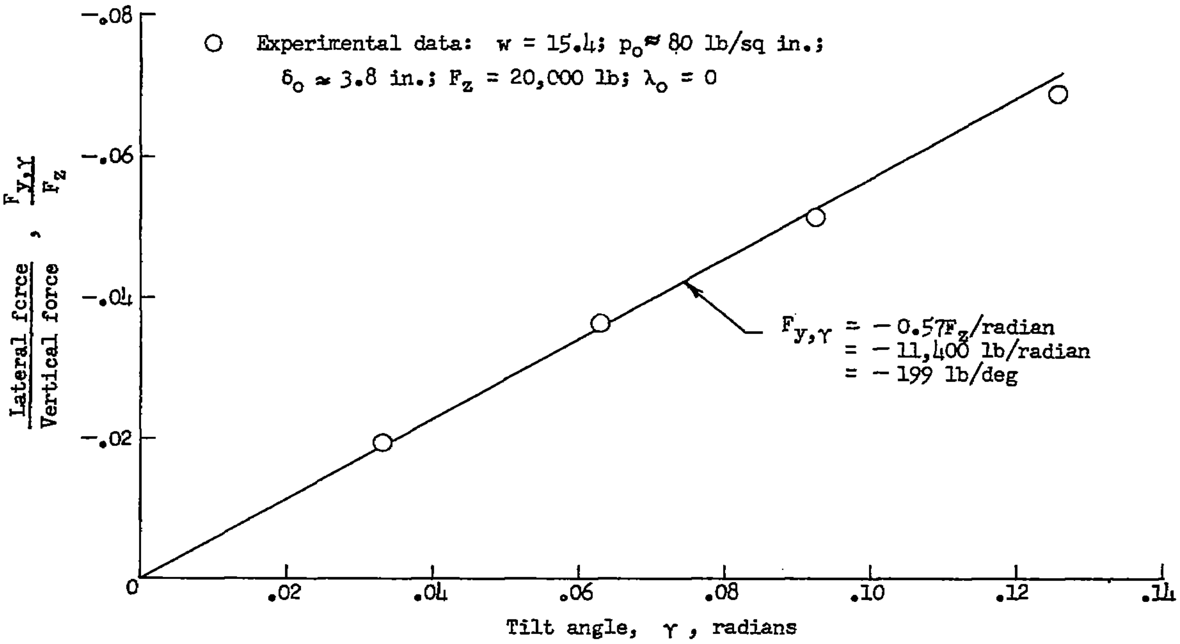

Figure 35.- Variation of lateral force with tilt angle for a standing tire. (Unpublished experimental data for 45x15-14PR-III(15.50-20) tire of ref. 21.)

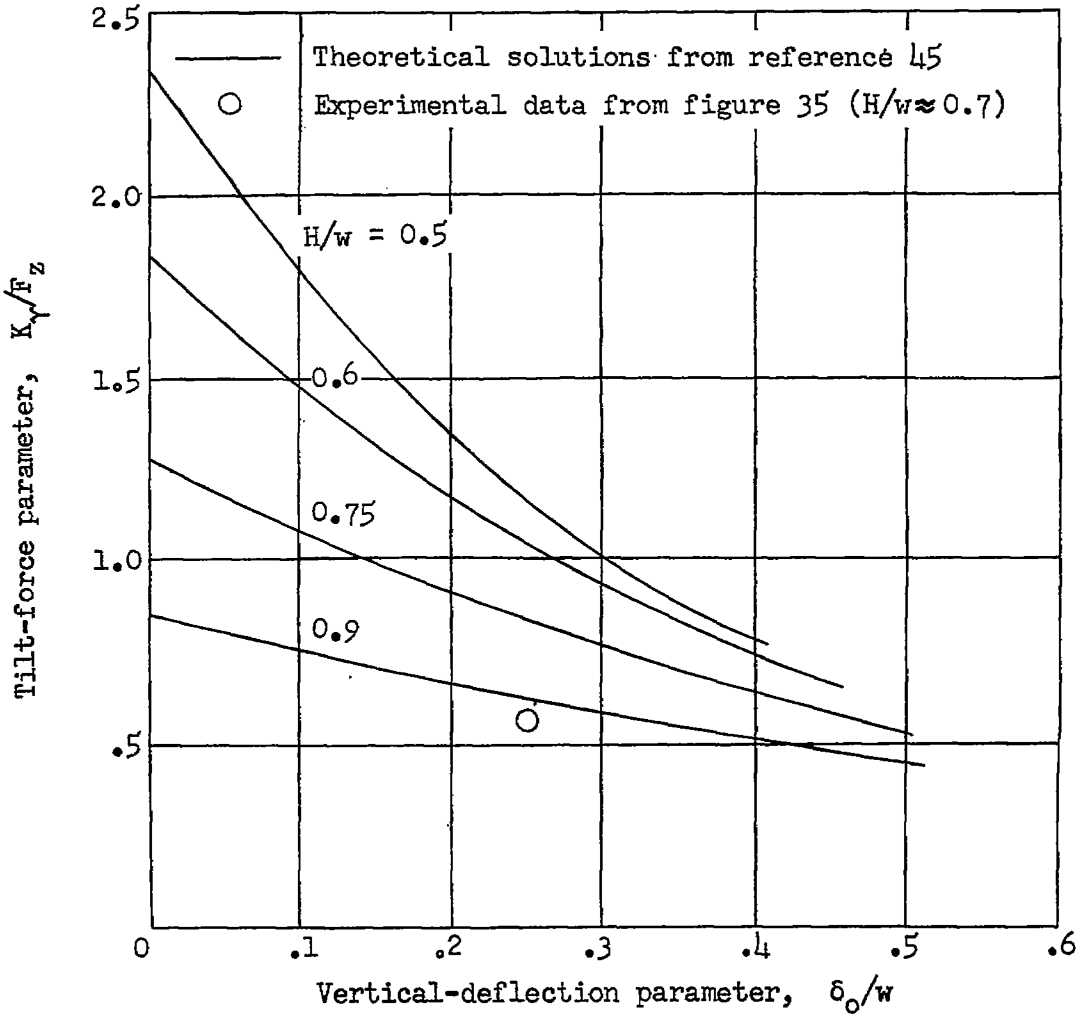

Figure 36.- Theoretical variation of static tilt-force parameter K_γ/F_z and comparison with experimental data.

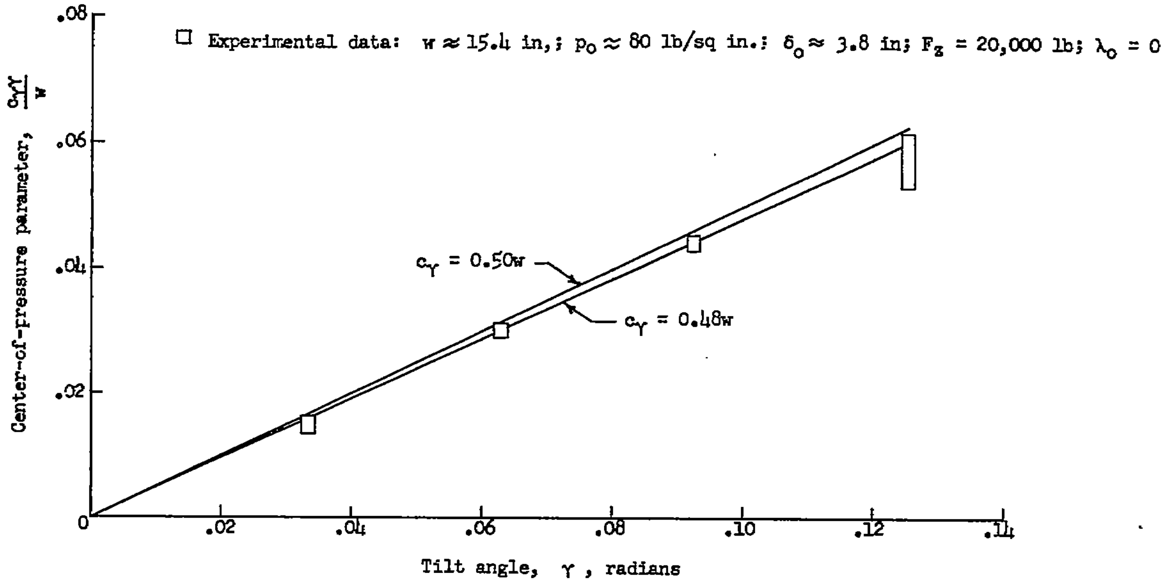

Figure 37.- Variation of vertical-force center-of-pressure parameter with tilt angle for a standing tire. (Unpublished experimental data for 45x15-14PR-III(15.50-20) tire of ref. 21.) Vertical height of test symbols indicates probable error for respective test points.

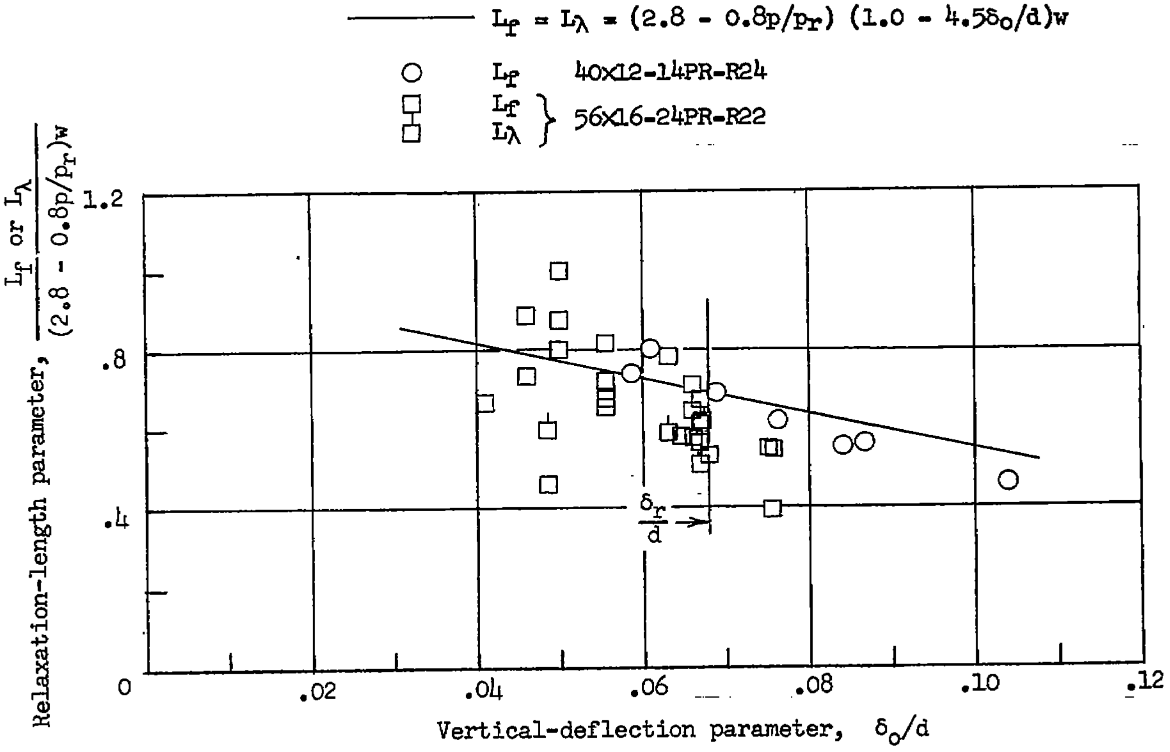

Figure 38.- Variation of unyawed-rolling relaxation-length parameters with vertical-deflection parameter for two pairs of type VII tires.

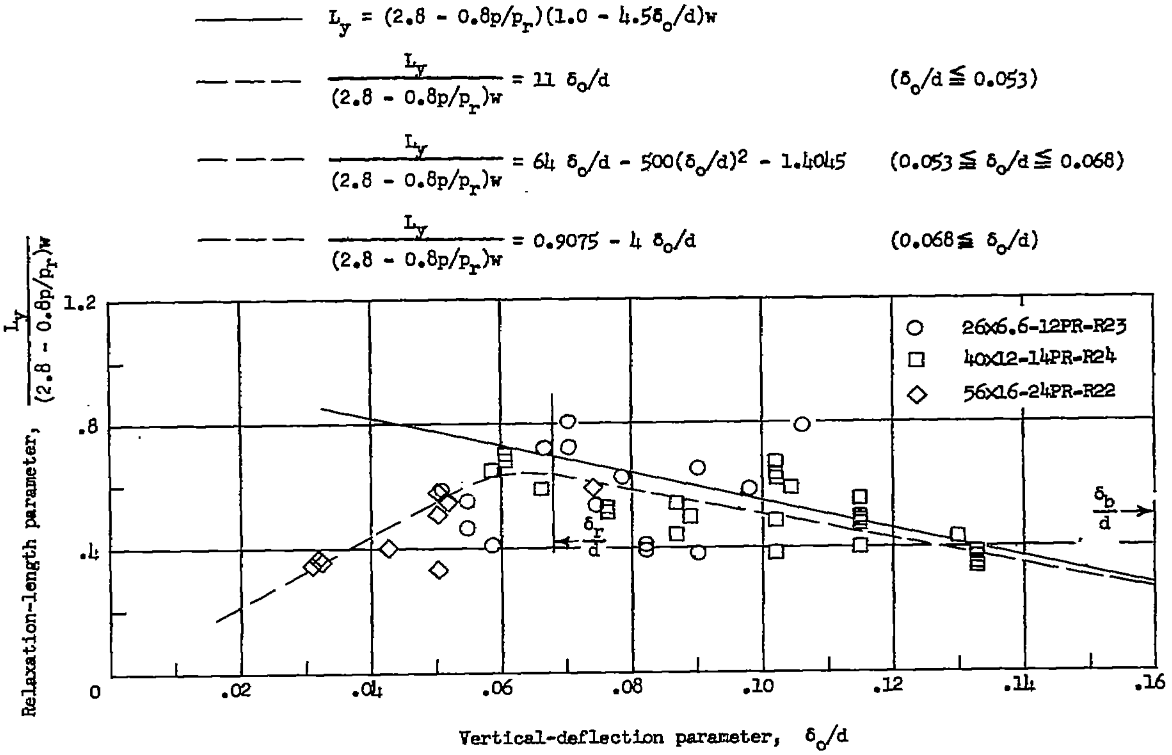

Figure 39.- Variation of yawed-rolling relaxation-length parameter with vertical-deflection parameter for three type VII tires.

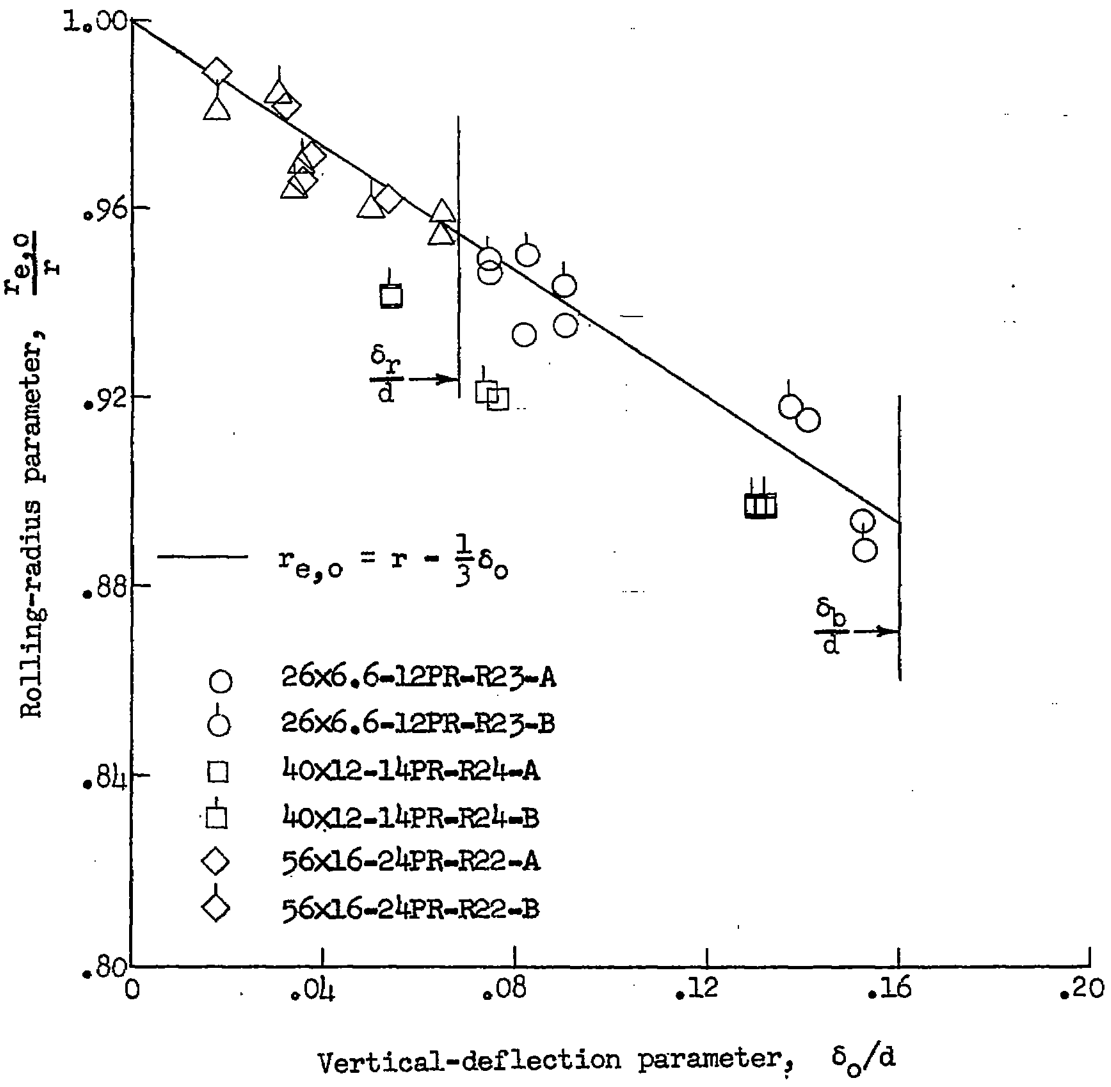

Figure 40.- Variation of rolling radius with vertical-deflection parameter for six type VII tires at very small or zero yaw angles.

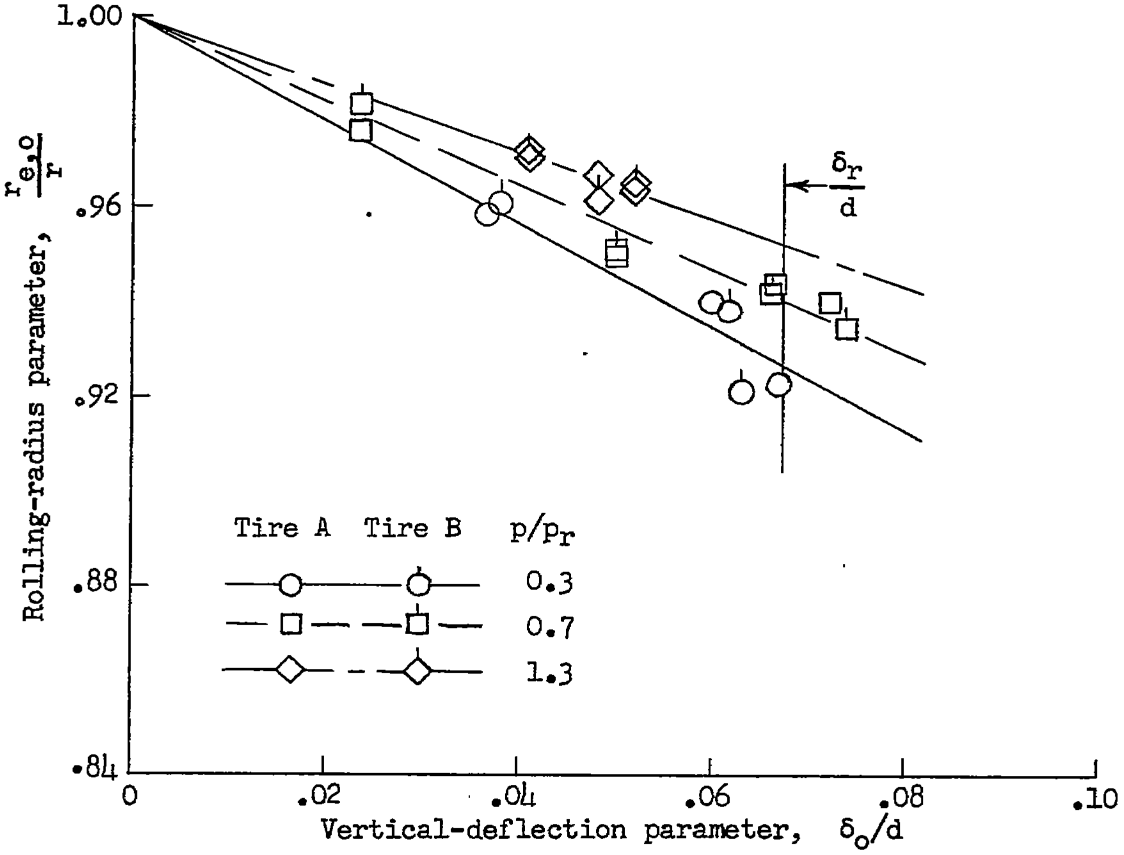

Figure 41.- Effects of inflation pressure on the variation of rolling radius with vertical-deflection parameter for two 56x16-24PR-VII-R22 tires.

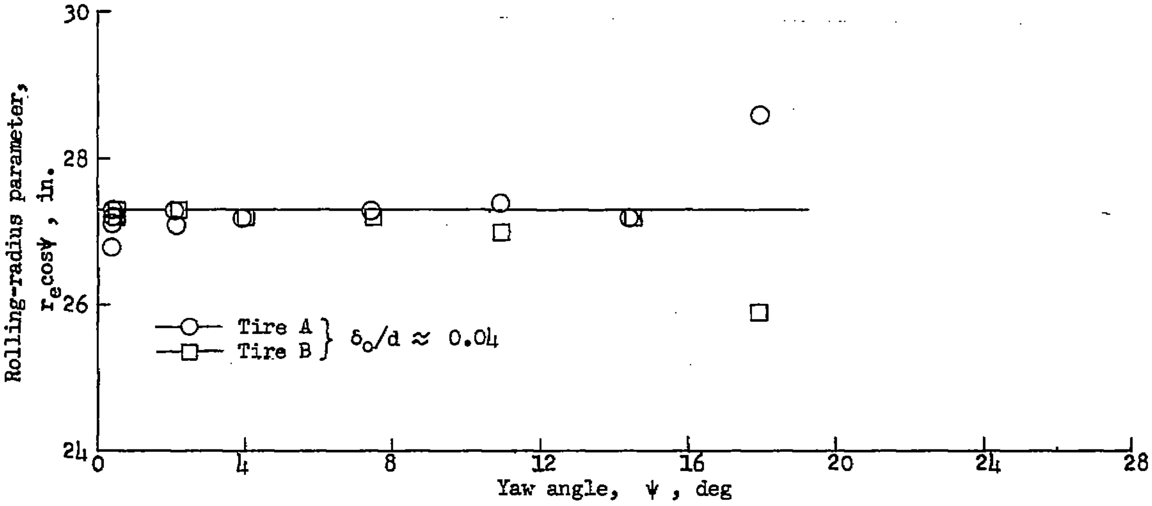

(a) 56x16-24PR-VII-R22 tires.

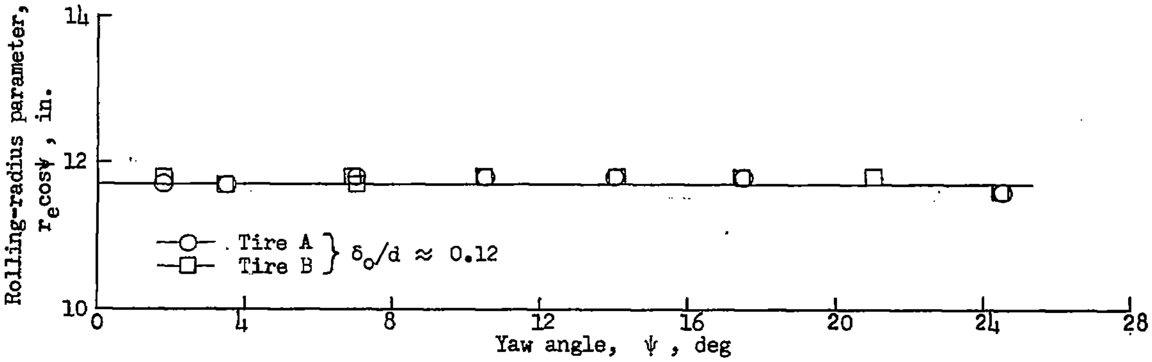

(b) 26x6.6-12PR-VII-R23 tires.

Figure 42.- Effects of yaw on rolling radius for two tires at different vertical-deflection—diameter ratios.

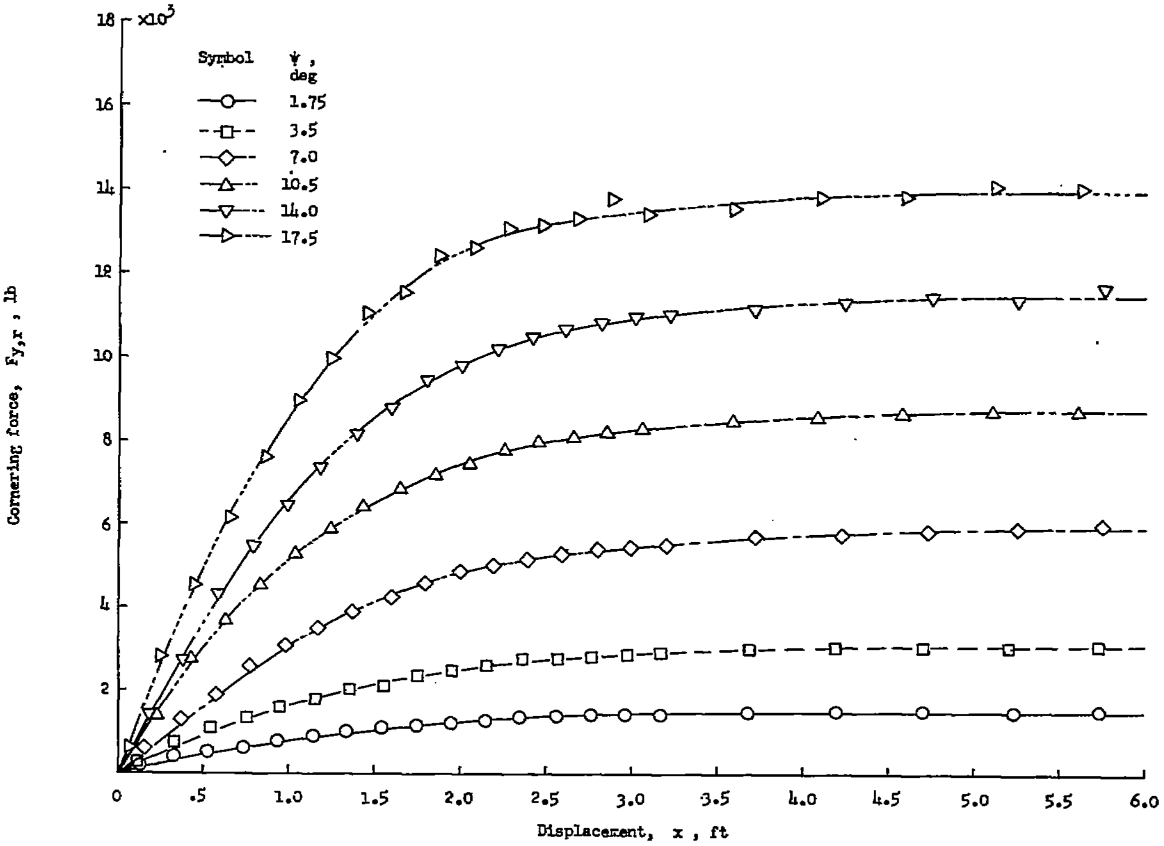

Figure 43.- Buildup of cornering force with distance rolled for a pair of 40×12-14PR-VII-R24 tires. $p/p_r = 1.5$; $\delta_o/d = 0.10$.

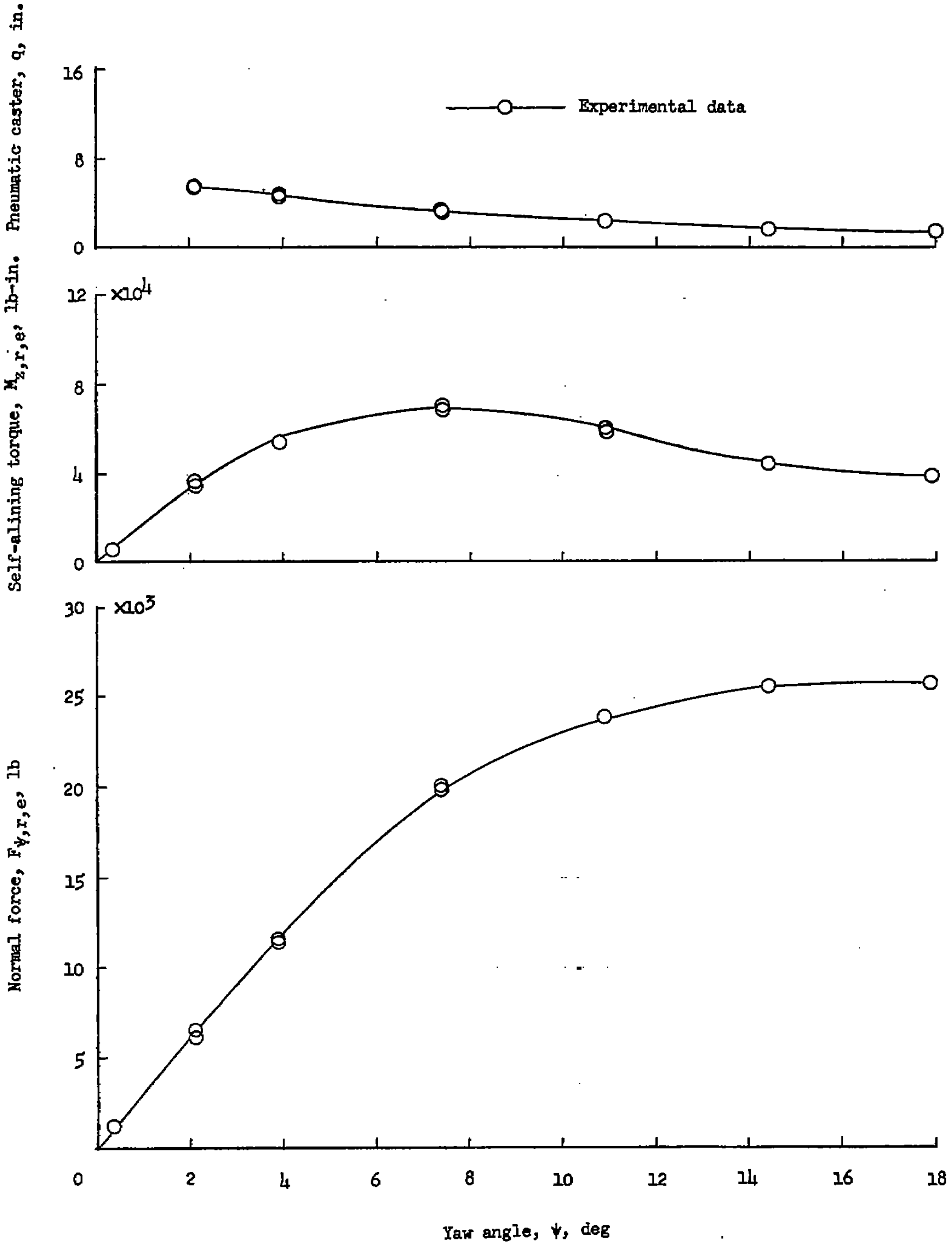

(a) 56x16-24PR-R22 tires. $p/p_r = 1.3$; $\delta_o/d = 0.05$; $F_z = 45{,}200$ pounds.

Figure 44.- Variation of normal force, self-alining torque, and pneumatic caster with yaw angle for two pairs of type VII tires.

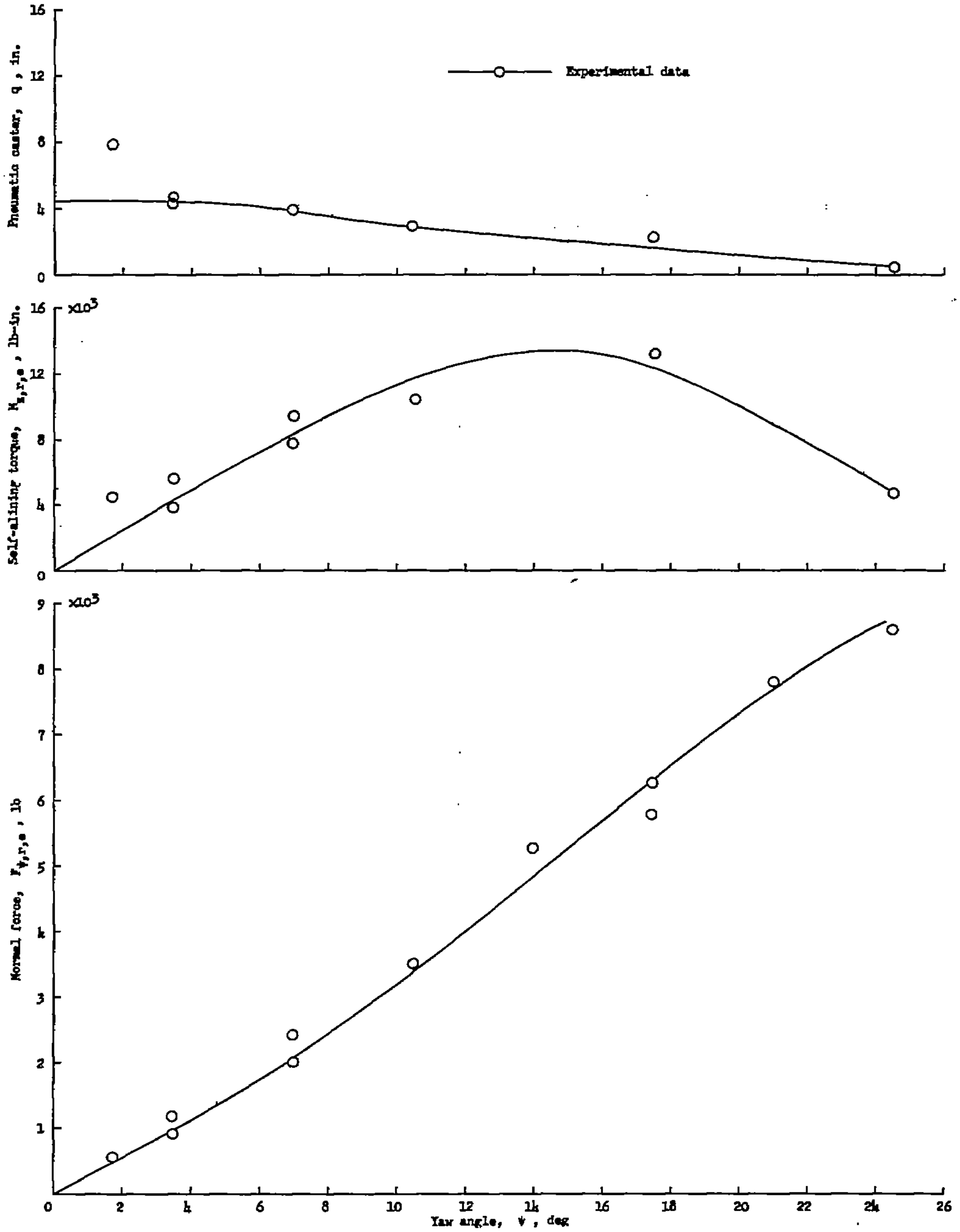

(b) 26x6.6-12PR-R23 tires. $p/p_r = 1.3$; $\delta_o/d = 0.13$; $F_z = 17,100$ pounds.

Figure 44.- Concluded.

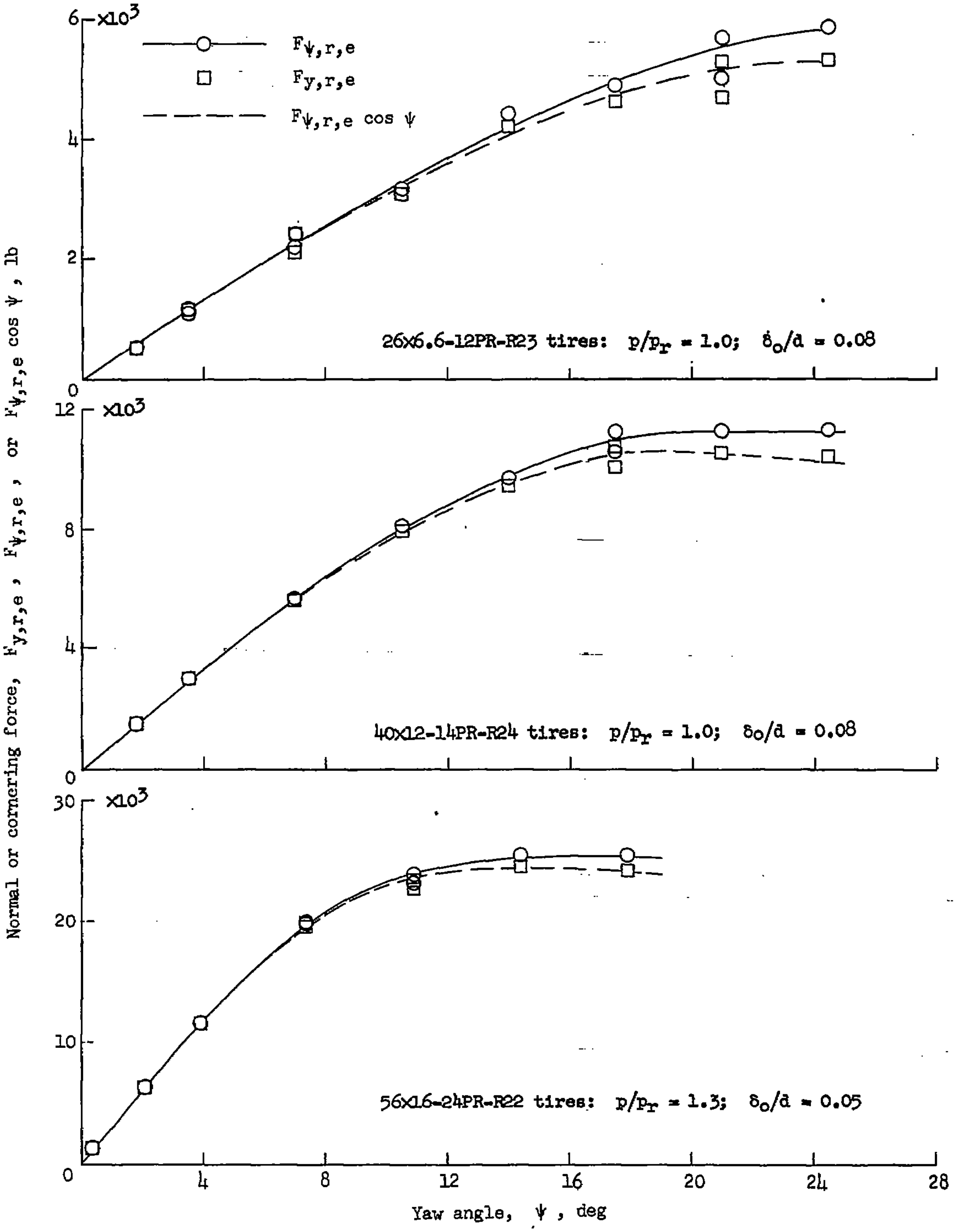

Figure 45.- Comparison of normal and cornering forces for yawed rolling of several type VII tires.

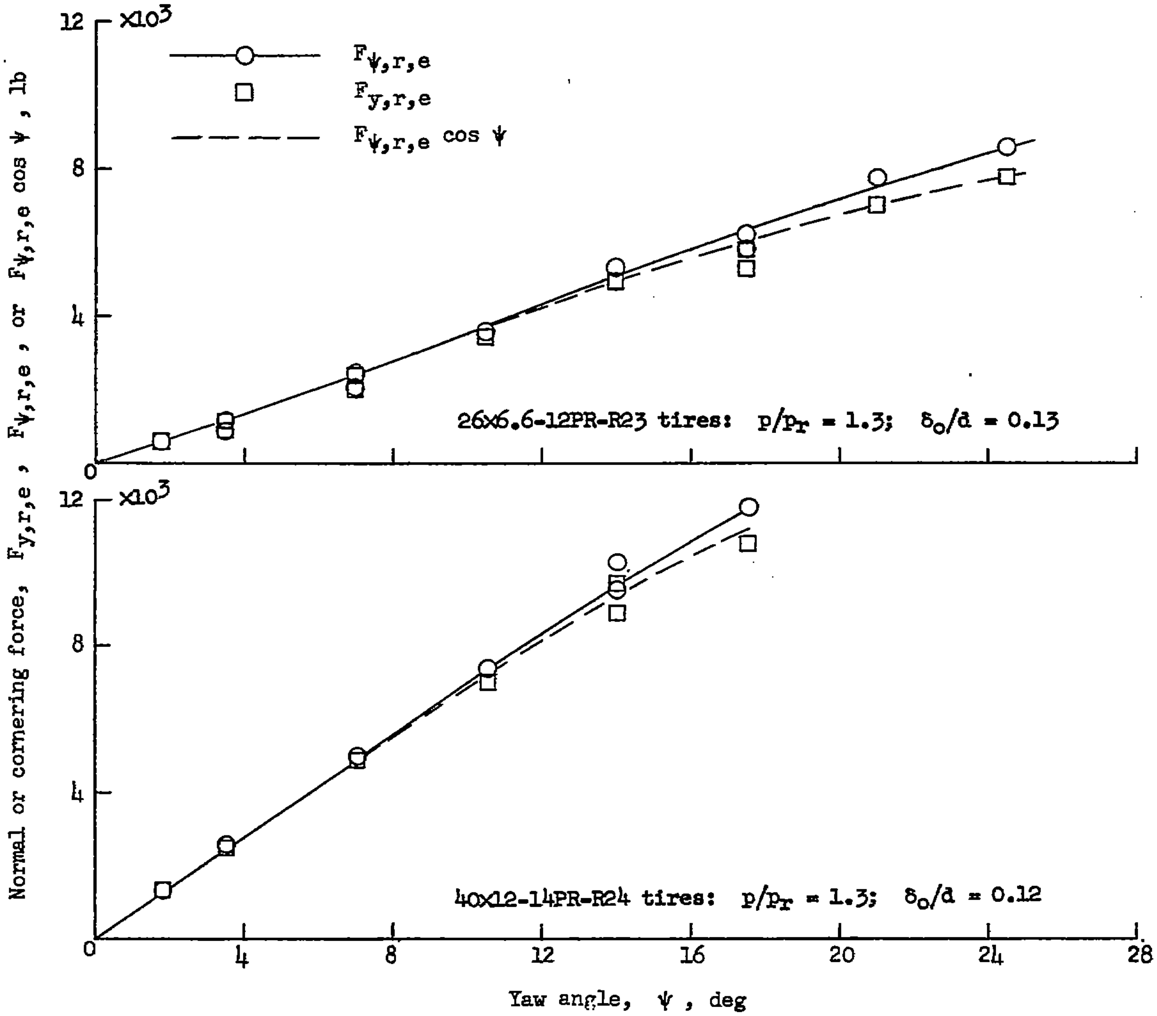

Figure 45.- Concluded.

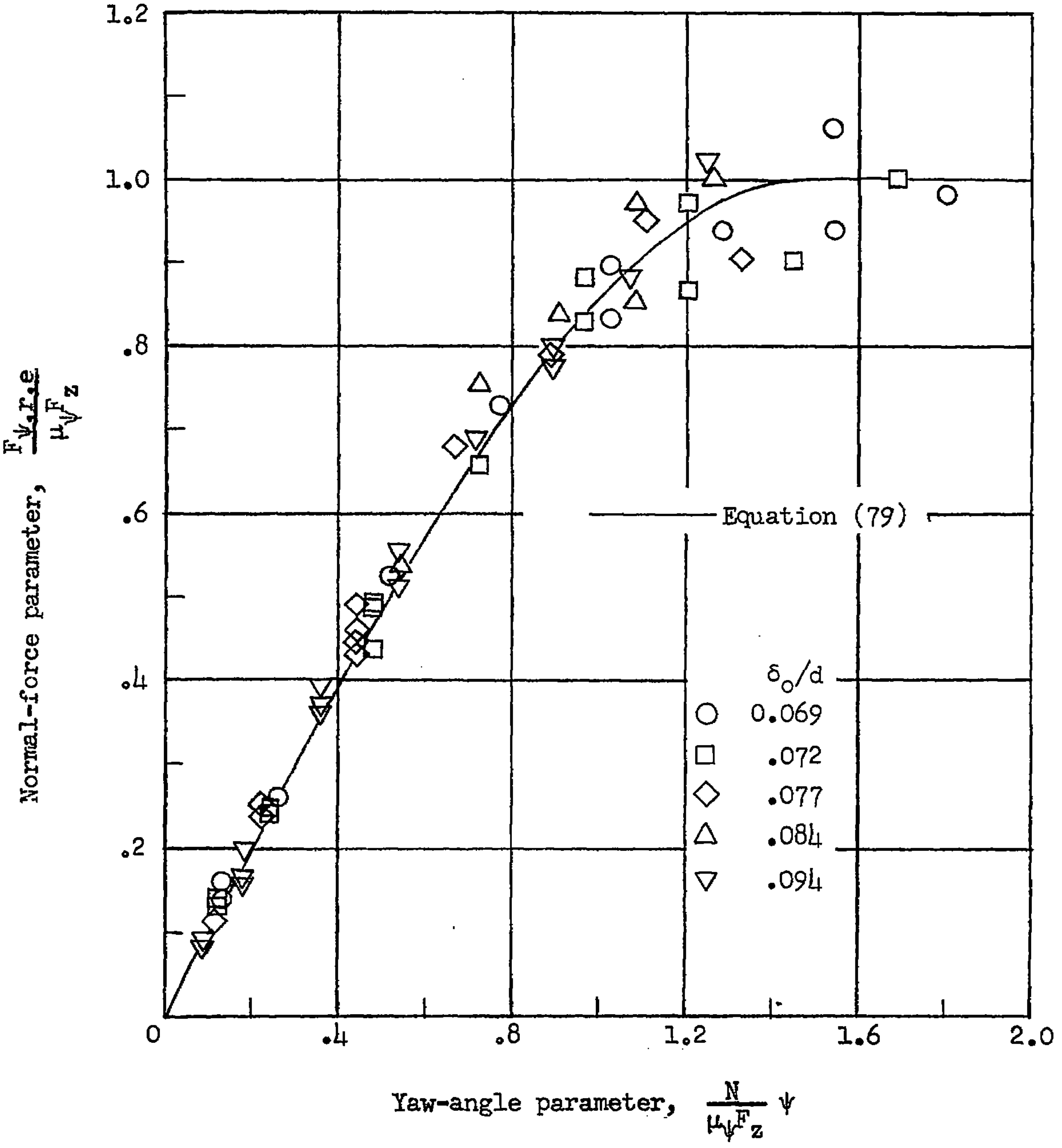

(a) 26x6.6-12PR-VII-R23 tires.

Figure 46.- Variations of normal-force parameter with yaw-angle parameter for steady-state yawed rolling of type VII tires.

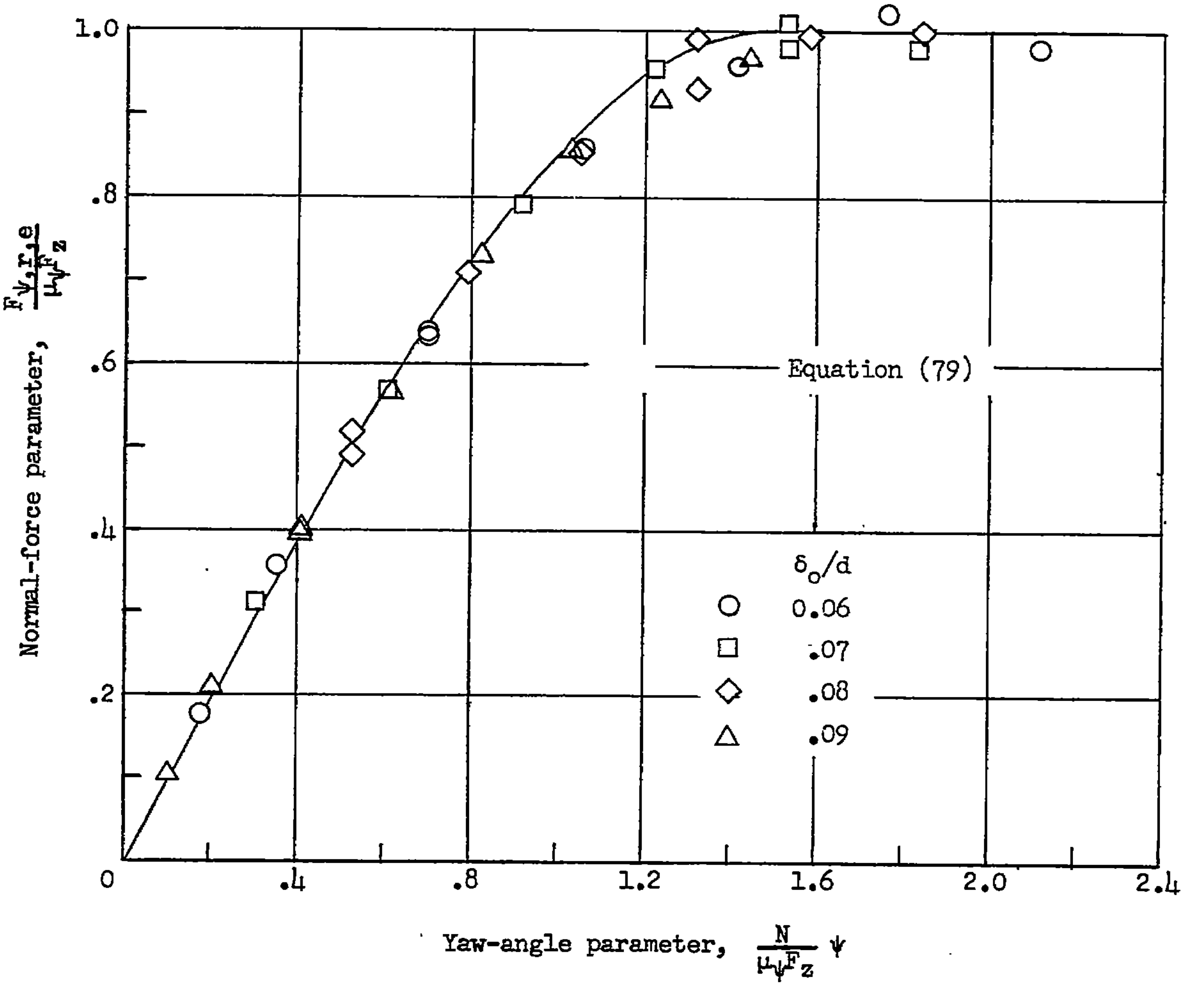

(b) 40x12-14PR-VII-R24 tires.

Figure 46.- Continued.

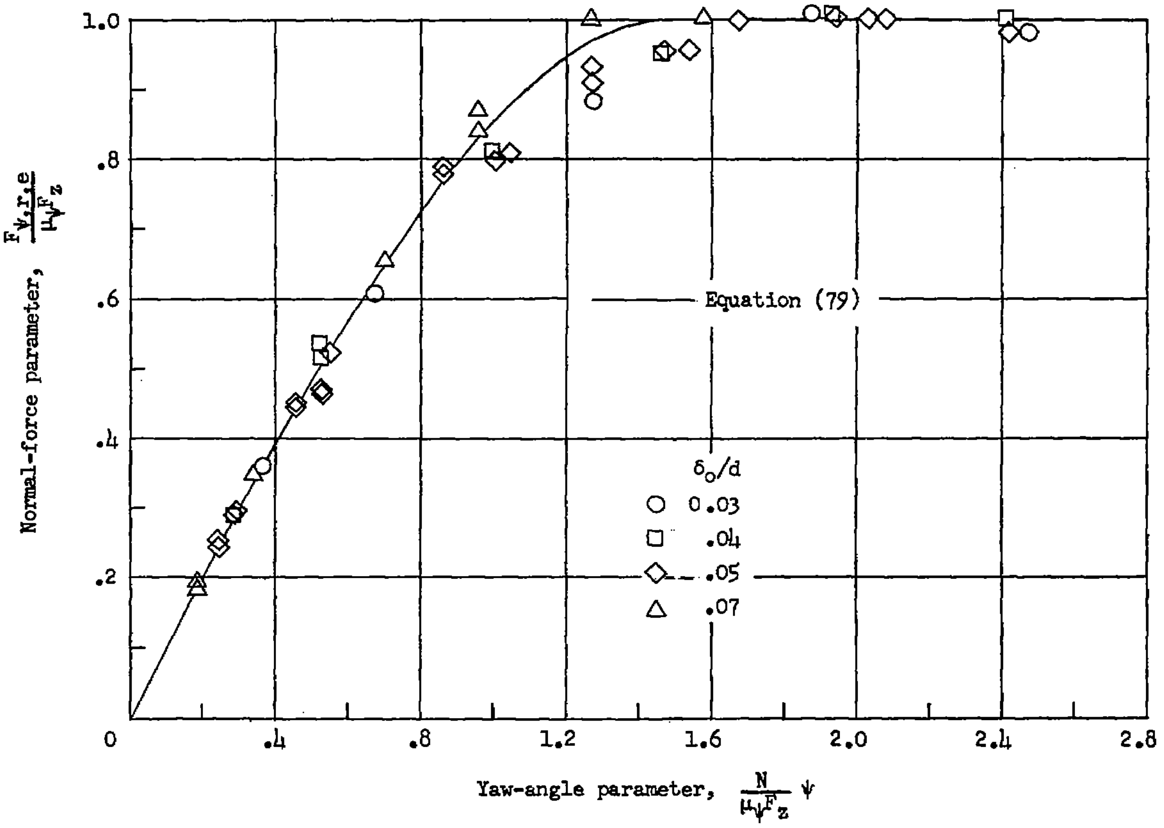

(c) 56x16-24PR-VII-R22 tires.

Figure 46.- Concluded.

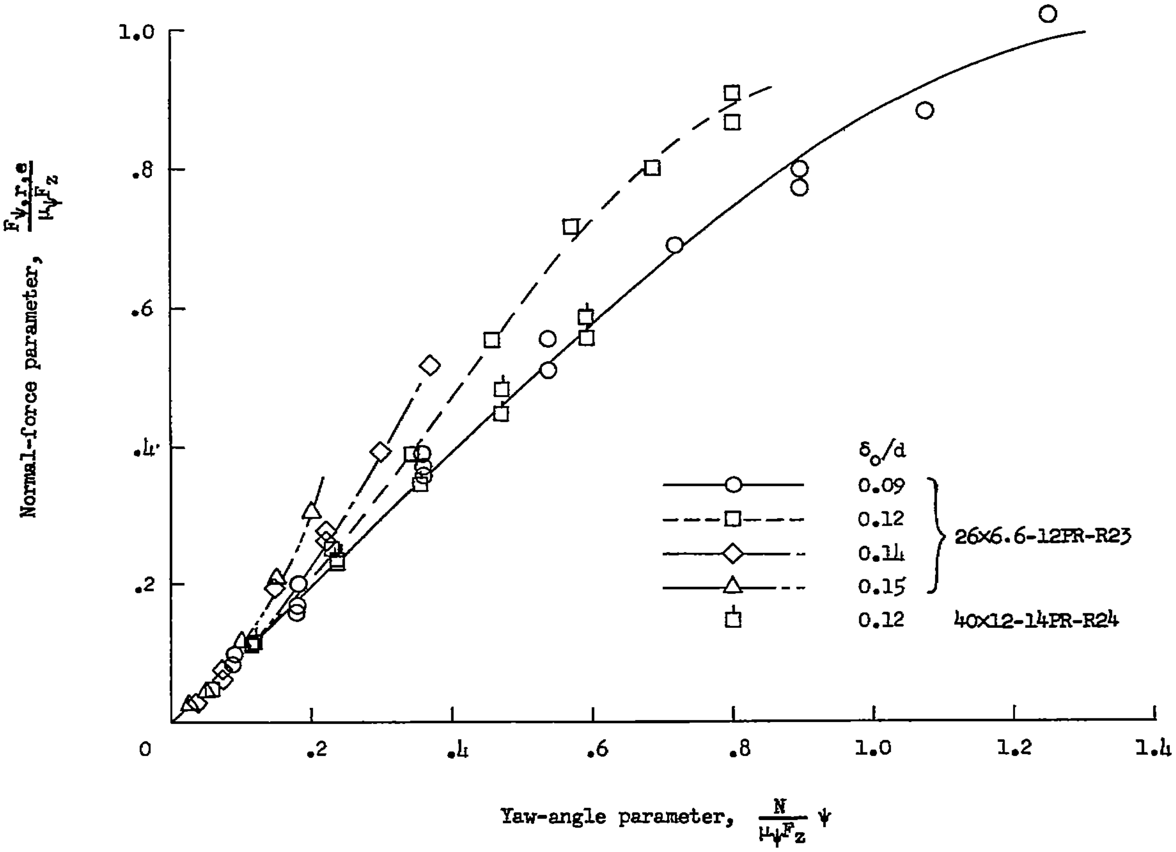

Figure 47.- Variation of steady-state normal force with yaw angle for large vertical deflections.

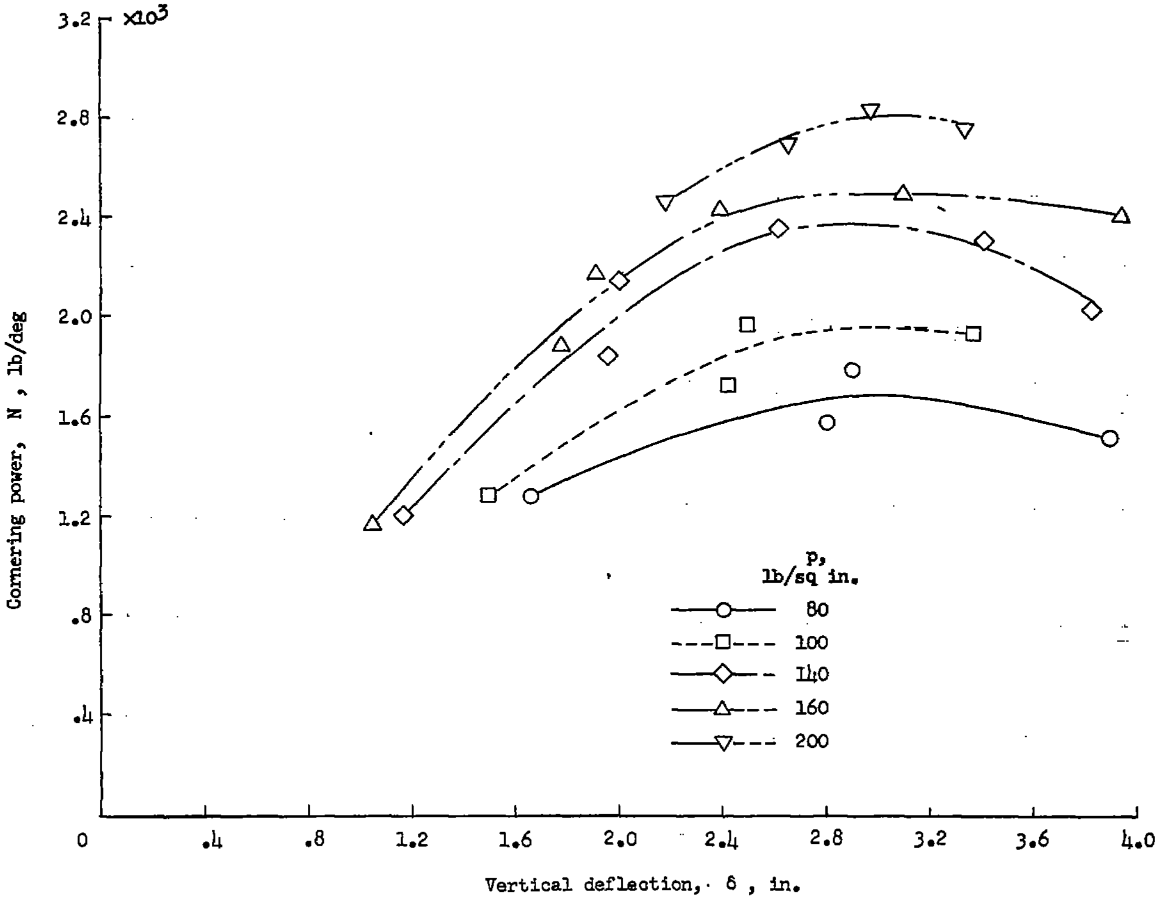

Figure 48.- Variation of cornering power with vertical deflection for several inflation pressures for a pair of 56x16-24PR-VII-R22 tires.

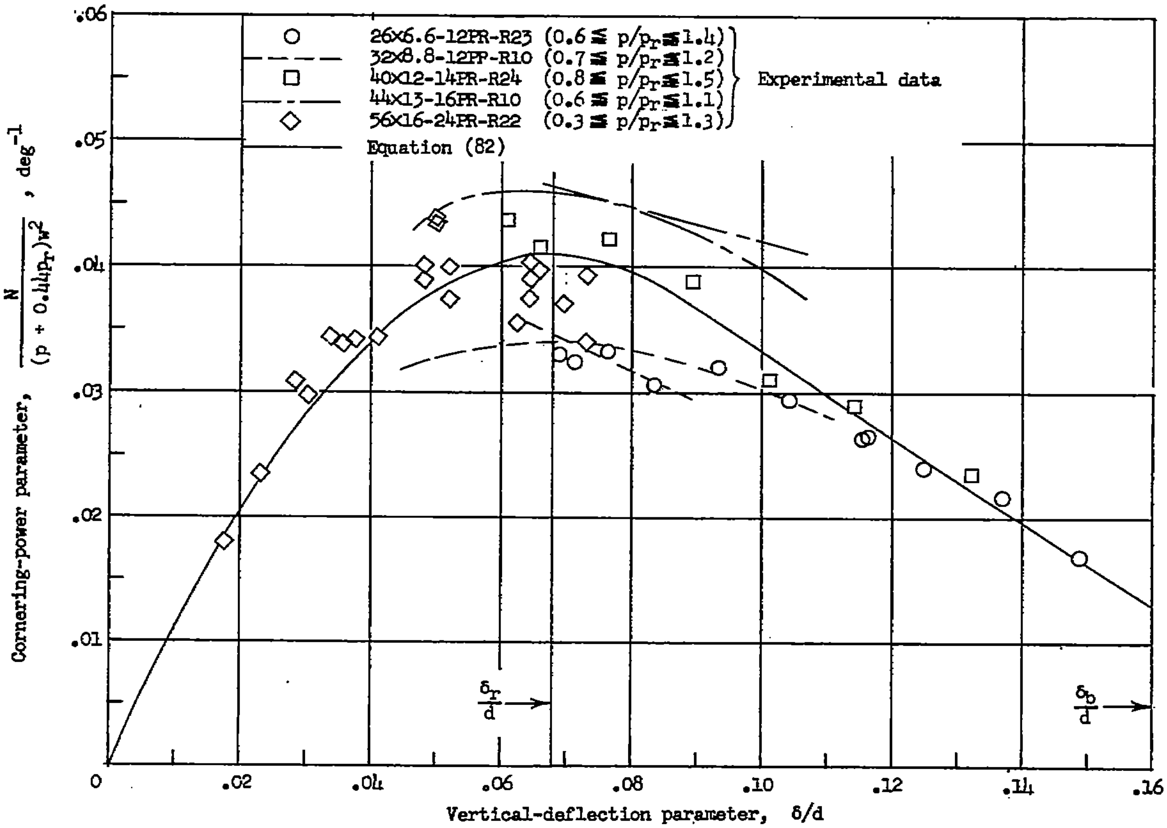

(a) Type VII tires.

Figure 49.- Variation of cornering-power parameter with vertical-deflection parameter for several tires.

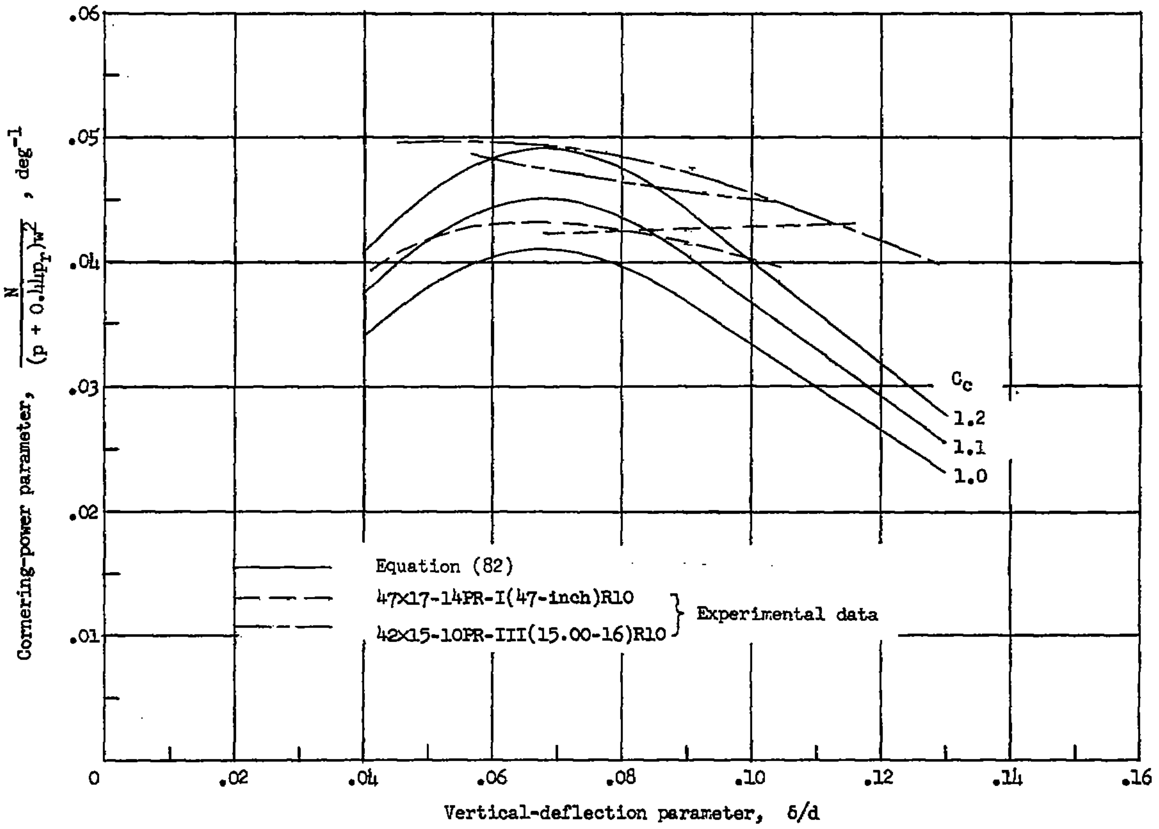

(b) Types I and III tires.

Figure 49.- Concluded.

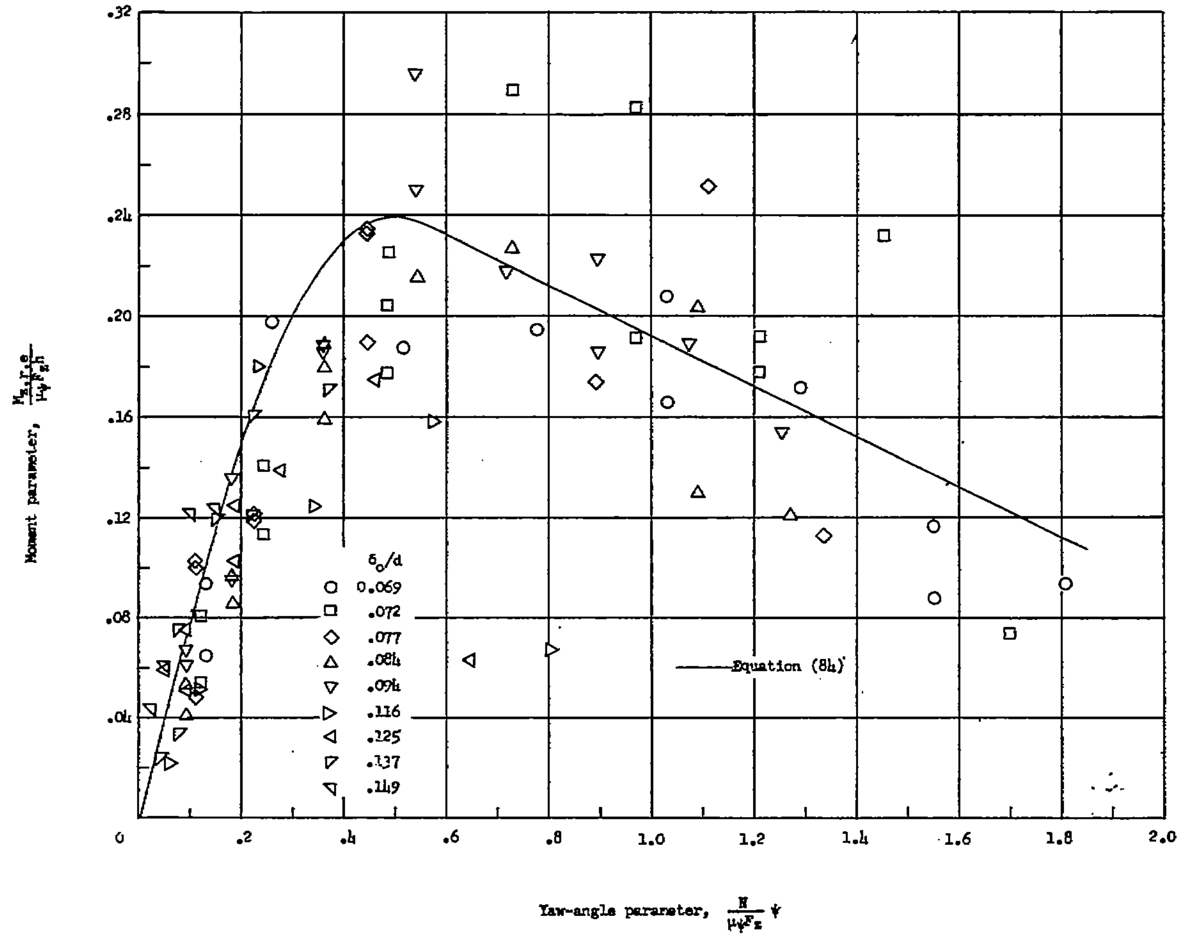

(a) 26x6.6-12PR-VII-R23 tires.

Figure 50.- Variation of self-alining-torque parameter with yaw-angle parameter for steady-state yawed rolling of several type VII tires.

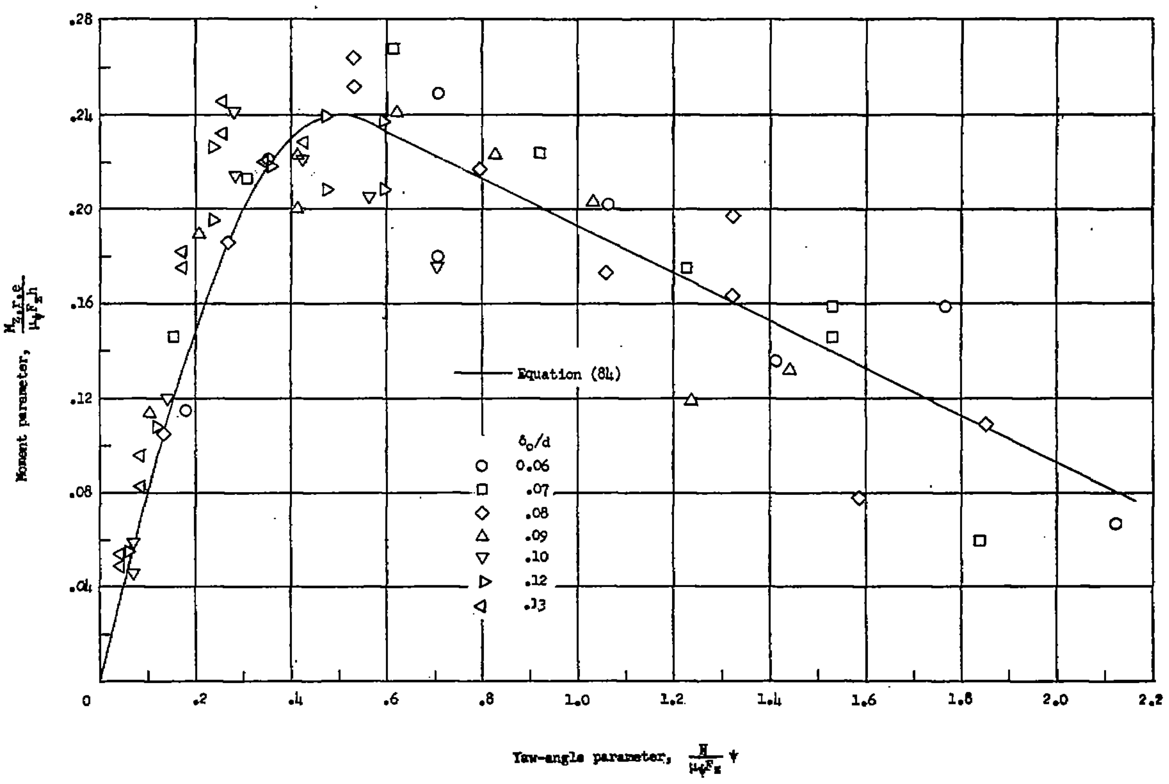

(b) 40x12-14PR-VII-R24 tires.

Figure 50.- Continued.

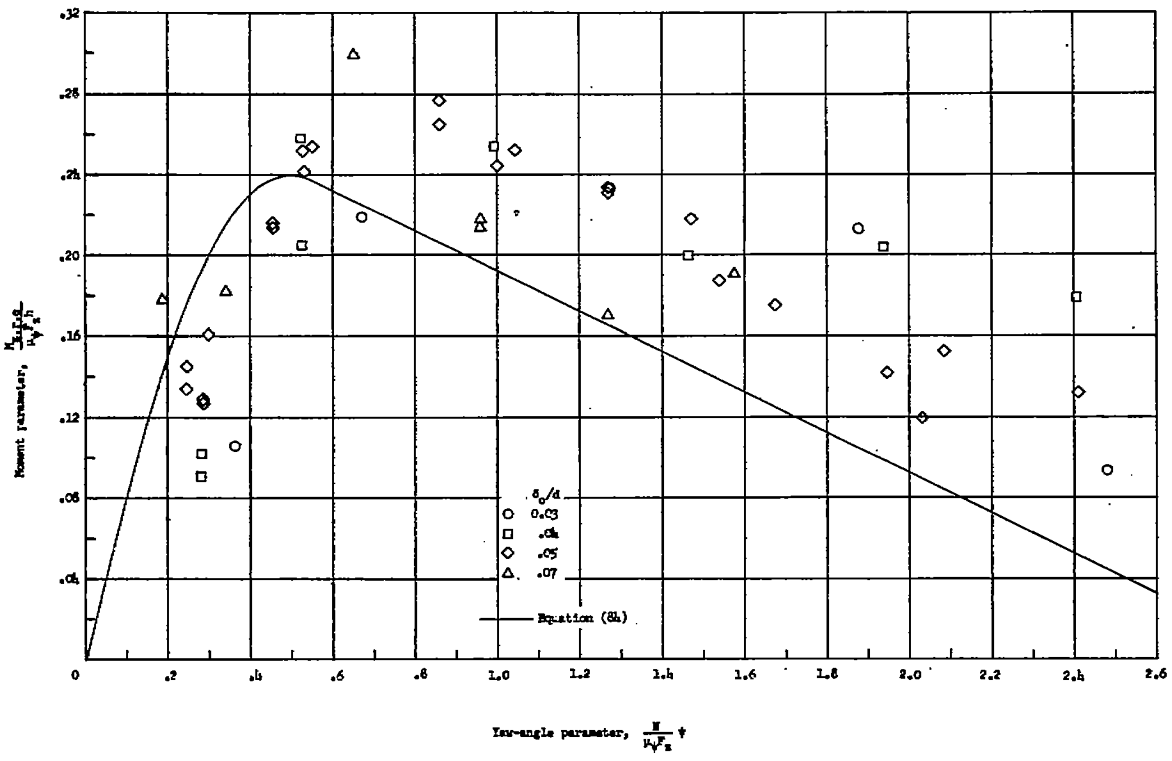

(c) 56x16-24PR-VII-R22 tires.

Figure 50.- Concluded.

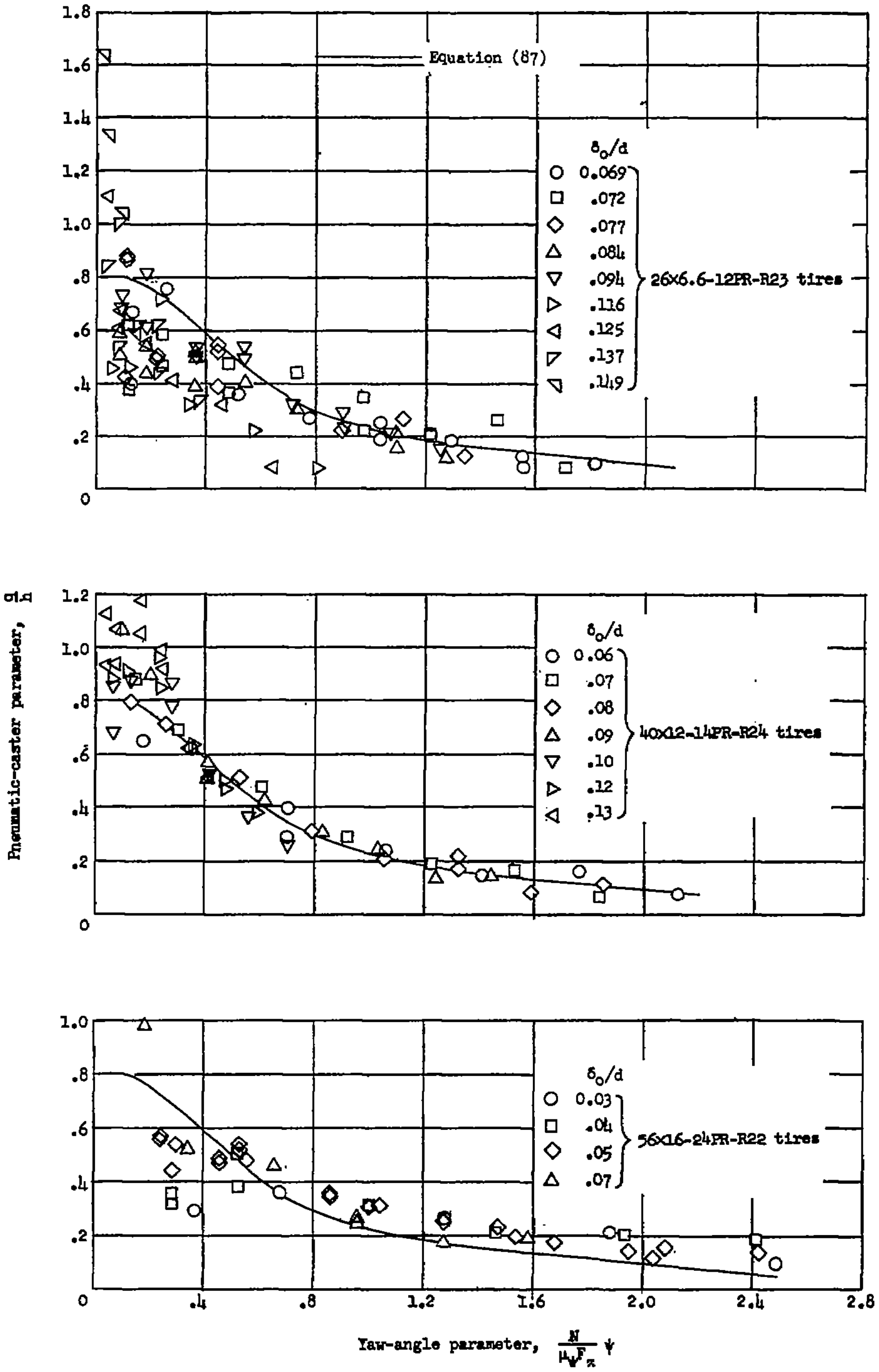

Figure 51.- Variation of pneumatic-caster parameter with yaw-angle parameter for several pairs of type VII tires.

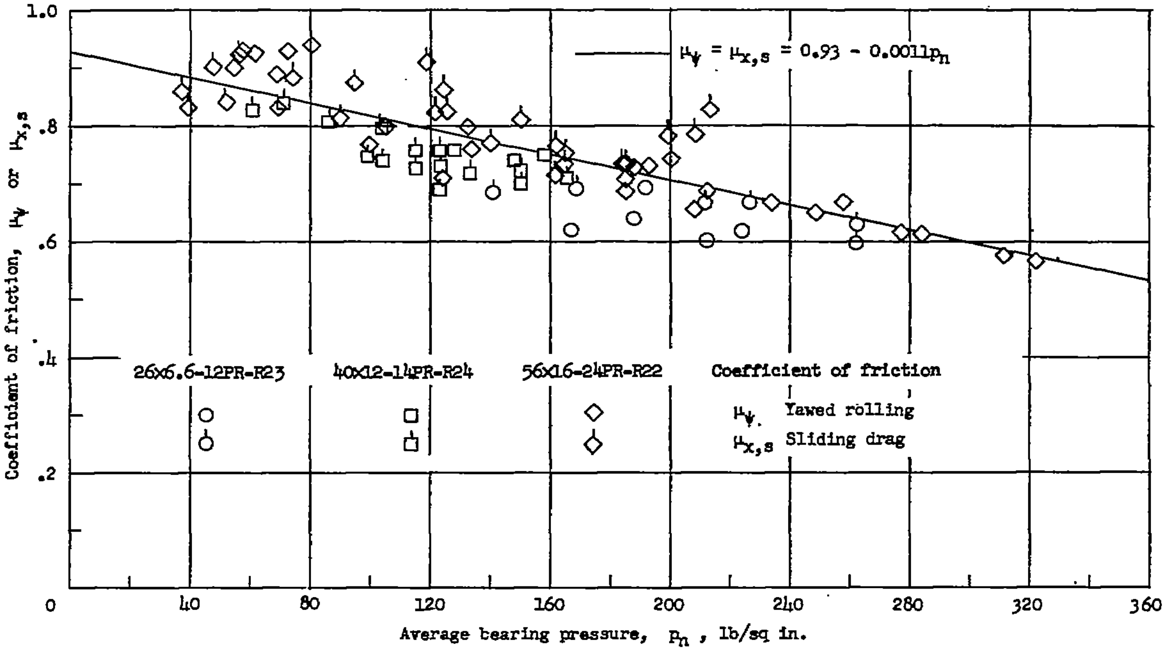

Figure 52.- Variation of sliding-drag and yawed-rolling coefficients of friction with bearing pressure from slow-speed tests of several type VII tires.

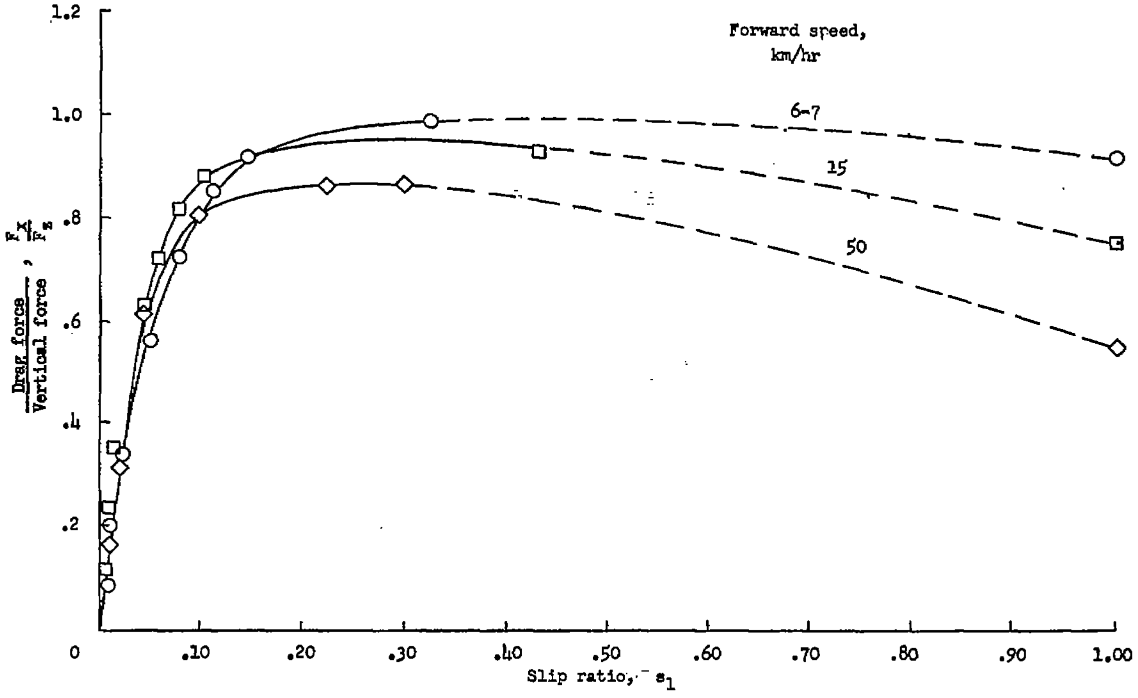

Figure 53.- Experimental variation of drag force with slip ratio for braking tests of an automobile tire on dry concrete. (Data from ref. 13.)

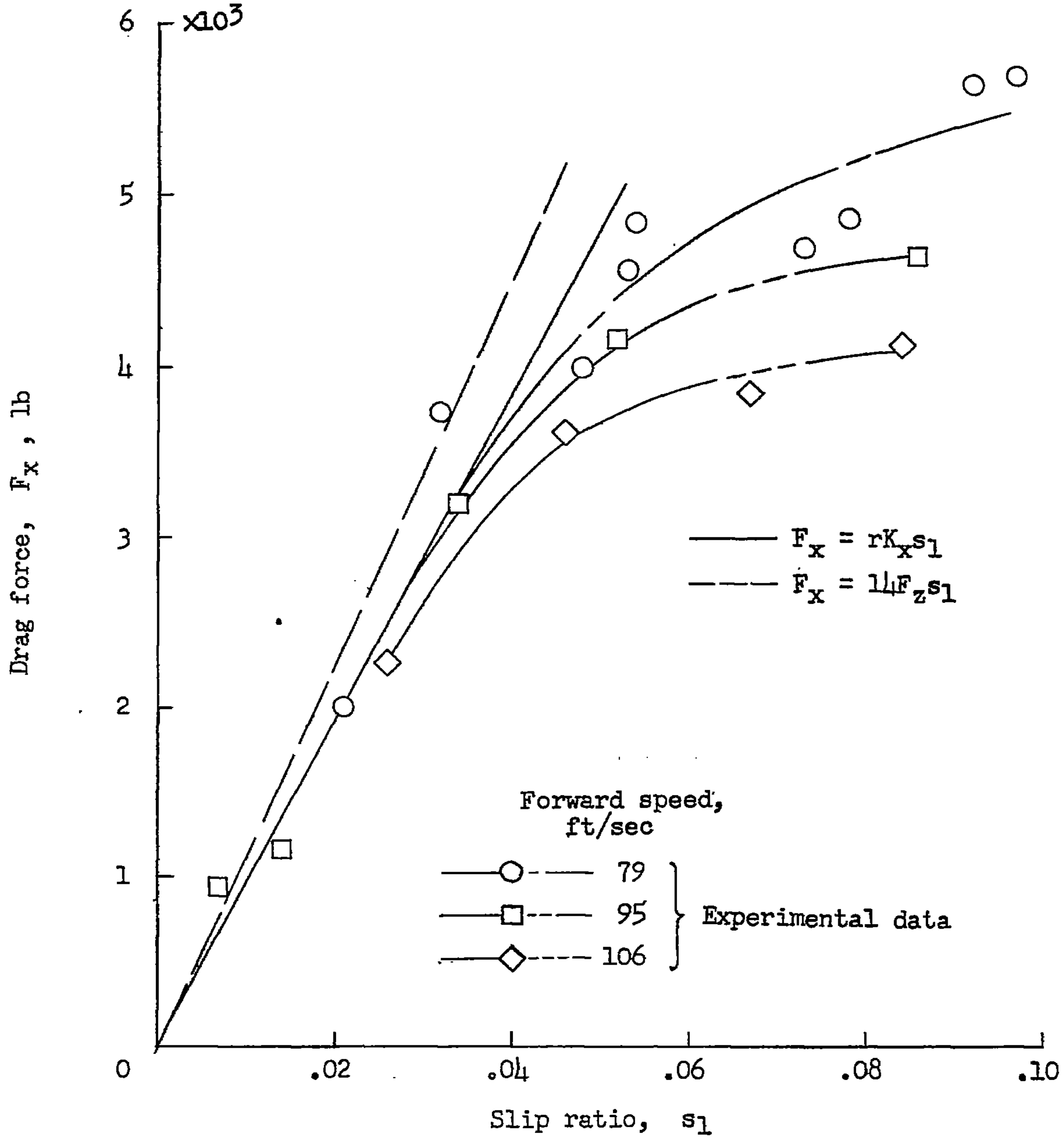

Figure 54.- Variation of drag force with slip ratio for braking tests of a 48×17-16PR-III(17.00-20)RU aircraft tire. $F_z \approx 8,000$ pounds; K_x(estimated) $\approx 4,000$ pounds per inch.

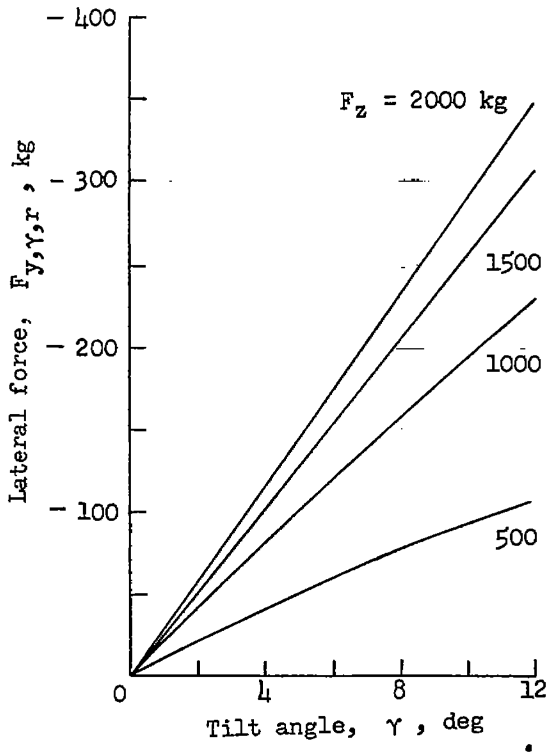

(a) Variation of lateral force with tilt angle.

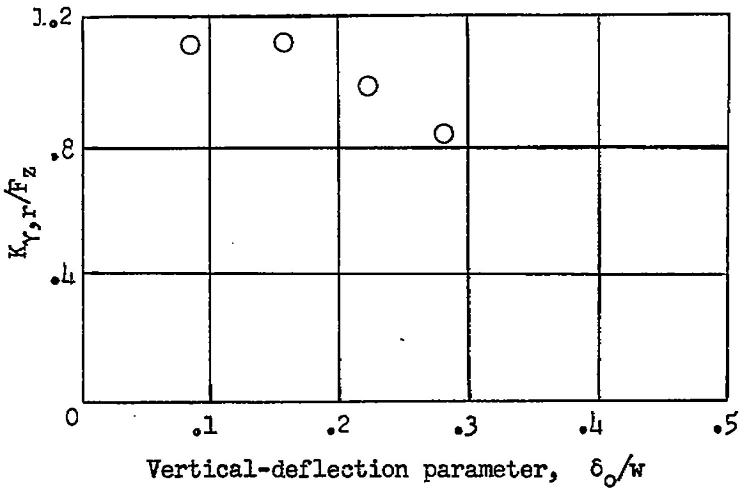

(b) Variation of tilt parameter $K_{\gamma,r}/F_z$ with vertical deflection.

Figure 55.- Experimental lateral-force data for unyawed tilted rolling behavior of a 28×7-R35 tire.

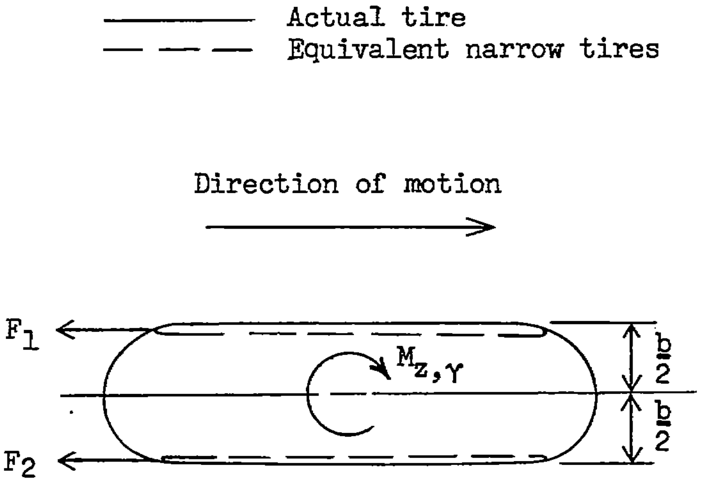

(a) Top view.

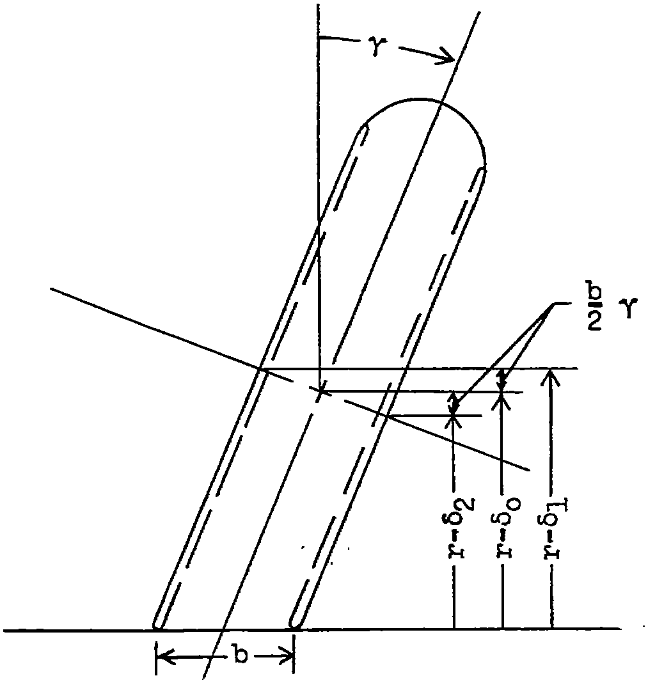

(b) Rear view.

Figure 56.- Sketches of a tilted rolling tire.

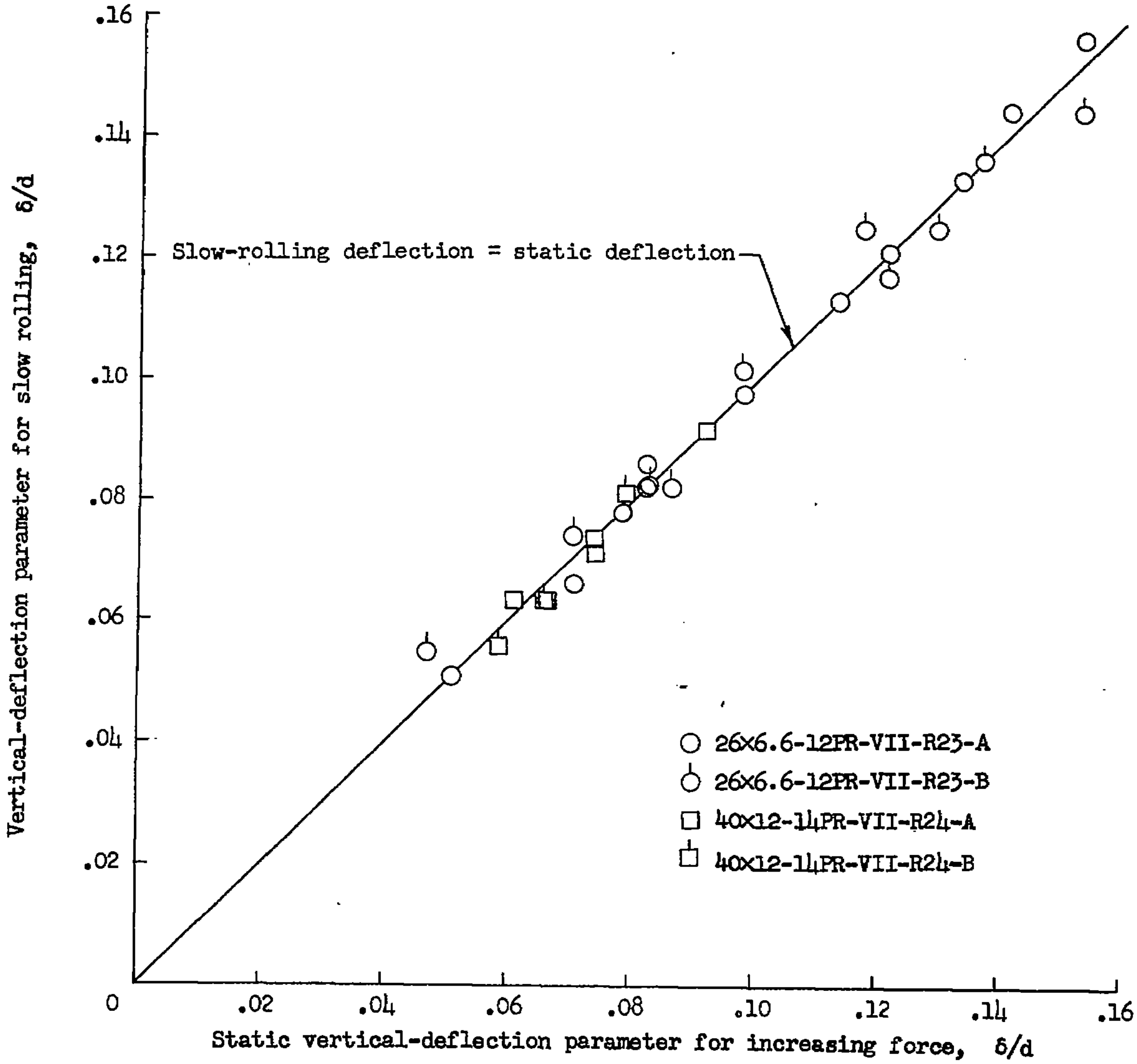

Figure 57.- Comparison of vertical deflections obtained from static tests with values obtained from slow-rolling tests.

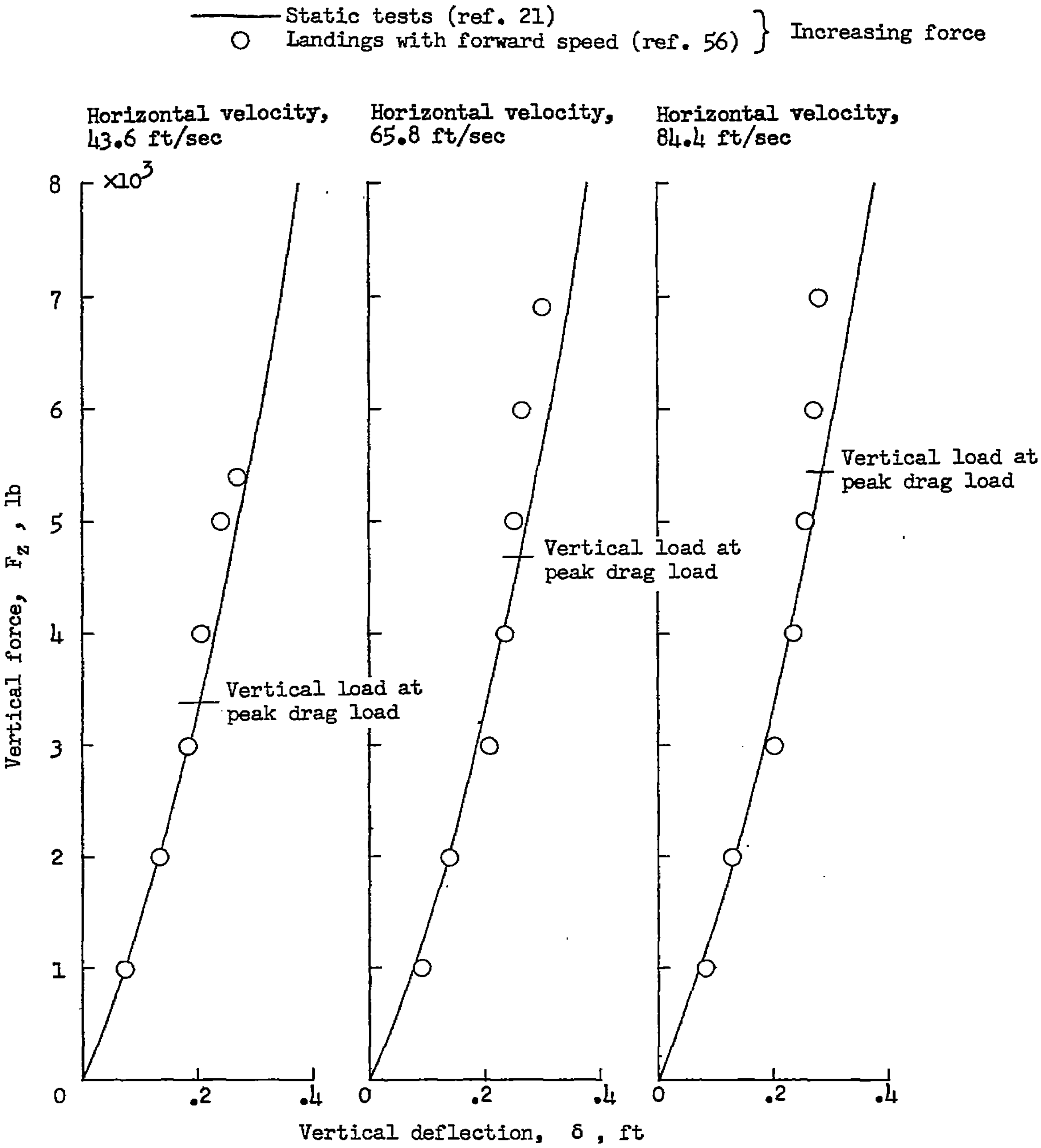

Figure 58.- Comparison of tire vertical-force-deflection curves from landings and from static tests for 28×9-10PR-I(27-inch) tires. p_o = 32 pounds per square inch; v_o = 7.5 feet per second.

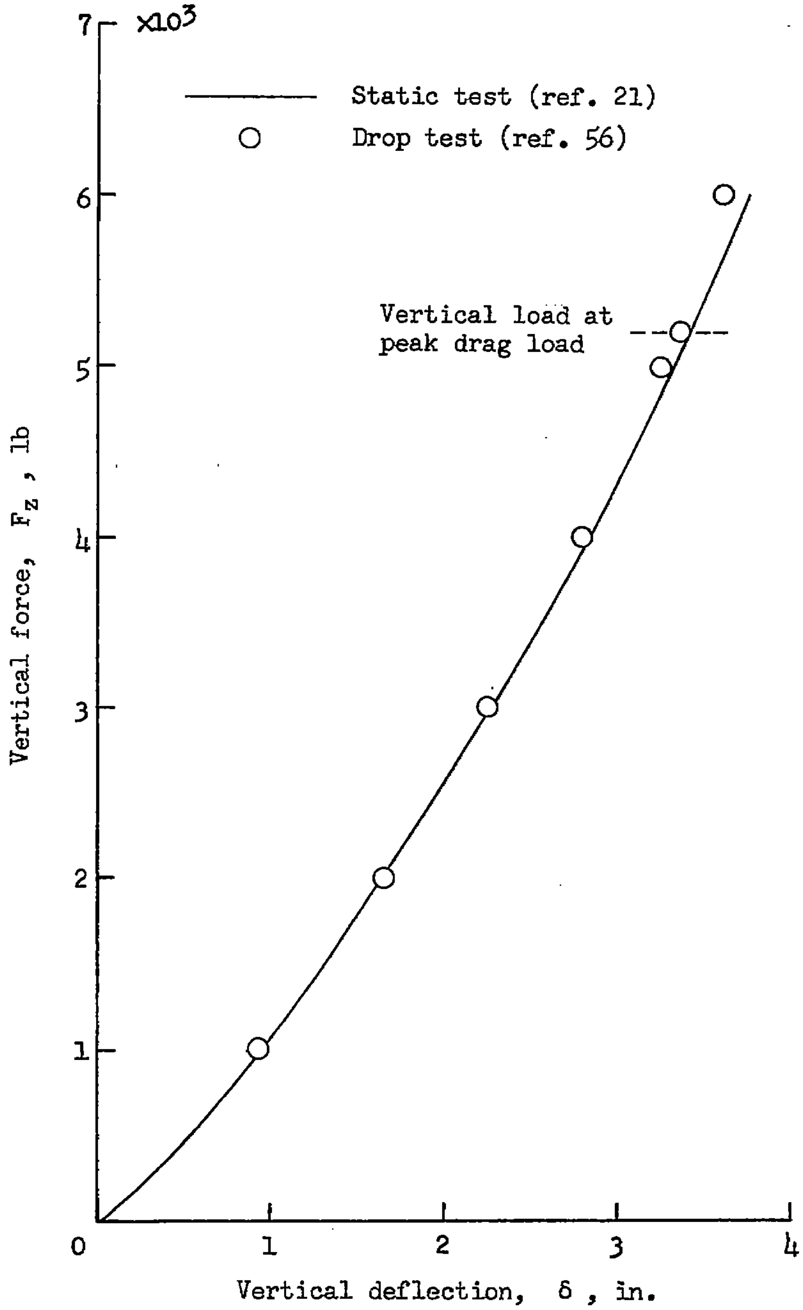

Figure 59.- Comparison of static vertical-force-deflection curve with force-deflection curve obtained from prerotation drop tests with initial peripheral velocity of 88 feet per second and initial vertical velocity of 7.5 feet per second. Data for 28×9-10PR-I(27-inch) tires; p_o = 32 pounds per square inch.

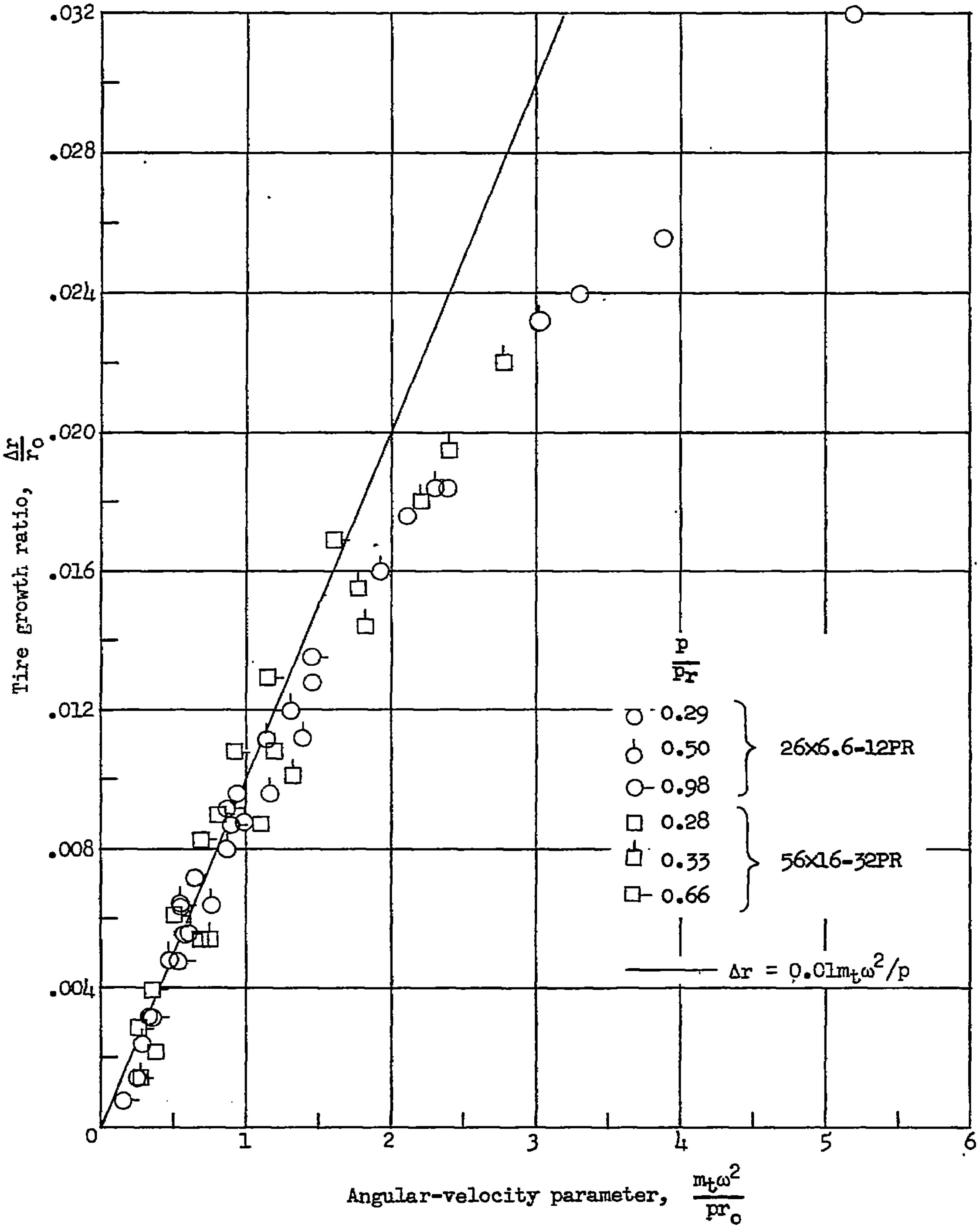

Figure 60.- Growth of tire radius due to centrifugal forces for two type VII tires. (Experimental data from tables III and IV.)

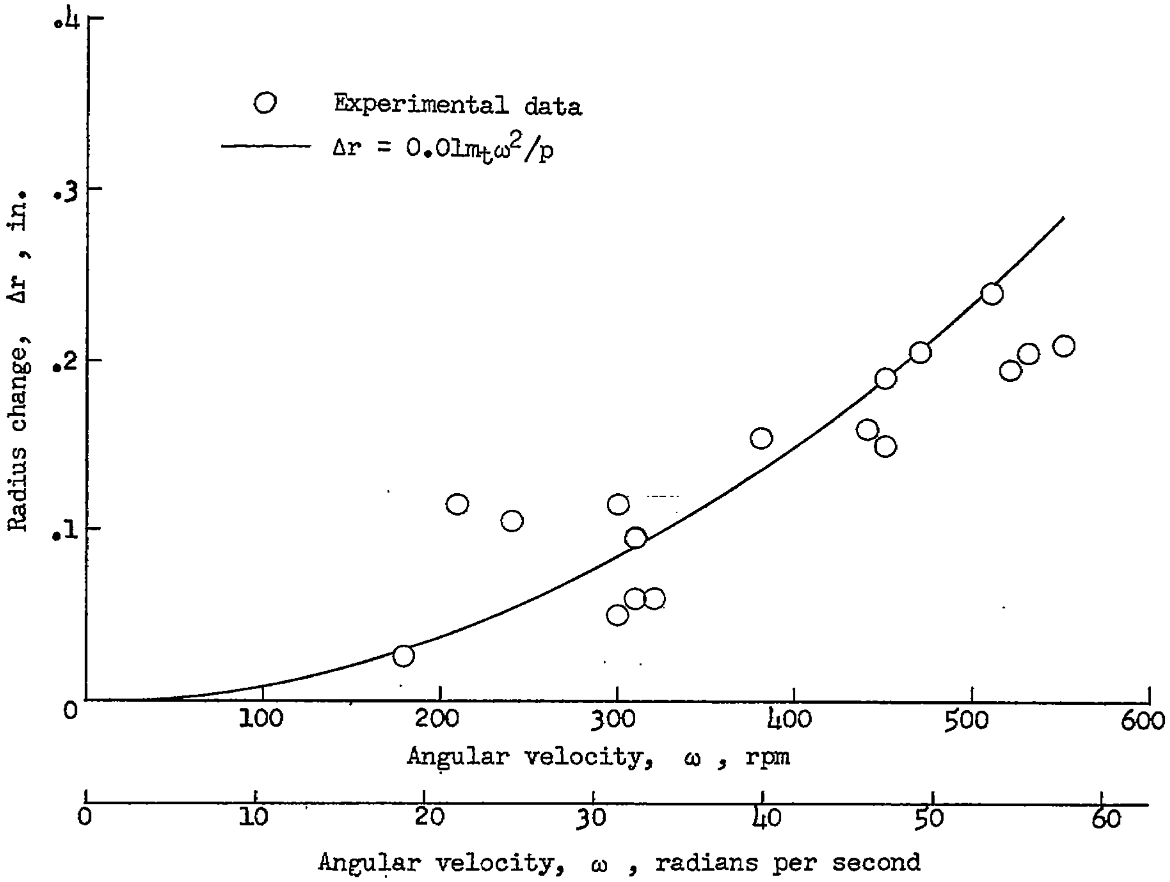

Figure 61.- Growth of tire radius due to centrifugal forces for a pair of 57×20-16Ply-I(56-inch)R53 tires. r = 28.3 inches; p = 80 pounds per square inch; m_t(estimated) = 8.2 slugs.

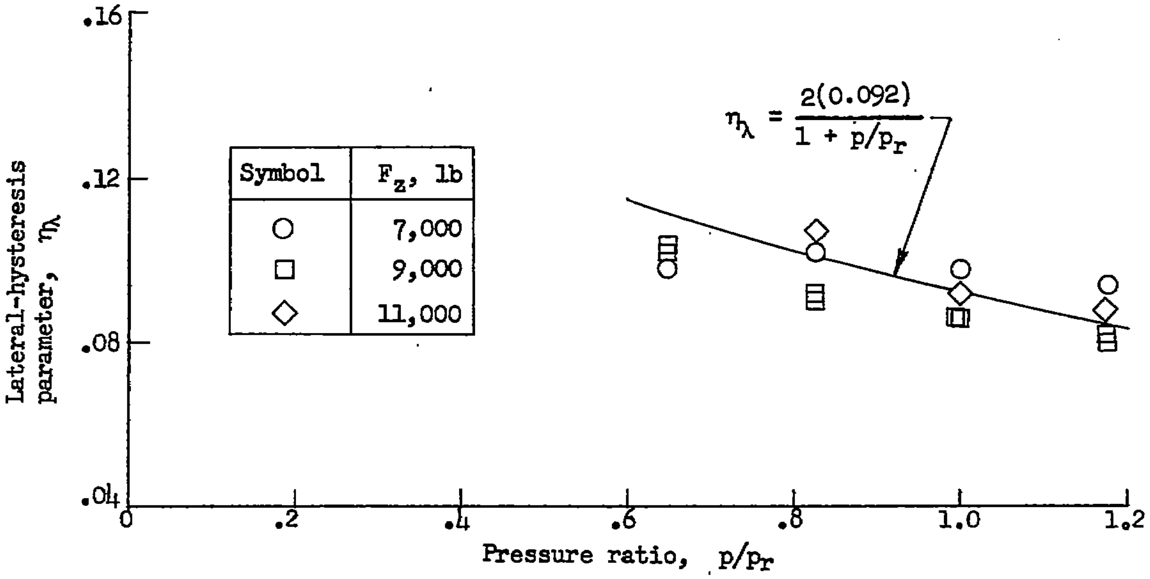

(a) 24×7.7-R25 normal-tread tires.

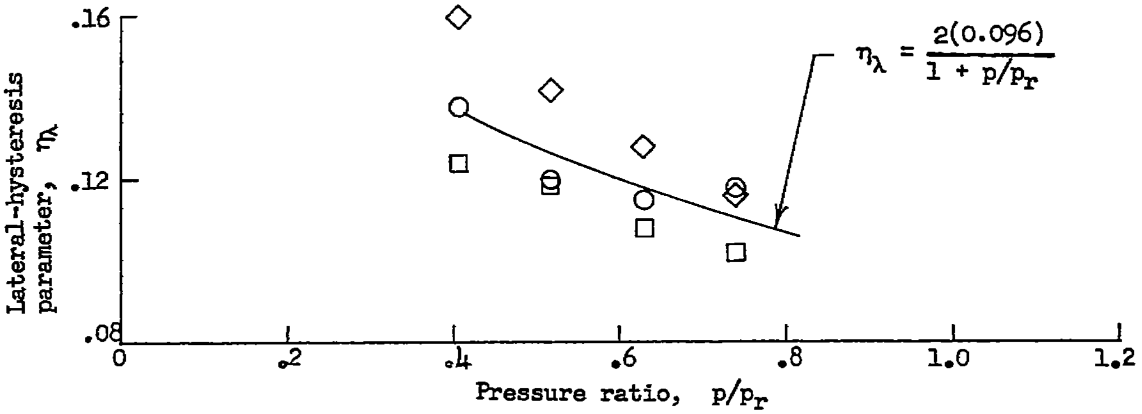

(b) 26×6.6-10Ply-R25 channel-tread tires.

Figure 62.- Variation of dynamic lateral-hysteresis parameter with inflation pressure for two pairs of type VII tires.

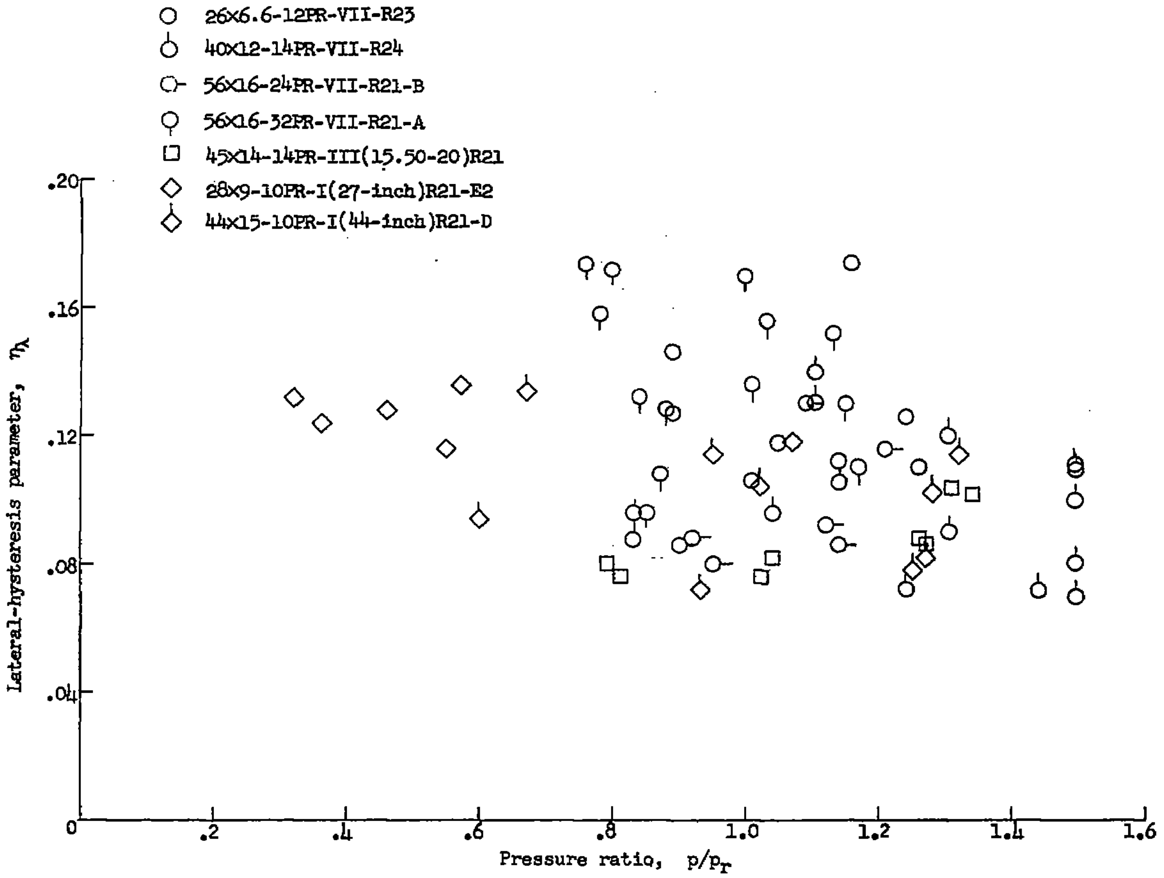

Figure 63.- Variation of static lateral-hysteresis parameter with inflation pressure for several types I, III, and VII tires.

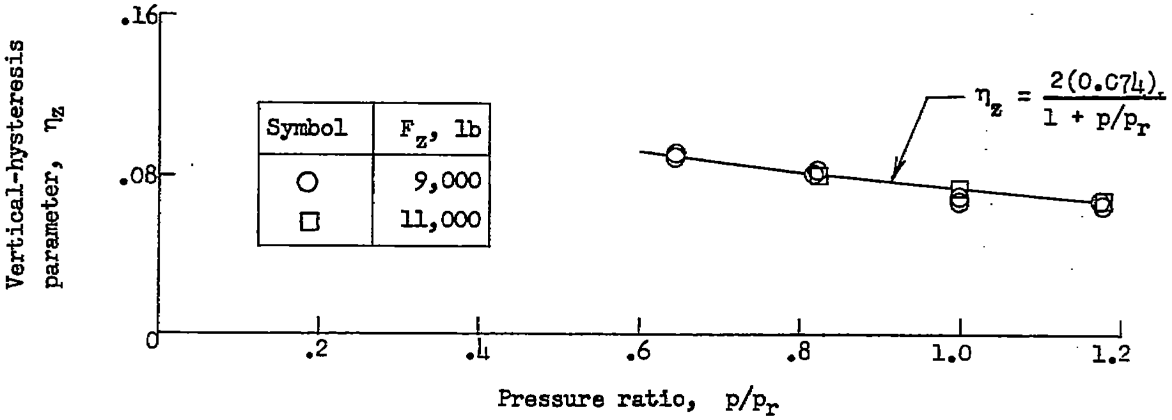

(a) 24x7.7-R25 normal-tread tires.

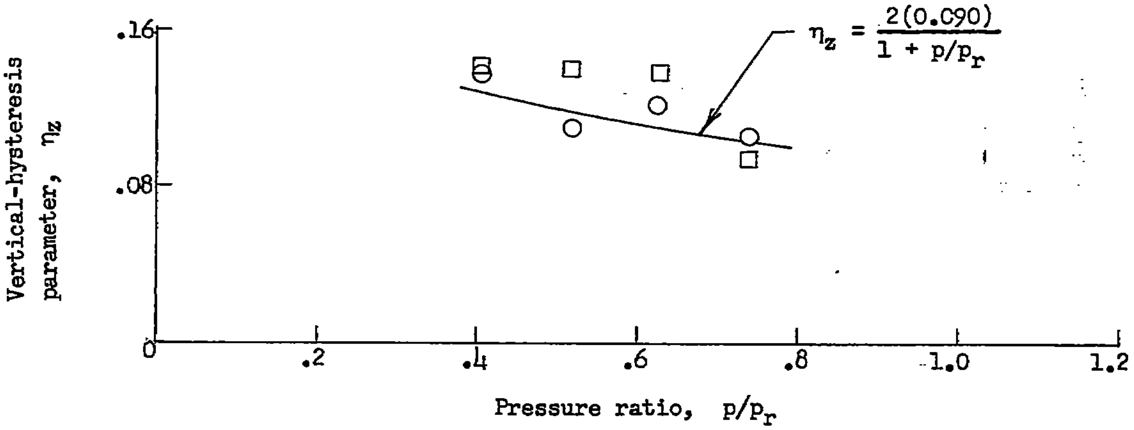

(b) 26x6.6-10Ply-R25 channel-tread tires.

Figure 64.- Variation of dynamic vertical-hysteresis parameter with inflation pressure for two pairs of type VII tires.

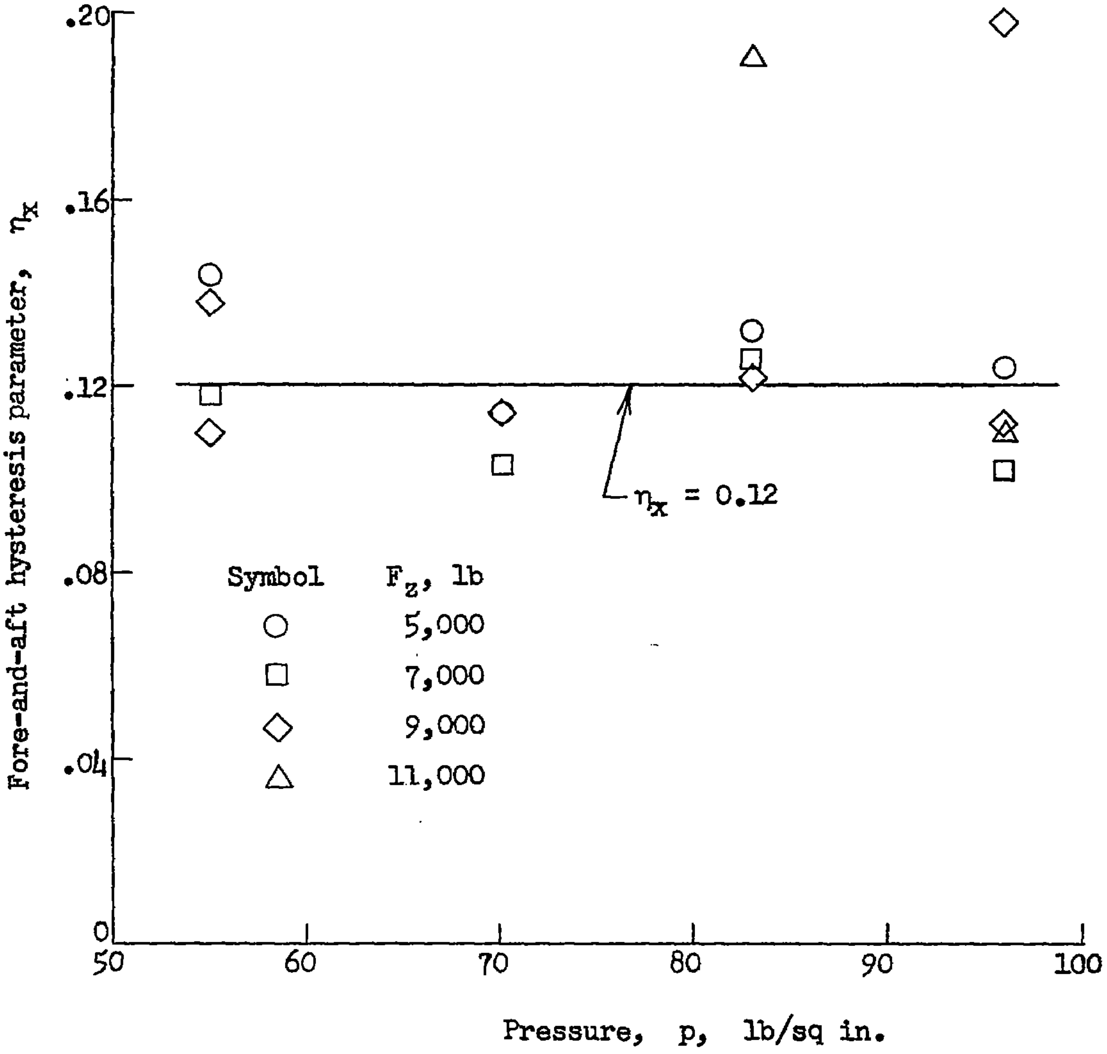

Figure 65.- Variation of dynamic fore-and-aft hysteresis parameter with inflation pressure for pair of 26x8-R25 tires.

NACA - Langley Field, Va